UNIVERSITY OF CALIFORNIA
Los Angeles

Reconfigurable and Conformal Antennas based on the Emerging Liquid Metal and Electro-Textile Materials

A dissertation submitted in partial satisfaction
of the requirements for the degree
Doctor of Philosophy in Electrical and Computer Engineering

by

Lingnan Song

2020

ABSTRACT OF THE DISSERTATION

Reconfigurable and Conformal Antennas based on the Emerging Liquid Metal and Electro-Textile Materials

by

Lingnan Song
Doctor of Philosophy in Electrical and Computer Engineering
University of California, Los Angeles, 2020
Professor Yahya Rahmat-Samii, Chair

With the development of wireless communications and its growing importance in all aspects of everyday life, the demand for developing robust and versatile wireless devices that support higher data rates is increasing. Antennas play a central and critical role in this endeavor. For RF and antenna engineers, next-generation antenna designs involve new materials and fabrication processes for emerging wireless applications. In the first part of this work, reconfigurable antennas based on liquid metal and 3D printed microfluidics are proposed. With the development of a robust liquid handling process on printed circuit board (PCB), two reconfigurable patch antenna implementations are introduced and characterized for the use of wide-band frequency reconfigurable or polarization reconfigurable antennas. An organ-tuned monopole antenna for microwave induced thermal ablation is also proposed based on liquid metal reconfiguration. The studies aim to explore novel reconfiguration technique enabled by new materials and manufacturing technologies with the potential of providing more functionalities and reduced cost. In the second part of the work, conformal antennas based on electro-textile for wireless body-area network (WBANs) are investigated. Electro-textile is playing a key role in the current and future smart garments implementations. We start with the detailed design and modeling strategies for embroidery-based electro-textile antennas. The patch antenna bending effects are then carefully investigated both numerically and experimentally. Nature-inspired global optimizations (e.g. particle swarm optimization and brain-storm optimization) are implemented in these designs and analyses.

The dissertation of Lingnan Song is approved.

Tatsuo Itoh

Yuanxun Ethan Wang

Sam Emaminejad

Yahya Rahmat-Samii, Committee Chair

University of California, Los Angeles

2020

To my parents,

who set me great examples,

who love and support me under all circumstances.

To my lovely husband,

whose love, inspiration and encouragement make me who I am.

TABLE OF CONTENTS

LIST OF FIGURES

LIST OF TABLES

ACKNOWLEDGMENTS

I am forever indebted to Professor Yahya Rahmat-Samii, who has set me an amazing example as a good researcher and good educator, whose support, guidance, wisdom, and time furthered my education and personal developments in my two years of my M.S. and four years of Ph.D study.

I am sincerely grateful to Professor Tatsuo Itoh, Professor Ethan Wang and Professor Sam Emaminejad for their time and efforts spent as part of my thesis committee.

I would like to thank Prof. Chi On Chui and Wuran Gao, for their time and resources spent during the collaboration in developing the liquid metal handling technique.

I would like to thank Dr. Jason Chiang and Dr. Fereidoun Abtin, for the insightful discussions and collaboration in the research project on microwave ablation.

I would like to acknowledge and thank all my wonderful labmates Joshua Kovitz, Jordan Budhu, Daisong Zhang, Vignesh Manohar, Botian Zhang, Anastasios Papathanasopoulos, Dustin Brown, Junbo Wang and Yubin Cai, from the UCLA Antenna Research, Analysis, and Measurement Laboratory for their constant support during my stay at UCLA.

VITA

1991	Born in Tianjin, China.
2013	Undergraduate Student Researcher in Nanomechanics and Nanoengineering Laboratory, North Carolina State University, Raleigh, NC
2014	B.S. in Optical Engineering, Zhejiang University, Hangzhou, China
2014-2018	Graduate Student Researcher in Antenna Research, Analysis, and Measurement Laboratory, University of California Los Angeles, Los Angeles, CA
2016	M.S. in Electrical Engineering, University of California Los Angeles, Los Angeles, CA
2017-2020	Teaching Assistant (EE101A Engineering Electromagnetics, EE2 Physics for Electrical Engineers, BE120 Biomedical Transducers), University of California Los Angeles, Los Angeles, CA

HONORS AND AWARDS

2019	International Symposium on Electromagnetic Theory (EMTS) Young Scientist Award
2017	First Place in the 2017 Ernest K. Smith USNC-URSI Student Paper Competition.
2016	HSSEAS Outstanding Master Thesis Award, Physical & Wave Electronics.
2016-2018	URSI National Radio Science Meeting Travel Award.

PUBLICATIONS

L. Song, W. Gao, and Y. Rahmat-Samii, "3D Printed Microfluidics Channelizing Liquid Metal for Multi-Polarization Reconfigurable Extended E-Shaped Patch Antenna," *IEEE Transactions on Antennas and Propagation*, 2020.

L. Song and Y. Rahmat-Samii, "A Hybrid of Particle Swarm and Brain Storm Optimization for Application in Electromagnetics", *URSI General Assembly*, 2020 (accepted).

L. Song, W. Gao, and Y. Rahmat-Samii, "3D Printing-based Liquid Metal Patch Antennas with Wide-Band Frequency and Multi-Polarization Reconfigurations", *International Symposium on Electromagnetic Theory*, 2019.

L. Song, W. Gao, C. O. Chui and Y. Rahmat-Samii, "Wideband Frequency Reconfigurable Patch Antenna With Switchable Slots Based on Liquid Metal and 3-D Printed Microfluidics," *IEEE Transactions on Antennas and Propagation*, vol. 67, no. 5, March 2019, pp. 2886–2895.

L. Song and Y. Rahmat-Samii, "A Systematic Investigation of Rectangular Patch Antenna Bending Effects for Wearable Applications," *IEEE Transactions on Antennas and Propagation*, vol. 65, no. 7, April 2018, pp. 3399–3408.

L. Song and Y. Rahmat-Samii, "An End-to-End Implanted Brain-Machine Interface Antenna System Performance Characterization and Development," *IEEE Transactions on Antennas and Propagation*, vol. 65, no. 7, July 2017, pp. 3399–3408.

CHAPTER 1

Introduction

1.1 New Materials for Next Generation Antenna Developments

Electromagnetic wave is ubiquitous in everyday life. All communication systems depend, to some extent, on electromagnetic devices such as antennas. Furthermore, the ever increasing demand for high capacity and small size presents more challenges for RF and antenna engineers in terms of multi-functionality, miniaturization and integration. The development of novel materials such as metamaterials [1, 2], micro or nano-composites [3], and smart or functional materials [4] introduces properties that are not occurring in conventionally used conductors and dielectrics. For example, inhomogeneous lenses can be used to significantly improve the directivity, reconfigurable antennas can be designed to satisfy changing environment or varying user requirements, and electro-textile materials can be used for future body area network applications with seamless integration of electronic systems. Fig. 1.1 illustrates some of the representative new materials that may contribute to the next generation antenna design. In addition, the evolution of additive manufacturing techniques and material processing has shown to have significant advantages for antenna design [5]. The ability to 3D print dielectric and conductive elements has been proved to be invaluable in antenna prototyping with improved accuracy and reduced cost. The advance in material science and manufacturing technologies have provided an opportunity in designing antenna systems with improved functionalities. The Engineering and Physical Science Council (EPSRC) has identified the favorable material properties as well as specific research challenges in the area of RF and Microwave Devices in which new materials might lead to a step change in technologies or performances [6]. Addressing such challenges would necessitate collaboration

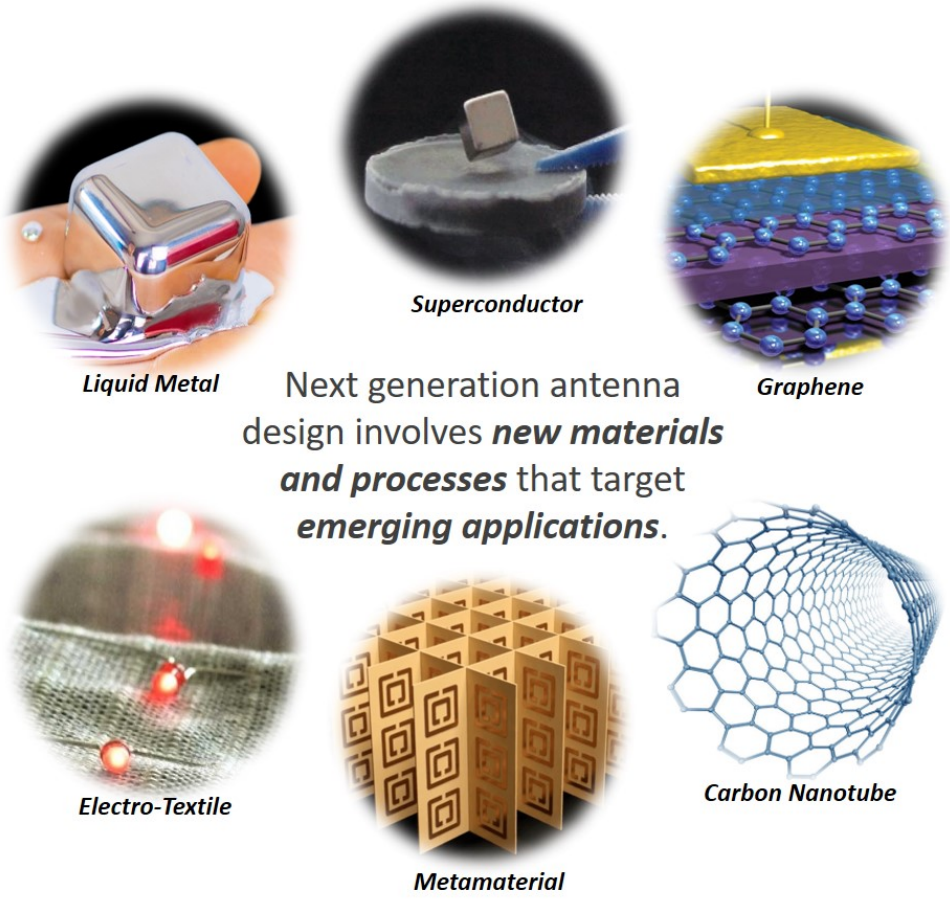

Figure 1.1: The next generation antenna design involves new materials and processes that target emerging applications.

between RF and microwave technologies and researchers in material science. For the area of antenna in particular, the research challenges and associated material properties have been identified, as listed in Fig. 1.2.

The vision of this work is to identify significant antenna design challenges that could be potentially addressed based on two types of new materials, i.e. liquid metal and electro-textile, and investigate the possible antenna design solutions accordingly. In each of the specified scenario, certain features or functionalities desired for the antenna will be investigated.

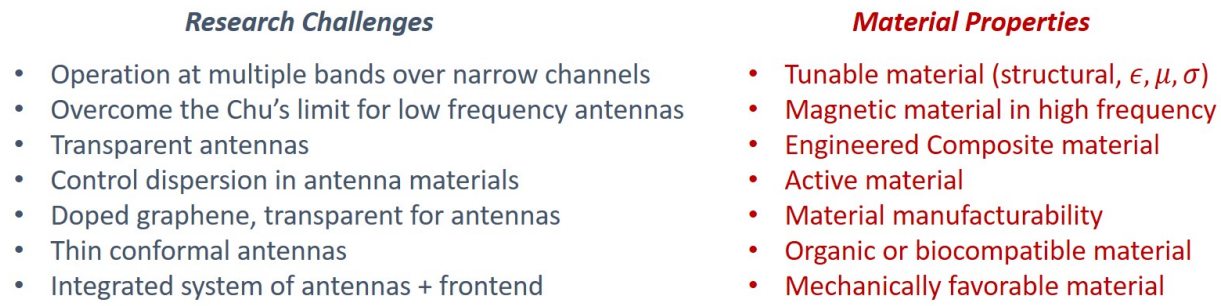

Figure 1.2: The research challenges in the area of antenna identified by EPSRC and the associated material properties which might contribute to addressing these.

1.2 Reconfigurable Antennas with Liquid Metal Tuning

As one of the major identified current research highlights in antenna area, reconfigurable antennas meet the varying needs of communication systems by adding functionalities, including frequency, polarization and pattern agility. The frequency agility allows the antenna to switch and operate between different bands, while the pattern reconfigurability can steer and maximize the radiation in a particular direction. Additionally, polarization diversity is used to reduce the polarization mismatch losses. These reconfigurabilities make efficient use of the frequency spectrum and power to maximize power transfer in a changing communication environment. Thus, reconfigurable antennas eliminate the need to accommodate multiple single-state antennas into the system. They further satisfy demands of miniaturization and compactness for modern electronic devices. Reconfiguration or adaptation can be implemented in antennas through the use of RF switches such as RF-MEMS, varactors, PIN diodes, or even optoelectronic switches. Other means of reconfigurability include mechanical movement or even microfluidic technology. Conventionally, electrical switching is the most popular reconfiguration technique due to its fast switching and easy integration of electrical switches into antenna systems. For example, multiple MEMS switches or PIN diodes have been utilized to deliver dynamic antenna reconfigurations [7, 8]. Varactor diodes offer a continuous and tunable capacitance when biased by a voltage. Therefore, a continuous frequency-reconfigurable antenna is achieved by integrating varactors on the radiation edges [9, 10]. However, such localized switching components at a few locations of

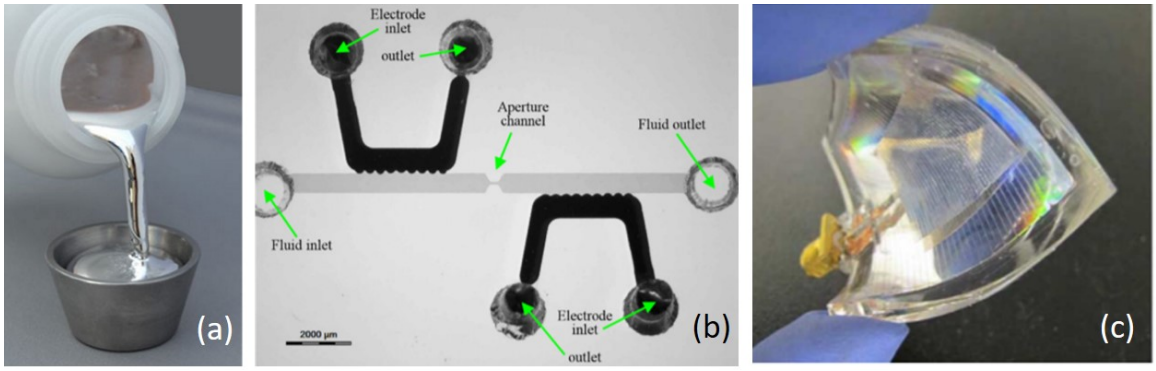

Figure 1.3: The research challenges in the area of antenna identified by EPSRC and the associated material properties which might contribute to addressing these.

a reconfigurable antenna are only able to realize a limited number of reconfiguration states. Additionally, incorporating these semiconductor switches into the antenna system can lead to undesirable signal distortion due to the nonlinear characteristics of the active components, limiting their applications in high power transmission scenarios. Overall, the above reconfiguration techniques only deliver a small number of reconfiguration states. Therefore, the reconfigurable characteristics of an antenna are limited based on existing techniques.

Comparing to existing reconfiguration methods, liquid metal based reconfiguration has been shown as a promising technique in terms of lower loss, more power handling, and greater tuning range [11]. In particular, liquid metal eutectic gallium indium (EGaIn) demonstrates low toxicity, high conductivity (3.4×10^6 S/m) and very good flexibility [12]. Several works implementing liquid metal have been published in the development of reconfigurable electronics, including tunable monopole and dipole antenna [13–15], slot antenna [16], and helical antenna [17]. In these works, the liquid metal is controlled either by the pressure difference with syringes or pumps, or by the voltage difference utilizing the effect of electro-wetting [18], which physically modify the antenna topology or parasitic structure and therefore change the antenna radiation characteristics.

In the first section of this work, the use of liquid metal EGaIn in designing slot loaded reconfigurable patch antennas is extensively explored. Slot-loaded patch antennas have been widely used in wireless communication, due to their low-profile, low-cost feature and ca-

pability of realizing various functionalities. The goal of this work is to utilize the flexible nature of liquid conductor to achieve patch antenna reconfiguration capabilities in all aspects of antenna characteristics, i.e. frequency, polarization and radiation pattern agilities. The processes developed for fabricating such type of liquid metal and microfluidic based reconfigurable patch antennas is also discussed. Building reliable microfluidics on printed circuit boards (PCB) presents a great challenge of upscaling in the microfluidics society. One of the major difficulties is the incompatibility between PCB and the popular microfluidic material PDMS. In this work, we for the first time explore the option of integrating 3D printed microfluidics onto PCB for the application of reconfigurable patch antennas. With the concept of liquid metal tuning, we also describe and propose a coaxial ablation antenna that can be adaptively tuned with liquid metal to maintain the optimal impedance matching as it is transfered among different organs of treatment, at the frequency of 2.45 GHz. Ablation performances are validated in ex vivo porcine liver and lung tissue.

1.3 Conformal Antennas with Electro-Textile

Another important aspect of the current antenna design highlights lies in the applications involving wireless body-area networks (WBANs), which enables the vision of ubiquitous healthcare. The recent advances in wireless communication and in electronics offer small and intelligent sensors able to be used on, around, or implanted in the human body. In this context, WBANs constitute an active field of research and development as it offers the potential of great improvement in the delivery and monitoring of healthcare. A typical WBANs consist of a number of nodes formed with biological sensing devices. Each of them is placed onto different parts of the body and can be wearable or implanted. Each of them has specific features and is used for different missions, such as measuring changes in a patient's vital signs and detecting emotions or human statuses etc. Communications between different nodes are supported by Bluetooth, WIFI, or IEEE 802.15.4. and IEEE 802.15.6, which were designed especially for WBAN applications.

The development of conformal and wearable antennas plays a critical role in WBANs.

Generally, there are three major challenges in designing wearable antennas. Firstly, the selection of conductive and dielectric materials need to ensure wearability and long-term performance. Secondly, the proximity of lossy human tissue results in a reduction of antenna efficiency and limits the maximum transmit power due to concerns of heating in human tissue. Thirdly, the bending effects degrade the performance of antennas compared to their flat condition. And even if the antenna is designed for a certain bending radius, the interpersonal bending variation can be significant in determining the antenna performance.

The manufacturing technologies for conformal or flexible antennas generally fall into two major categories: printing and embroidery technologies. Printing technology recently has gained significant attention because of their potential application in areas such as large area printed electrical sensors and "skin-like" membranes [19–21]. Another type of technology is based on the embroidery method with electro-textile material [22]. Comparing to conventional conductive material, the electro-textile materials are especially favorable due to its superb flexibility and light weight nature. Its seamless integration with the normal clothes makes it good candidate for wearable applications. With the modern computerized embroidery machines that are fast and cost effective in pattern generation, embroidery-based antennas have large potentials to meet many of the system requirements for wearable applications.

The major parameters of interest for a certain type of eletro-textile include the conductivity, the mechanical strength and the fitness for embroidery fabrication. Silver and copper based electro-textiles are generally favorable for applications requiring high conductivity. While for applications require high mechanical strength, carbon based textiles Kevlar and Zylon are preferred [23]. Combining the highly conductive metals with the high strength textiles by depositing layers of conductors on the fibers is one of the most attractive methods to produce the appropriate electro-textiles for the embroidery fabrication. The electro-textiles typically used for antenna and RF applications have large variations of linear resistivity depending on the applications [24].

In the second section of this work, we focus on wearable antenna design based on electro-textile material. The embroidery-based electro-textile patch antennas are different to the

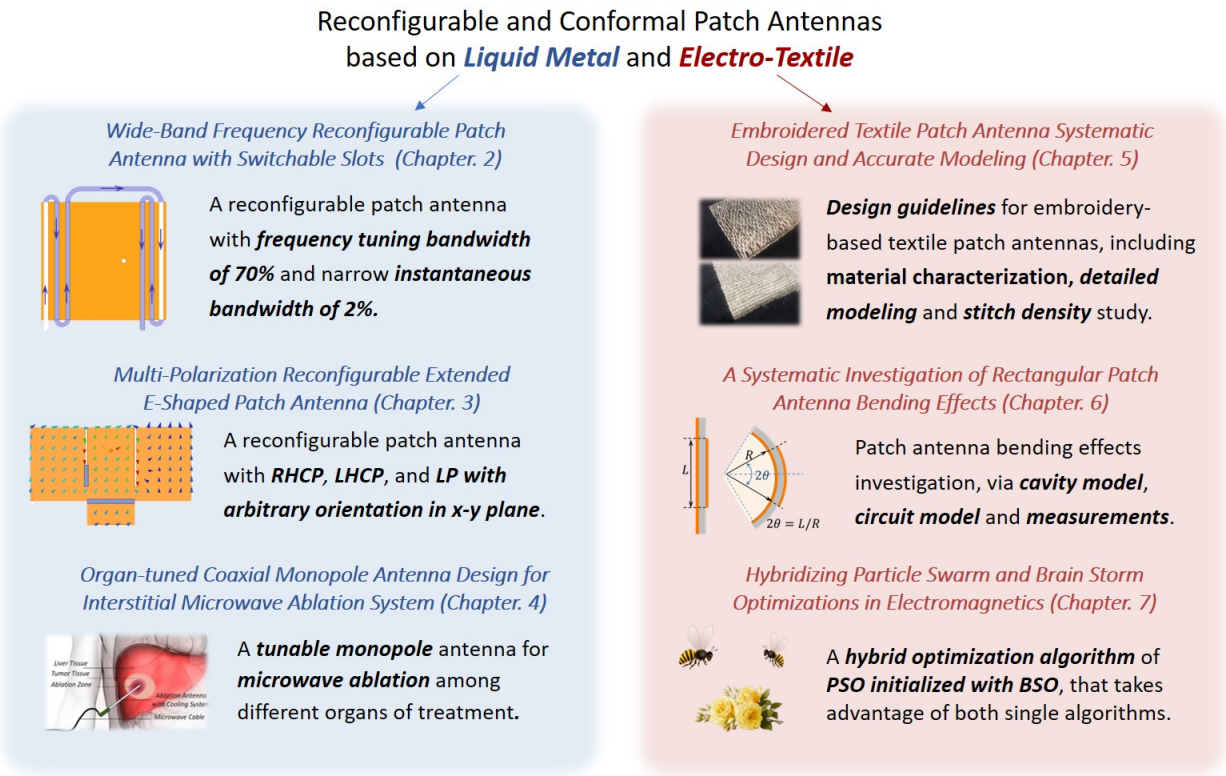

Figure 1.4: The dissertation consists of two parts: reconfigurable antennas with liquid metal tuning, and conformal antennas based on electro-textiles.

ones fabricated with bulk conductive materials since the characterization of the detailed embroidery structures need to be carefully incorporated into the antenna design procedures. We present the methodology of material characterization and modeling strategies for embroidered textile rectangular patch antennas. The effect of bending the rectangular patch onto a cylindrical surface is also investigated, via analytical approach, circuit model and measurements.

1.4 Organization of this Dissertation

The dissertation is organized into two parts, as depicted in Fig. 1.4. We first discuss reconfigurable antennas utilizing liquid metal and 3D printed microfluidics as an emerging reconfiguration technique (from Chapter 2 to 4), and then switch to the discussions

on embroidery-based conformal antennas and optimization techniques (from Chapter 5 to Chapter 7).

Three antenna designs are proposed in the first part of the dissertation. Some representative prototypes are shown in Fig. 1.5. In Chapter 2, a wide-band frequency reconfigurable patch antenna is introduced. By incorporating three pairs of parallel composite liquid metal tuning slots, a 70% frequency tuning bandwidth is achieved, with a 2% instantaneous bandwidth for each frequency tuning state. A semi-empirical formula based on physical interpretation, full-wave simulation and particle swarm optimization is presented. It is well known that building reliable microfluidics on printed circuit boards (PCB) presents a great challenge of upscaling in the microfluidics society. One of the major difficulties is the incompatibility between PCB and the popular microfluidic material PDMS [25]. In Chapter 2, we for the first time explore the option of integrating 3D printed microfluidics onto PCB for the application of reconfigurable antennas. The prototyping process and liquid handling procedures demonstrated here provide hands-on details including material selection, surface treatment, etc. In Chapter 3, we propose the second liquid metal reconfigurable patch antenna design: a multi-polarization reconfigurable patch antenna. It achieves circular polarization states in both rotations and linear polarization states in arbitrary orientations with pneumatic driven liquid metal reconfiguration. A thorough and comprehensive circuit model analysis for asymmetric E-shaped patch antenna is demonstrated, decomposed into horizontal and vertical modes. Using the circuit model, we explicitly proved that the two modes can be considered independently with their relative phase and magnitude manipulated based on designing the asymmetric geometry, which is the underlying strategy in the proposed multi-polarization reconfigurable patch antenna. The two designs introduced in Chapter 2 and 3 are both simulated, prototyped and measured with fully-implemented liquid metal reconfiguration. In Chapter 4, we explore the use of liquid metal reconfiguration in biomedical application by introducing an organ-tuned coaxial antenna for interstitial microwave ablation. Analytical solutions for insulating monopole immersed in lossy dielectric media is described. And based on that, a coaxial antenna that can be adaptively tuned with liquid metal to maintain the optimal impedance matching is proposed. Experimental

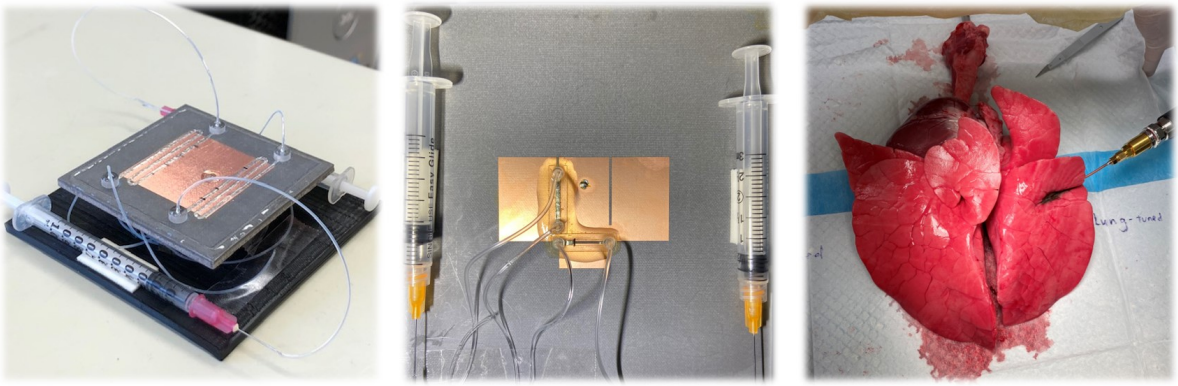

Wide-Band Frequency Reconfigurable Patch Antenna with Switchable Slots (Chapter. 2)

Multi-Polarization Reconfigurable Extended E-Shaped Patch Antenna (Chapter. 3)

Organ-tuned Coaxial Monopole Antenna Design for Interstitial Microwave Ablation System (Chapter. 4)

Figure 1.5: Three antenna designs are introduced in the first part of this dissertation from Chapter 2 to 4. The application of liquid metal reconfiguration is explored for wide-band frequency reconfiguration, multi-polarization reconfiguration, and organ-specific ablation antenna for cancer treatment.

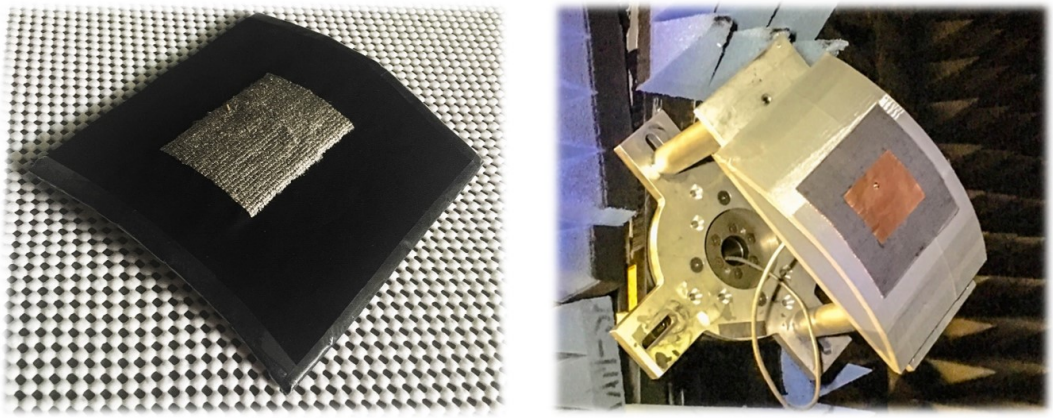

Embroidered Textile Patch Antenna Systematic Design and Accurate Modeling (Chapter. 5)

A Systematic Investigation of Rectangular Patch Antenna Bending Effects (Chapter. 6)

Figure 1.6: Representative prototypes developed in the second part of this dissertation in Chapter 5 and 6, for the study of embroidery-based textile patch antenna and the cylindrical bending effects.

validations are performed in ex vivo porcine liver and lung tissue.

Next, the dissertation continues to the second part, devoting to the discussion on embroidery textile antenna systematic design and accurate modeling, bending analysis and optimizations. Some representative prototypes are shown in Fig. 1.6. In Chapter 5, we

introduce design guidelines for embroidery-based electro-textile patch antennas, including detailed full-wave modeling and stitch density study. These design and modeling strategies are then validated through measurements. We then investigate the patch antenna bending effects in Chapter 6. The resonant frequency variations and radiation pattern variations have been studied by full-wave simulation, analytical solution, circuit model and measurements on real prototypes. One of the main objectives of this work is to generate useful design curves based on the definition of bending angle, to help antenna engineers to incorporate the effects of bending more efficiently for various wearable applications. PSO and BSO are both evolutionary global optimization techniques based on the movement and intelligence of swarms. We start from revisiting the concepts and algorithms of PSO and BSO. The advantages of the two algorithms are then investigated through a comparison study using a bench marking function. The hybrid optimization is then proposed and validated with the generalized circuit model of patch antenna, which has been extensively utilized throughout the chapters in this dissertation. It is observed that the BSO-PSO hybrid algorithm could benefit from taking advantages of both PSO and BSO, and therefore outperforms single technique with PSO or BSO in some electromagnetic related optimization problems. To conclude this dissertation, several broad statements are made about the contributions of this work provided to the scientific and engineering community.

Part I

Reconfigurable Antennas based on Liquid Metal Eutectic Gallium Indium

CHAPTER 2

Frequency Reconfigurable Patch Antenna with Switchable Slots

The rapid development of wireless communication and emerging applications have led to great demand for compact wireless systems that satisfies demanding multiband requirements. Antennas with wide-band frequency reconfigurability are the essential enabling components for this endeavor [26]. One of the potential applications for frequency reconfigurable antenna is the cognitive ratio system. In these systems, a wide-band sensing antenna such as an ultra-wideband antenna [27] is continuously monitoring the wireless channel searching for unoccupied frequency bands, and a wide-band reconfigurable transmit/receive antenna with narrow instantaneous bandwidth is required for data transfer [28]. In order to achieve reconfiguration of the radiation characteristics, switching or tuning elements are commonly used to electrically modify the antenna radiation characteristics, such as microelectromechanical systems (MEMS) switches [29], p-i-n diodes [30], varactor diodes [9], or combination of those [31].

Comparing to existing reconfiguration methods, liquid metal based reconfiguration has been shown as a promising technique in terms of lower loss, more power handling, and greater tuning range [11]. In particular, liquid metal eutectic gallium indium (EGaIn) demonstrates low toxicity, high conductivity (3.4×10^6 S/m) and very good flexibility [12]. Slot-loaded patch antennas have been widely used in wireless communication, due to their low-profile, low-cost feature and capability of realizing various functionalities. It has been shown that dual-band operation with good impedance matching could be achieved using patch antenna with composite slots, with the frequency-ratio of the two frequency bands controlled by the lengths of the slots [32]. However, the capability of wideband continuous frequency

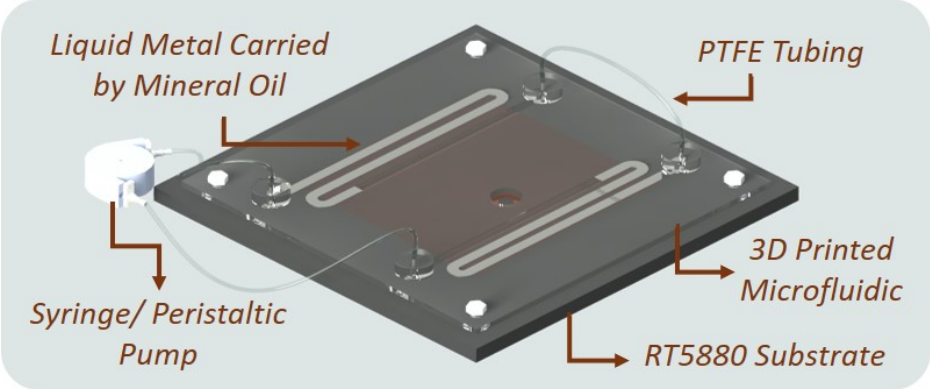

Figure 2.1: The proposed wide-band frequency reconfigurable patch antenna with switchable slots (PASS) based on liquid metal tuning in 3D printed microfluidics.

reconfiguration with liquid metal tuning elements has not been explored. Advanced 3D printing technologies has been widely used in the development of microfluidic chips [33], but have not been utilized in liquid metal reconfigurable antennas. Comparing to traditional soft lithography, 3D printing offers a cheaper and faster solution in building complex fluidic design.

In this chapter, we propose a wide-band and continuous frequency reconfigurable patch antenna with switchable slots (PASS) based on manipulating liquid metal in a 3D-printed microfluidic channel. The frequency reconfiguration is achieved by continuous movement of the liquid metal droplet over the channel that covers the slots. By tuning and switching the liquid metal loaded slot in the designed microfluidic channel, a wide frequency tuning bandwidth of around 70% is achieved with a 2% instantaneous bandwidth. EGaIn carried by mineral oil has been used for prototyping and measurements. A schematics for the proposed patch antenna with liquid metal and microfluidics is illustrated in Fig. 2.1.

The chapter has been organized as follows: in Section II the dual-band operation mechanism is explained and a semi-empirical formula is established based on fitting the simulation results with particle swarm optimization (PSO); in Section III, the multi-slot patch antenna with switchable slots is proposed with the wide-band frequency tuning demonstrated by full-wave simulations; in Section IV, a feasible process to integrate 3D printed microfluidic channel to patch antenna is developed. The prototype is fabricated, assembled and measured

with syringes for liquid pumping. Measurement results presented in Section V demonstrate good agreement with the full-wave simulations.

2.1 Dual Band Operation of Patch Antenna with Composite Slots

In this section, the basic configuration of a rectangular patch antenna with two composite slots is described and the physical insights of the dual-band operation characteristics is illustrated by current distribution plot at the two frequencies of resonance. Simple empirical formulas to predict the two resonant frequencies are given based on the parameters extracted by fitting the simulation results using particle swarm optimization.

Starting from an unslotted rectangular patch antenna excited horizontally, as shown in Fig. 2.2 (a), the first three modes in the cavity are the TM10, TM20 and TM30 modes. TM20 mode generates broadside null and TM30 produce grading lobes since the two radiating slots are separated more than a half wavelength (at the frequency of resonance of the TM30 mode). When the two slots are created close to the two radiating edges and are cut through on one side, it results in a minor perturbation of the TM10 mode, and also a relatively strong perturbation of the TM30 mode, since the slots are located at where the current of TM30 is significant. The modified current distribution for the two modes are depicted in Fig. 2.2 (b) as TM10' and TM30'. The perturbed TM30 mode has a much lower resonant frequency and the radiation pattern becomes similar to that of the TM10 mode.

The geometries of a slot-loaded rectangular patch antenna is provided in Fig. 2.3 (a). The patch is printed on 125 mil RT5880 substrate. Two slots with length L_s, width W_s and separation P_s are etched close to the two radiating edges. A similar antenna topology has been studied in [34] for the case with slots cut from center. In this work, we focus on the topology in Fig. 2.3 (a) with the two slots cut from the edges in a center-symmetric manner. The simulation result for S_{11} in 2.4 (a) clearly shows the dual-band resonance characteristics, with the TM10' mode at $f_{10} = 2.1$ GHz and the TM30' mode at $f_{30} = 2.85$ GHz. The simulated vector current plots for the two modes of resonance are shown in Fig. 2.3 (b), which shows close resemblance to the current direction depicted in Fig.3.4. In

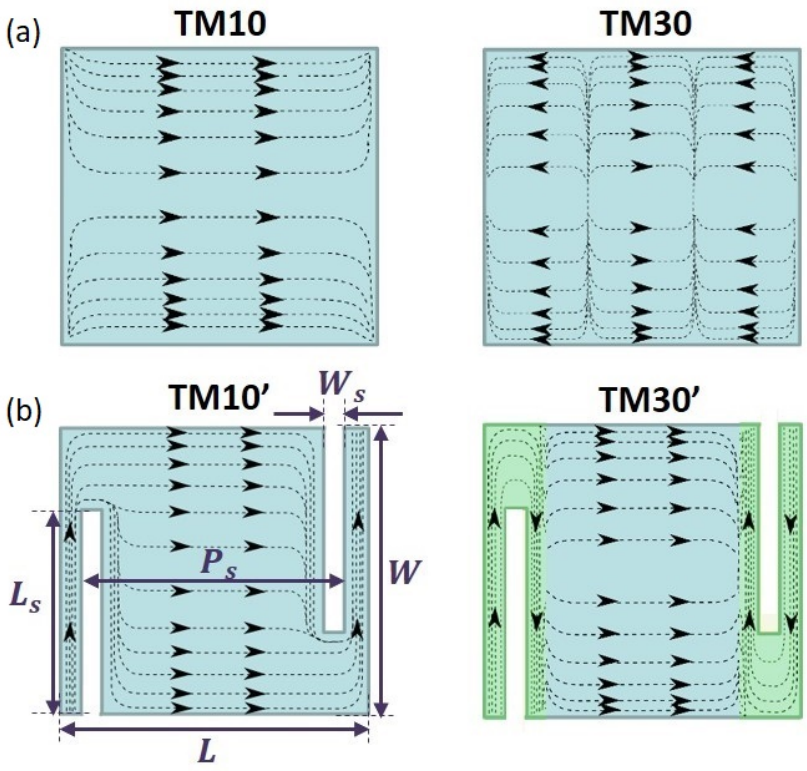

Figure 2.2: Current distribution for the original and perturbed TM10 mode and TM30 mode. (a) The original current distribution for unslotted rectangular patch, and (b) the perturbed TM10' mode and TM30' mode with two narrow slots cut close to the two radiating edges.

addition, the E plane pattern plot as shown in Fig. 2.4 (b) demonstrates that a radiation pattern very similar to the TM10' mode is generated by the TM30' mode by loading the patch antenna with two narrow slots.

The resonant frequencies of the perturbed TM10' and TM30' modes depends on the length of the slots L_s and the separation between the two slots P_s. In order to find the effective correlation between the design parameters and the two resonant frequencies f_{10} and f_{30}, simple semi-empirical formulas are generated to predict f_{10} and f_{30}. The simple formulas evolve from the well-established equations for rectangular patch antenna, by including modified terms based on fitting the simulation results using particle swarm optimization (PSO). The simple formula for the perturbed resonant frequency of TM10' is given as [35]:

$$f_{10} = \frac{c}{2(L + \Delta L + \Delta L')\sqrt{\epsilon_e(W)}} \tag{2.1}$$

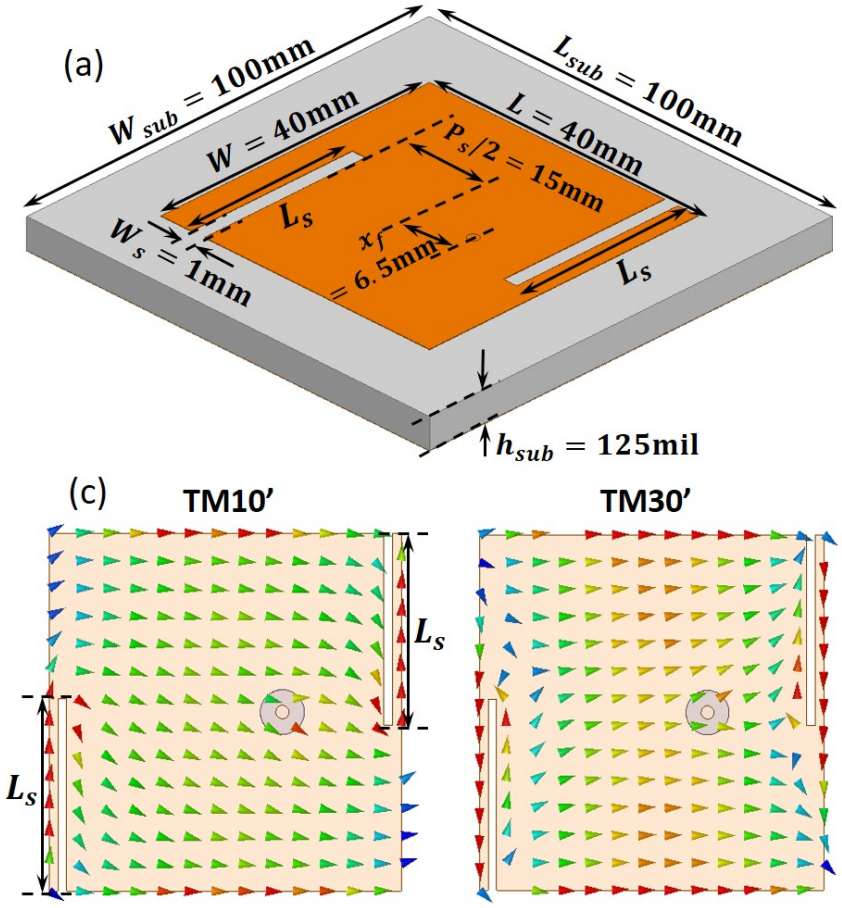

Figure 2.3: (a) A patch antenna with two composite slots cut close to the two radiating edges. (b) The current vector plot from full-wave simulation for TM10' and TM30' modes.

$$\Delta L = 0.824h\frac{(\epsilon_r + 0.3)(W/h + 0.264)}{(\epsilon_r - 0.26)(W/h + 0.8)} \tag{2.2}$$

$$\epsilon_e(x) = \frac{\epsilon_r + 1}{2} + \frac{\epsilon_r - 1}{2}(1 + \frac{10}{x/h})^{-1/2} \tag{2.3}$$

where c is the speed of light in free space; L and W are the length and width of the patch as denoted in Fig. 2.3 (a); ΔL is the term that accounts for the effects of fringing field for rectangular patch antenna; h and ϵ_r are the thickness and relative dielectric constant of the substrate; and the term ϵ_e gives the effective dielectric constant. The perturbation due to the two slots is modeled by the term $\Delta L'$, which is assumed to be linearly dependent on L_s and P_s, based on inspection of the current distribution for the modified TM10' mode:

$$\Delta L' = L(a_1\frac{L_s}{W} + b_1\frac{L - P_s}{L}) \tag{2.4}$$

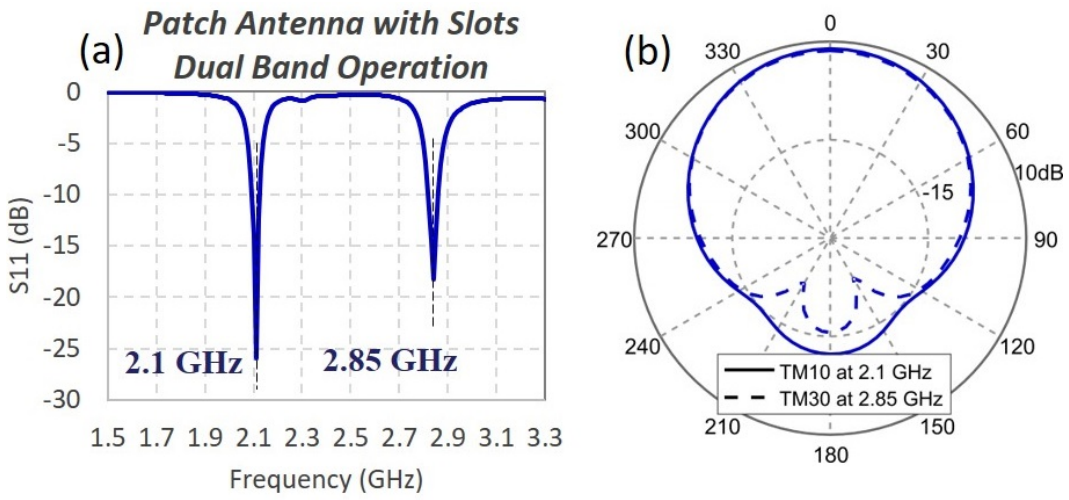

Figure 2.4: (a) The simulation results of S_{11} for the patch antenna with dual-band characteristics. (b) The E plane radiation pattern of the patch antenna with slots at the frequencies of 2.1 GHz and 2.85 GHz.

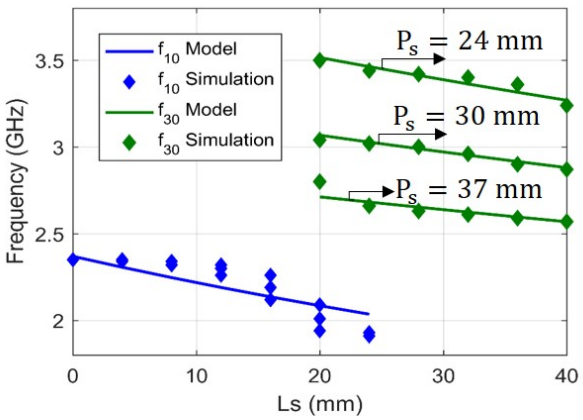

- ***Number of Dimensions: 5 ;***
- ***Number of Particles: 21 ;***
- ***Number of Iterations: 800 ;***

Final Coefficients Found by PSO (dimensionless)

a_1	b_1	a_3	b_3	c_3
0.294	0.000	0.761	0.173	0.437

Figure 2.5: The simulated f_{10} (blue markers) and f_{30} (green markers) are plotted with respect to L_s for three cases of P_s (24 mm, 30 mm, and 37 mm). The fitted f_{10} (blue line) and f_{30} (green lines) using the semi-empirical formulas demonstrate good agreement with the simulations. The final coefficients given by PSO are listed in the table.

where a_1 and b_1 are undetermined coefficients for TM10'.

For the TM30' mode, inspection of the highlighted portion of the current plot in Fig. 3.4 reveals the resemblance of the portion that encircles the slots to an half-wavelength folded open-circuit stub. The effective dielectric constant is therefore determined by relating the

folded stub to a section of microstrip line with the width of $(L - P_s)/2$. The resonant frequency of TM30' is therefore formulated as:

$$f_{30} = \frac{c}{2(a_3 L_s + b_3 W_s + c_3 P_s)\sqrt{\epsilon_e(\frac{L-P_s}{2})}} \tag{2.5}$$

Similarly, a_3, b_3 and c_3 are unknown coefficients for TM30'.

The five coefficients are determined by fitting the simulated TM10' resonant frequencies in HFSS for varying L_s and P_s within the range of:

$$0 \leq L_s \leq 40\,\text{mm}, \quad 24\,\text{mm} \leq P_s \leq 37\,\text{mm} \tag{2.6}$$

As shown in Fig. 2.5, the simulated f_{10} (blue markers) and f_{30} (green markers) are plotted with respect to L_s for three cases of P_s (24 mm, 30 mm, and 37 mm). The curve fitting is done by PSO, which has been shown to be effective in optimizing multidimensional problems [36]. The fitness function is defined by the normalized frequency deviation Δ_f to produce the set of coefficient that gives the closest fitness between the formulas and simulations:

$$\Delta_f = \frac{1}{f_0 M}\{\sum[(f_{10s} - f_{10f})^2 + (f_{30s} - f_{30f})^2]\}^{1/2} \tag{2.7}$$

where f_0 is the reference frequency chosen as 2.4 GHz, M is the number of cases we simulated, f_{10s} and f_{10f} are the simulated and fitted TM10' resonant frequency f_{10}, and similarly, f_{30s} and f_{30f} are the simulated and fitted f_{30}.

We assigned 21 particles to search in the 5 dimensional space. A maximum value of 800 iterations is assigned as the termination criterion. Convergence plots for the average fitness and the global best fitness are shown in Fig. 2.6. Stable fitness values are maintained in the last few iterations, which indicates the convergence behavior of the swarm. The final coefficients obtained by PSO are shown in the table in Fig. 2.5, which give the blue and green lines in the plot. It is worth noting that the final coefficient b_1 is determined as 0, indicating that the resonant frequency of TM10' mode is almost independent to the separation between the two slots P_s, and the perturbation term $\Delta L'$ is only a linear function of the length of the slot L_s. This is also confirmed by observing the fullwave simulation results in Fig. 2.5,

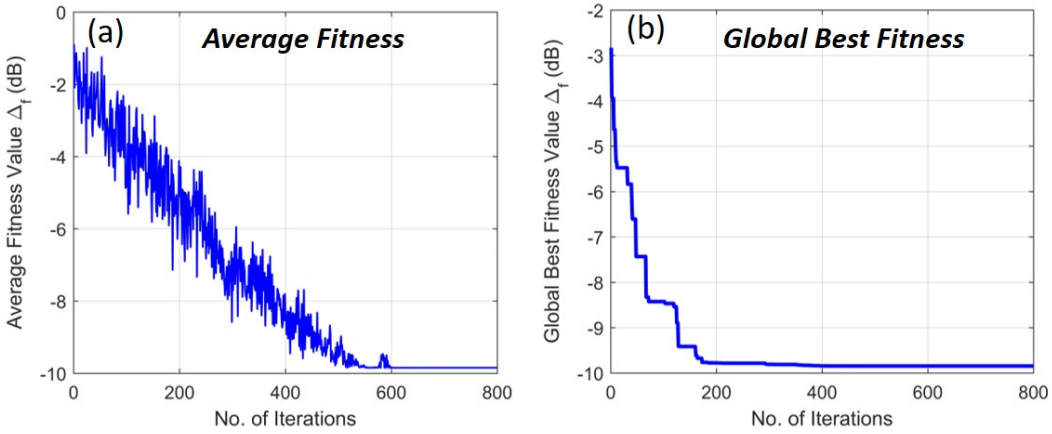

Figure 2.6: Convergence plots for the average fitness (a) and the global best fitness (b) within the 800 iterations of PSO. Stable fitness values are maintained in the last few iterations, indicating the convergence behavior of the swarm.

but only for cases with relatively large P_s ($P_s > L/2$) so that the TM10 mode is not very strongly modified and equation (1) still holds.

2.2 Multi-Slot PASS Antenna for Wide-band Continuous Frequency Tuning

With the dual-band characteristics analyzed for patch antenna with slots, the multi-slot PASS for wide-band frequency reconfiguration is introduced in this section. A basic PASS structure with composite tuning slots is used as a starting point. The antenna was built on a RT5880 substrate, with the dimensions listed in Fig. 2.7 (a). As shown in Fig. 2.7 (b), the patch antenna with slots was simulated in HFSS. Two composite slots with width W_s located at position $P_s = 24$ mm are cut through on copper. To simulate the effect of injecting liquid metal, two rectangular blocks with conductivity of 3.4 $\times 10^6$ S/m are inserted to cover the two slots. As the length of the blocks varied from 0 mm to 40 mm, the slot lengths L_s are varied from 40 mm (completely empty) to 0 mm (completely filled by with liquid metal). According to the simulated S_{11} for different L_s, the f_{10} frequency band of 1.9 GHz to 2.35 GHz is covered by slot length from 0 to 20 mm, while the f_{30} frequency band of 3.2 GHz to

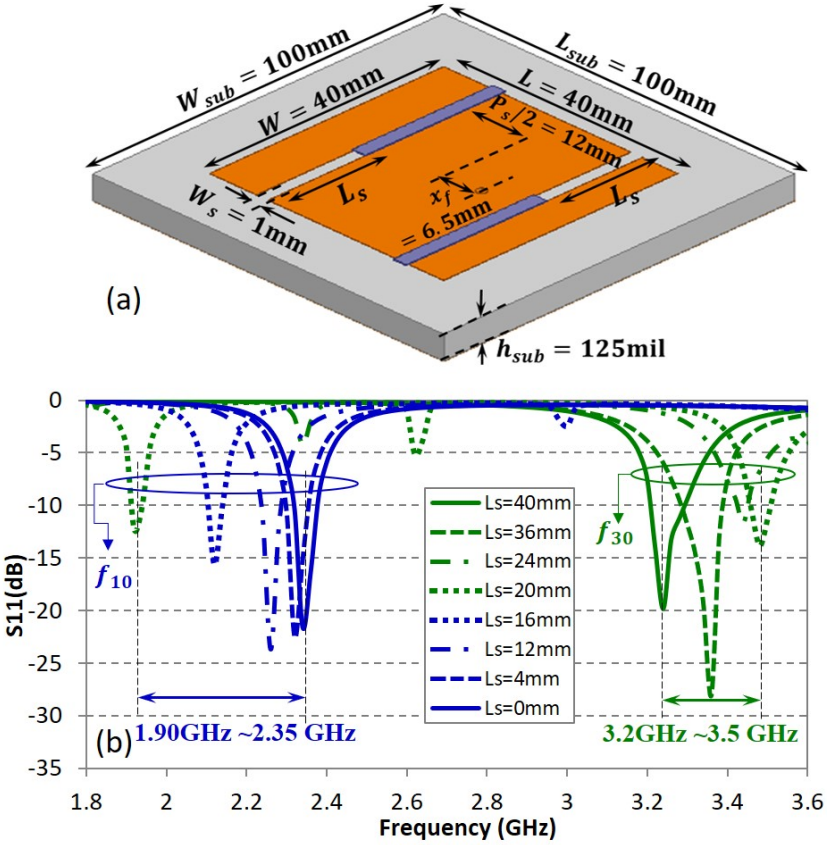

Figure 2.7: (a) A basic PASS structure with two composite tuning slots and (b) the simulation results of S_{11} for continuous frequency tuning by varying the slot lengths L_s. The separation between the slots is fixed as $P_s = 24$ mm.

3.5 GHz is covered by slot length from 20 to 40 mm, giving two continuous frequency tuning bands. In practical implementation, the length of the slot L_s is controlled by the amount of liquid metal pumped into the two microfluidic channels and bridging the gap formed by the slots. Thus, by tuning the length of liquid metal filling, the length of the slots could be changed continuously, and frequency reconfiguration in two continuous frequency bands is achieved.

The simulated radiation pattern in E plane and radiation efficiency for different cases of L_s is shown in Fig. 2.9 (a) and (b), respectively. As expected from the analysis in Section II, the simulated antenna radiation pattern, peak directivity and radiation efficiency has not changed significantly with the slot length tuned by liquid metal, since the modified TM30

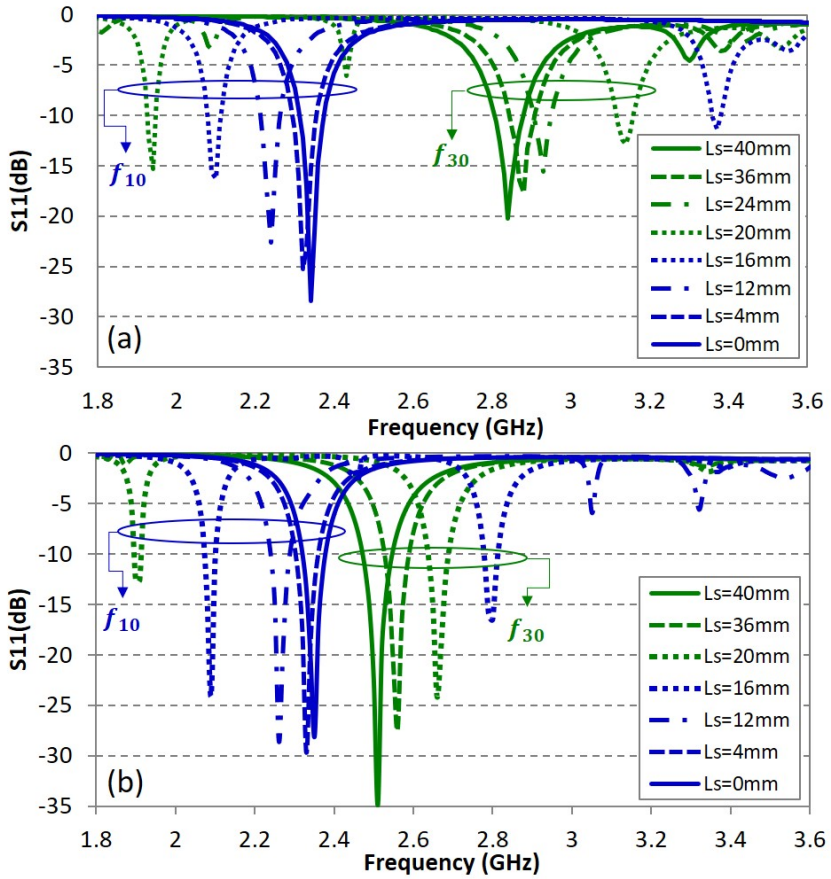

Figure 2.8: The simulated S_{11} with P_s increased to 30 mm (a) and 37 mm (b), respectively. The f_{30} band has been shifted while the f_{10} band is not significantly affected by changing the separation distance P_s.

mode maintain the similar radiation pattern to the fundamental TM10 mode. There is a slight decrease in radiation efficiency for intermediate states ($L_s = 12, 20$, and 24 mm) than the starting and final states ($L_s = 0, 40$ mm), possibly due to the reason that intermediate states have more current resides on the narrow portion of the patch with slots. The radiation efficiency listed in Fig. 2.9 (b) accounts for the conductive loss of EGaIn. However, since the conductivity of EGaIn is relatively high (3.4×10^6 S/m), the degradation in radiation efficiency due to the loss of liquid metal is not significant.

According to the analysis in Section II, the lower-frequency band corresponding to TM10' mode is not very much affected by the separation between slots P_s, while the higher-frequency tuning band corresponding to TM30' mode can be relocated by adjusting the separation

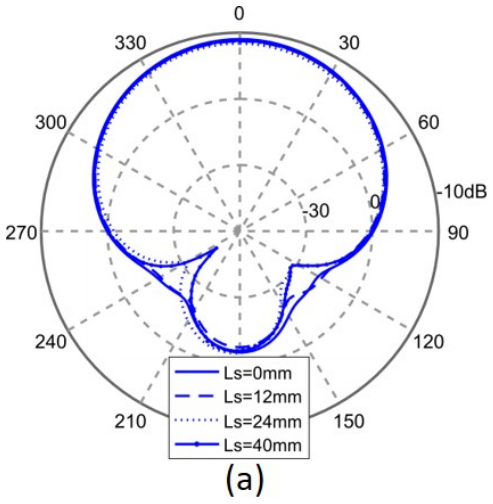

Slot Tuning Ls	Frequency Center	Radiation Efficiency
0 mm	2.35 GHz	99.1%
12 mm	2.31 GHz	96.2%
20 mm	2.80 GHz	98.7%
24 mm	2.67 GHz	97.1%
32 mm	2.64 GHz	99.1%
40 mm	2.55 GHz	99.2%

(b)

Figure 2.9: The simulated radiation pattern in E plane (a) and radiation efficiency (b) for different cases of L_s. The simulated antenna radiation pattern, peak directivity and radiation efficiency has not changed significantly with the slot length tuned by liquid metal

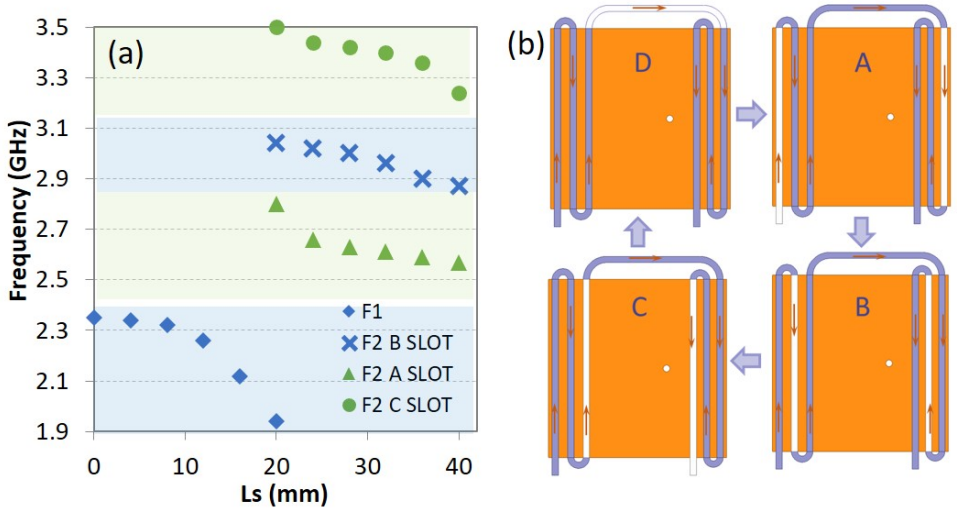

Figure 2.10: (a) A wide and continuous frequency tuning band from 1.9 GHz to 3.5 GHz is achieved by combining three pairs of slots in one patch design. (b) Scenario A to C corresponds to patch with the composite slots with 3 different cases of separation distance P_s.

between the two composite slots P_s. The simulated S_{11} with P_s increased from 24 mm to 30 mm and 37 mm are shown in Fig. 2.8 (a) and (b), respectively. Comparison between Fig.

2.7 (b) and Fig. 2.8 clearly demonstrate the shift of f_{30} band with different P_s while the f_{10} band is almost unaffected for the three different cases of P_s. According to the simulation results, the f_{30} frequency bands corresponding to different P_s are: 2.5 GHz to 2.8 GHz for P_s = 37 mm; 2.8 GHz to 3.2 GHz for P_s = 30 mm; 3.2 GHz to 3.5 GHz for P_s = 24 mm; while f_{10} band is maintained as 1.9 GHz to 2.35 GHz for all three cases. Therefore, by combining three pairs of slots in one patch design, the available frequency tuning bands for different P_s can be superimposed, giving a wide and continuous frequency tuning band from 1.9 GHz to 3.5 GHz, with the number of achievable states only limited by the accuracy of slot tuning.

Tuning and switching the slots can be done by injecting liquid metal into the designed microfluidic channel attached on top of the patch antenna. As shown in Fig. 2.10, the meander microfluidic channel was designed to sweep over the 3 pairs of composite slots on the patch antenna. During the continuous pumping of liquid metal droplet, there is always a pair of slots with unfilled liquid metal and length of the slot is changed by pumping. By connecting the two terminals with a peristaltic pump to connect the two terminals, the liquid metal can be recycled and re-injected into the microfluidics after one cycle of pumping. In Fig. 2.10 (b), scenario A to C corresponds to patch with the composite slots with 3 different cases of P_s. By integrating three pairs of composite slots on one patch, a 70% continuous frequency tuning range and a 2% instantaneous bandwidth are simultaneously achieved.

2.3 Prototype Fabrication and Operation

The prototype frequency reconfigurable PASS antenna was fabricated by attaching the 3D printed microfluidic module to the patch antenna with patterned adhesive layer as illustrated in Fig. 2.11. The microfluidic module was printed by a Polyjet 3D printer (Eden 260V) using optical-clear acrylic material (VeroClear) from Stratasys Inc. A resolution of 0.016 mm was claimed by the manufacturer. The inlet/outlet stubs were integrated into the 3D printed fluidic module. Copper thickness compensation was built-in to ensure the seamless fit between microfluics and PCB substrate. The patch antenna with slots was made on a

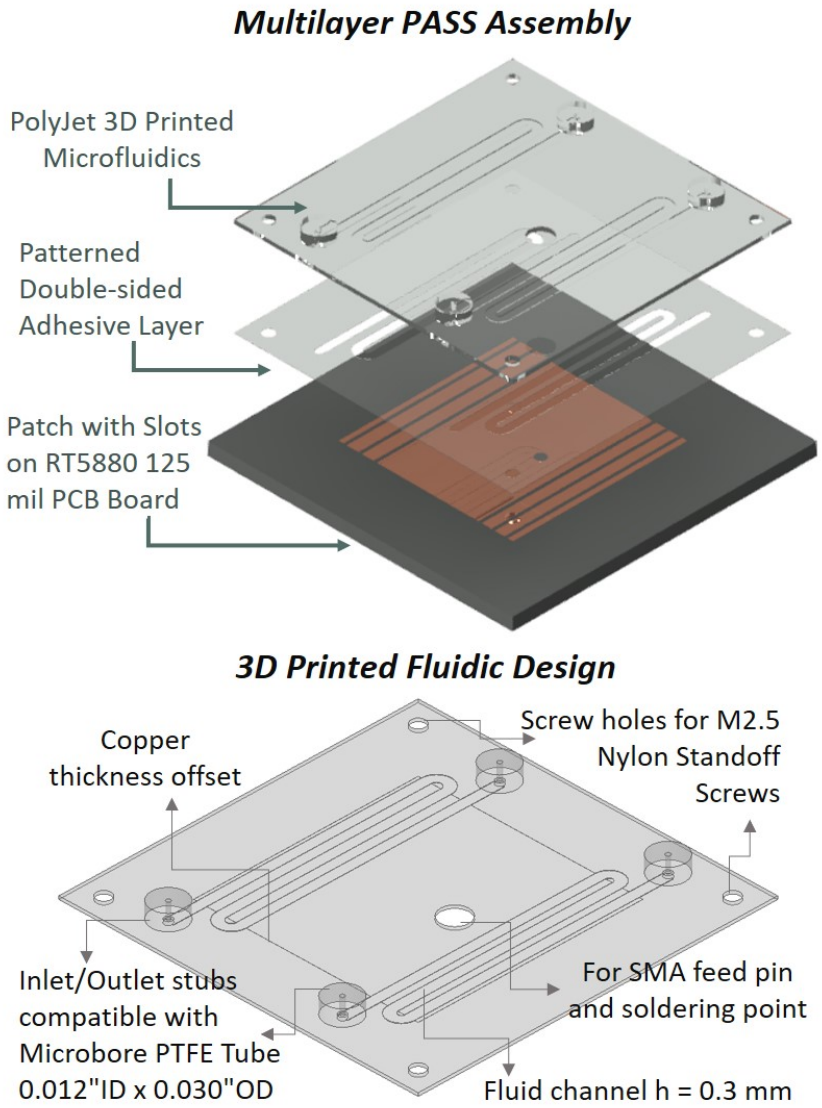

Figure 2.11: The multilayer prototype assembly and microfluidic design. The prototyped wide-band frequency reconfigurable PASS is assembled by attaching a 3D printed microfluidics to the patch antenna on PCB substrate via a patterned double-sided adhesive layer.

125 mil RT5880 substrate.

Two parts were bonded together using 3M's double sided adhesive tape. The tape was patterned with a cutter (silhouette portrait), and adhesive material inside the channel was removed. To tightly seal the channels, mechanical compression was applied at the elevated temperature of 85°C for 10 minutes, and then in room temperature over night. During the

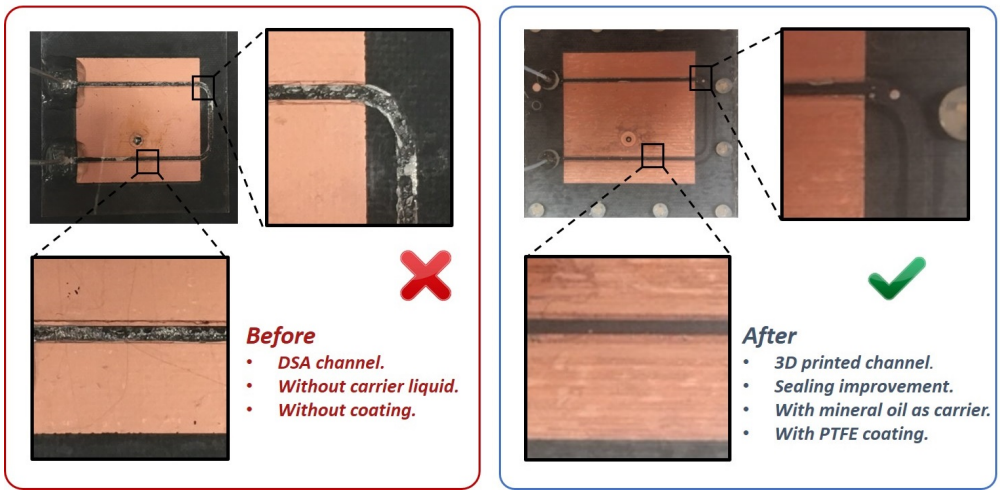

Figure 2.12: Comparison of the channel quality with and without the optimized prototyping process after one cycle of liquid metal flowing inside the microfluidic channel. The use of 3D printed fluidics and channel treatment procedures helps prevent the formation of skin residue caused by liquid metal oxidation.

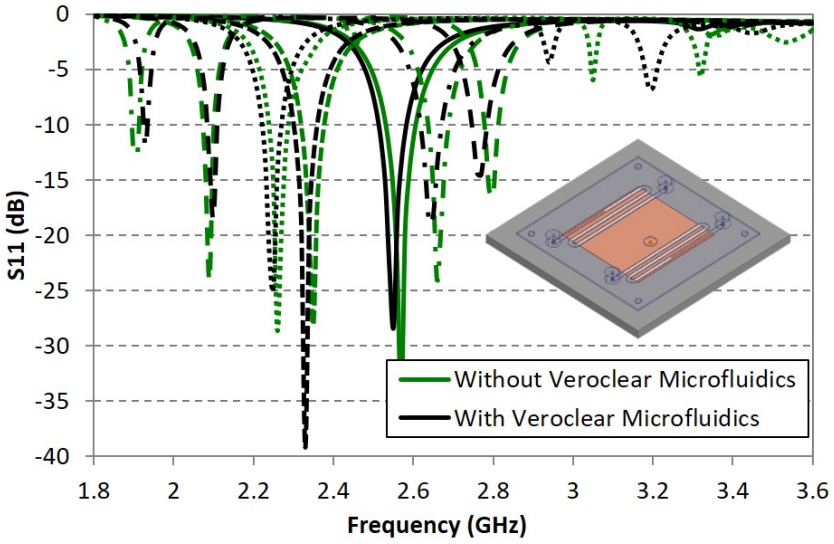

Figure 2.13: The simulated S_{11} with (black curves) and without (green curves) the 3D printed channel for different slot length with separation of 37 mm.

compression, a specially designed 3D printed module was used to accommodate inlets and evenly apply the force to entire structure.

Polytetrafluoroethylene (PTFE) tubes were then inserted to the inlet and outlet and

sealed by Ultraviolet (UV) cured epoxy. In this prototype, 1mL syringes were attached to the PTFE tube to manipulate liquids.

Skin residue generated by EGaIn oxidation is considered a great challenge in operating EGaIn based liquid metal antennas. In order to further improve the channel quality and prevent the formation of skin residue, the channel was then passivated by flushing PTFE dispersion surfactant and then air dried at room temperature, leaving a uniform finish of PTFE coating on channel walls, as reported in [11].

The proposed fabrication process was able to construct liquid metal antenna operating EGaIn with minimum skin residue. Fig. 2.12 compares the channel quality with and without the optimized prototyping process after one cycle of liquid metal flowing inside the microfluidic channel. Compared with our previous design built with double sided adhesive tapes, the high-resolution Polyjet 3D printing has improved the channel quality significantly. After one cycle of EGaIn actuation, the channel remains clean and reusable. We believe this is contributed to multiple efforts in promoting the sealing tightness and PTFE surface coating.

The 3D printing material Veroclear has a reported dielectric constant of $\epsilon_r = 3.1$ and a loss tangent of $\tan\delta = 0.02$ [37]. Effects of the presence of microfluidic channel are investigated in simulation. As shown in Fig. 2.13, the simulated S_{11} with and without the 3D printed mincrofluidics for different L_s and $P_s = 37$mm are plotted and compared. Presence of the fluidic channel on top of the patch antenna only results in a slight lower frequency shift by 0.02 to 0.03 GHz, since the thickness of the channel is relatively small comparing to the wavelength ($< 0.005\lambda$ at the frequency of 2.4 GHz).

Eutectic gallium-indium (EGaIn) carried by mineral oil has been used for prototyping and measurements. Mineral oil was selected as the carrier liquid since it is transparent and low loss in radio frequency ($\tan\delta < 0.01$ [38]) compared to water with impurity. Liquid metal and mineral oil were loaded into the syringe and injected into the PASS prototype as illustrated in Fig. 2.15. A reservoir containing both liquid metal and mineral oil was made by mixing them in a 1 mL vial, where they stratified and layered by themselves. The channel was first filled with mineral oil and then with a EGaIn plug by withdrawing from respective

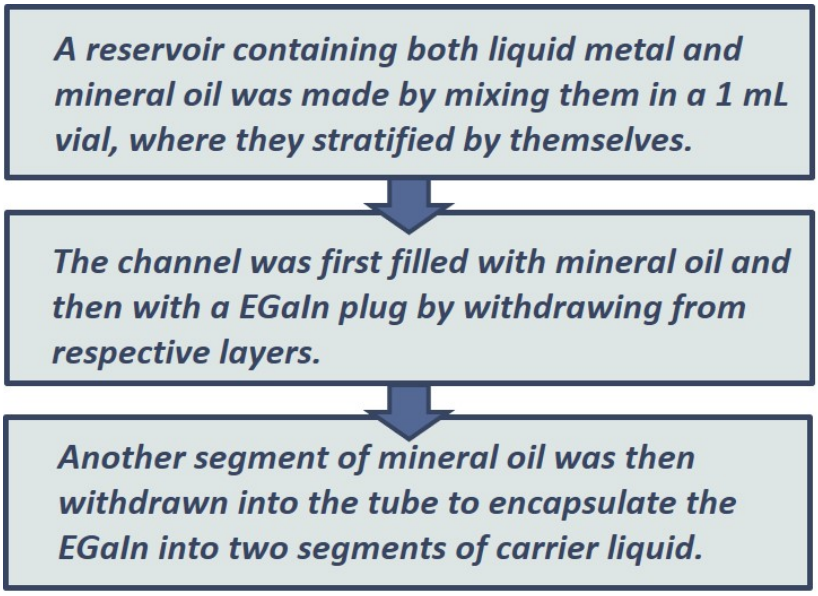

Figure 2.14: Instructions on liquid metal and mineral oil loading procedures.

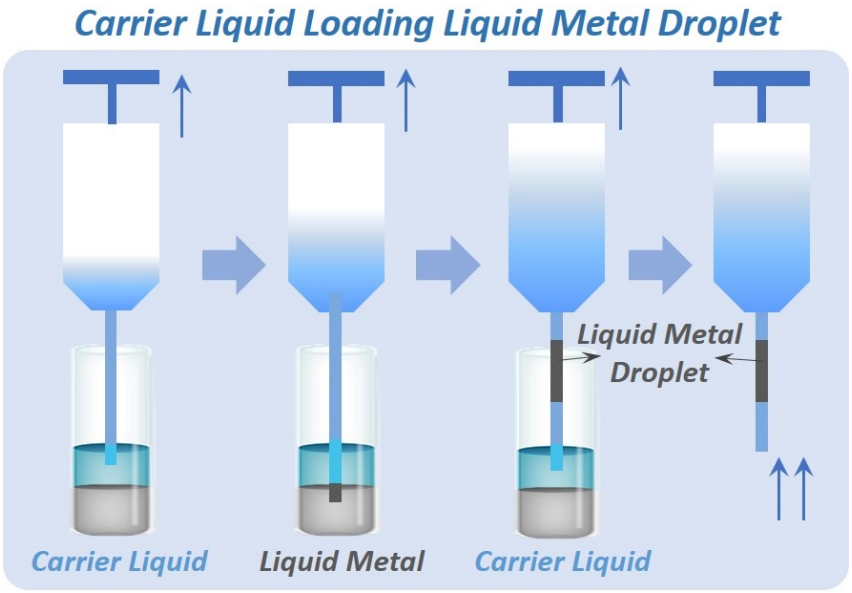

Figure 2.15: Carrier liquid of mineral oil has been used to load the liquid metal plug into the syringe and pumped into the designed fluidic channel that covers and reconfigure the slots on the patch antenna.

layers. Another segment of mineral oil was then withdrawn into the tube to encapsulate the EGaIn plug into two segments of carrier liquid in order to prevent the contact with oxygen and the formation of skin residues. The use of carrier liquid and PTFE channel coating

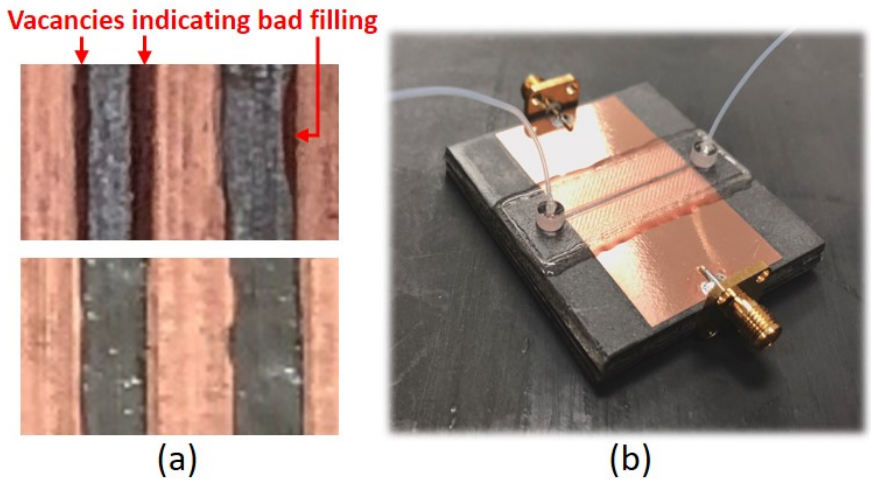

Figure 2.16: (a) Comparing the two microfluidic channels with different filling condition in the region between copper and ceiling, and (b) a transmission line switch with a lateral slot in the middle of the line is built to test the performance of liquid metal slot tuning.

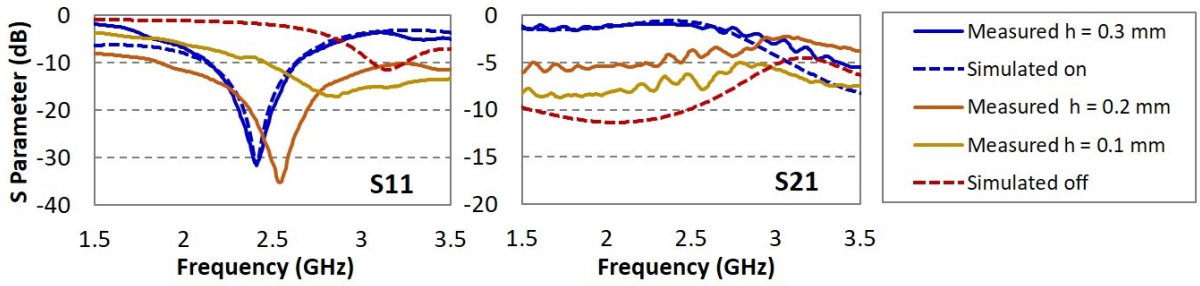

Figure 2.17: The two port S parameters S_{11} and S_{21} measured with liquid metal for channel height of $h = 0.1$, 0.2, 0.3 mm and compared with the simulation results.

helps reduce the formation of skin residues left by EGaIn plugs. After one cycle of EGaIn actuation, the channel remains clean and reusable.

The height of microfluidic channel is found to be an important design parameter through our trials. Thinner channel reduces the loaded EGaIn volume, but shows worse contact to the underlying patch. This is because EGaIn won't fill in the gap between copper and the channel ceiling when it is too narrow, as shown in Fig. 2.16 (a), while increasing channel height requires more volume of the pricey EGaIn and higher pressure to manipulate it, and also significantly affect the reconfiguration speed. Therefore the channel height is an

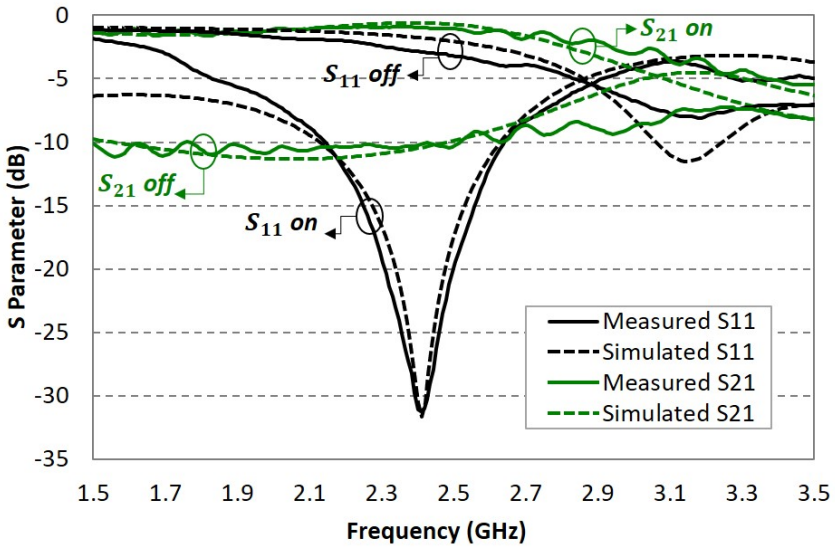

Figure 2.18: The two port S parameters S_{11} and S_{21} (black and green solid lines) are measured with liquid metal for channel height of $h = 0.3$ mm and compared with the simulation results (black and green dashed lines).

important parameter need to be optimized in the fluidic design.

To determine a minimum channel height providing satisfying electrical contacts, we built a simple transmission line switch as shown in Fig. 2.16 (b). The transmission line had a slot in the middle with a single lateral microfluidic channel mounted on top of the slot. The switch was turned on (off) by filling (withdrawing) EGaIn in the channel. The transmission line was designed to have a characteristic impedance of 50 Ω with a width of $w = 10$ mm on a 250 mil thick RT 5880 board. The gap on the transmission line has a width 0.8 mm. The channel width is selected as 1.8 mm, giving a 0.5 mm contact area on each side of the slot. The size of contact area is chosen to ensure the reliable connection between copper and the liquid metal plug. A smaller contact area could result in misalignment and unreliable contacts, while making the area too large could affect the sealing and isolation between adjacent channels. Using a wide transmission line helps improve the reliability of measurements for channel quality and liquid metal contacts. However, the S parameters are expected to be different from the broadband narrow transmission lines due to the relatively small size of the feeding pin comparing to the microstrip line.

Fluidics with 3 different channel heights $h = 0.1, 0.2$ and 0.3 mm were attached onto the transmission line and the two port S parameters S_{11} and S_{21} were measured with liquid metal, as shown in Fig. 2.17. According to the full-wave simulation, the two port S parameters are not very sensitive to the overall impedance of the liquid metal plug while changing the height of the channel. It is proved that the channel height of h =0.3 mm gives the best contact between the area of the gap and is therefore chosen for the microfluidics of the prototypes. Measurement results of the instant with 0.3 mm channel height are plotted in Fig. 2.18 and demonstrate good agreement with full-wave simulations. The maximum insertion loss measured in the frequency range of 2 to 2.5 GHz for the "on" state is 1.2 dB, while the maximum insertion loss simulated was 0.54 dB within the same frequency range.

After the EGaIn/mineral oil flow is withdrawn into the microfluidics, the motion of EGaIn plugs loading the two slots is synchronous, so that the lengths of slots are varied simultaneously. Besides manual control, the synchronous movements of the two liquid metal plugs can also be easily achieved using a two-channel syringe pump, since the cross section of channel is uniform and a given volume of liquid flow corresponds to the same amount of liquid metal movement at the two slots. With a electric-driven syringe pump, the lengths of liquid metal tuned slots can be very well controlled, with the maximum error within ± 1 mm. Since the frequency reconfiguration for this proposed antenna relies on tuning the slot length L_s, we should expect effect of the length difference on the accuracy of frequency selection. A quick simulation is performed to investigate the effect of slot length difference. We use the antenna topology with one pair of slots and $P_s = 24$ mm. One of the slot length has been fixed as 36 mm while length of the other slot is varied from 34 mm to 38 mm. The simulated S_{11} are plotted in Fig. 2.19. For a slot length difference of $\Delta L = \pm 1$ mm, the shift of selected frequency from 3.35 GHz is within ± 0.03 GHz (0.9%), and for $\Delta L = \pm 2$ mm, the shift of selected frequency is within ± 0.05 GHz (1.5%).

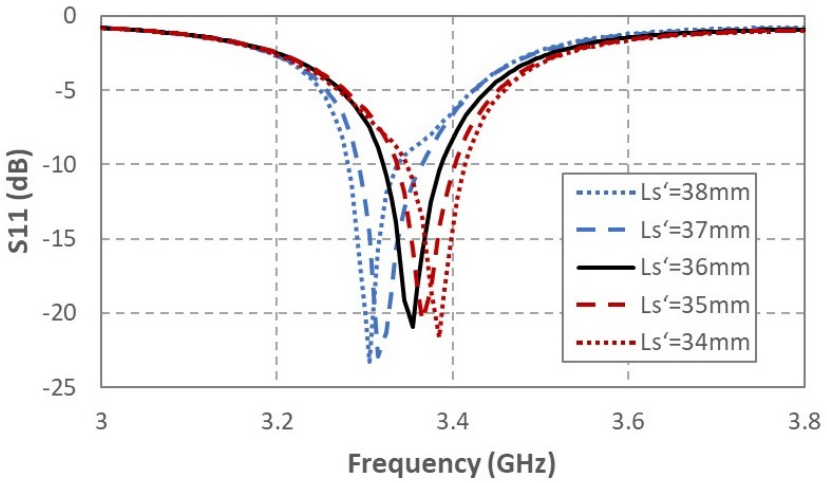

Figure 2.19: Simulation of the effect of slot length difference. One of the slot length is fixed as 36 mm, while the other slot length L_s' is varied and simulated S_{11} is plotted for each case. The dimension of the slot length L_s is illustrated in Fig. 2.7 (a).

2.4 Measurements and Discussions

The single-pair-slot prototype PASS with $P_s = 24$ mm is first fabricated for preliminary testing. The liquid metal plug has been pumped into the microfluidic channel on top of PCB substrate and tuned for different cases of L_s. In practice, the two frequency bands of the antenna can be tuned continuously and the number of achievable states is only limited by the accuracy of liquid control in the designed channel. Here we choose a few discrete states to demonstrate the tuning capability for the patch antenna with liquid metal tuning slots. 5 states with $L_s = 0$ mm, 8 mm, 16 mm, 24 mm and 32 mm have been achieved by pumping liquid metal plug accordingly and S_{11} for each case has been recorded and compared with the full-wave simulations to characterize the performance. As shown in Fig. 2.20, the measured S_{11} results for the 5 states are plotted for each state, which agree very well with the simulation results from full-wave simulator HFSS, proving the feasibility of this approach in developing frequency reconfigurable PASS antenna.

The prototype wide-band frequency reconfigurable PASS with 3 pairs of composite slots is than fabricated and measured with liquid metal integrated for slot tuning. S_{11} has been measured for 9 states by tuning the 2 pairs of slots A and C with varying slot length (referring

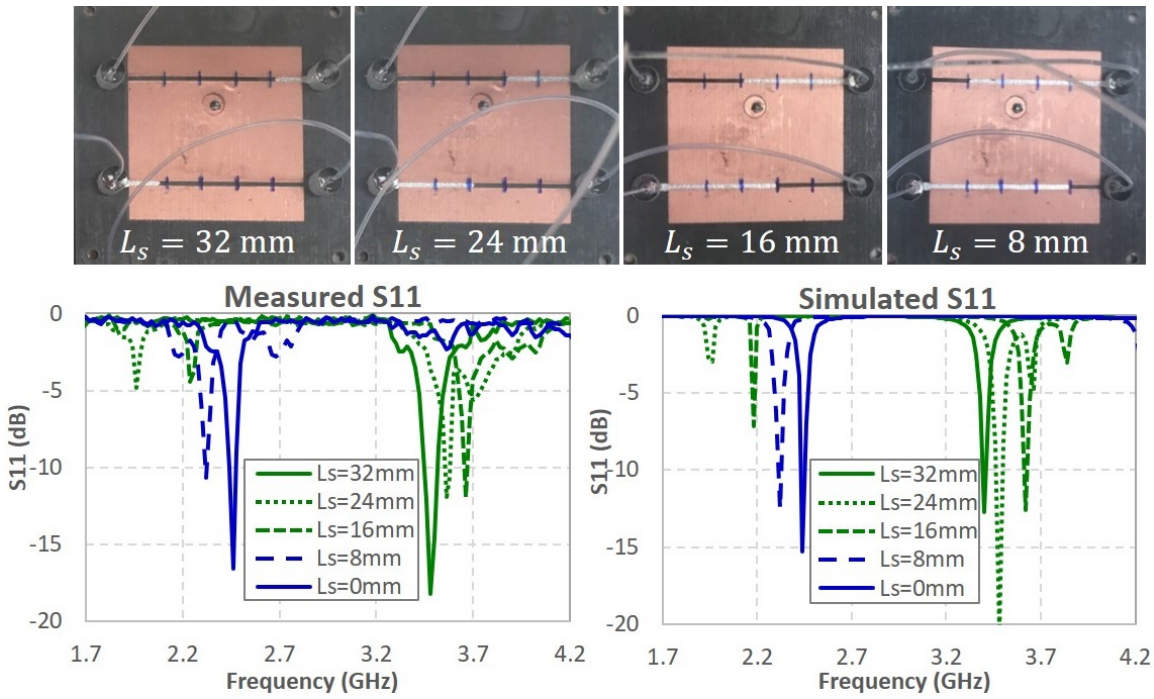

Figure 2.20: The single-pair-slot prototype PASS is first prototyped and measured with liquid metal slot tuning. The S_{11} for 5 discrete states with varied L_s are measured and compared with simulations.

to Fig. 2.10 (b)), which are denoted by the slot symbol (A or C) and the slot length (e.g. 40 mm). The measured S_{11} for each of the cases are plotted in Fig. 2.21 and compared with simulation results denoted by dashed lines. Varying the slot length of slot C to 0 mm, 8 mm and 16 mm excites the operating band centered at 2.35 GHz, 2.28 GHz and 2.12 GHz, while the length of 24 mm, 32 mm and 40 mm excites the band centered at 3.46 GHz, 3.41 GHz and 3.23 GHz. The operating frequencies of tuning slot A with 0 mm, 8 mm and 16 mm are similar to those of slot C with corresponding slot length, while slot A with 24 mm, 32 mm and 40 mm excites the frequencies of 2.67 GHz, 2.60 GHz and 2.56 GHz. Very good agreement between simulated and measured resonant frequencies are observed and return loss greater than 10 dB are obtained for all the measured states. The three continuous tuning band are achieve and more frequencies within the bands can be easily obtained by including more intermediate states. After the first cycle of measurements, the liquid metal plugs are retrieved to the starting position without any skin residues formed on channel walls. A

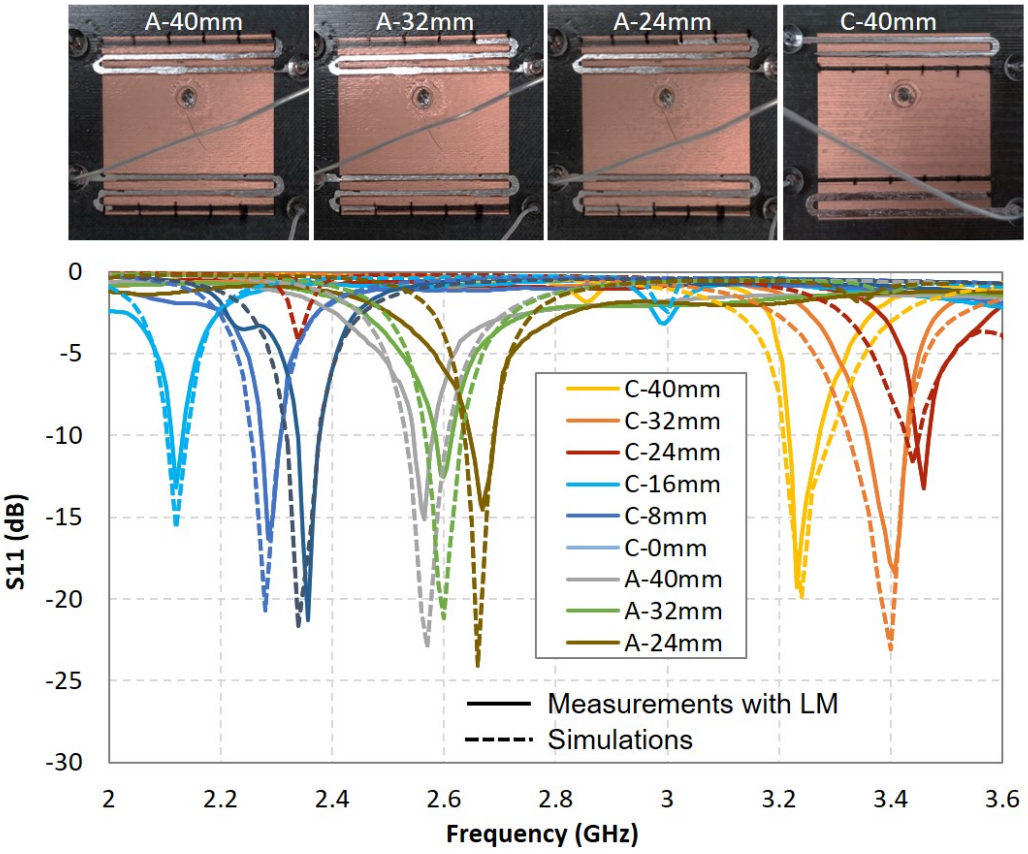

Figure 2.21: The prototype wide-band frequency reconfigurable PASS with 3 pairs of composite slots is measured for 9 states by tuning the 2 pairs of slots A and C with varying slot length. Each of the states has been denoted by the slot symbol (A or C) and the slot length (e.g. 40 mm).

second cycle of measurements are then successfully performed with very similar results to the first cycle.

The radiation pattern measurements are carried out in the spherical near-field chamber at University of California, Los Angeles (UCLA). The PASS prototype is mounted on a 3D printed bracket to secure the position of syringes and tubes, as shown in Fig. 2.22. The far-field radiation pattern in E plane and H plane for 6 discrete states are scanned for both horizontal and vertical polarizations at their corresponding center frequencies. Measurement results (solid lines) are compared with the full-wave simulations (dashed lines) in Fig. 2.23 for the 6 discrete states (L_s = 0 mm, 8 mm, 16 mm, 24 mm, 32 mm and 40 mm) achieved

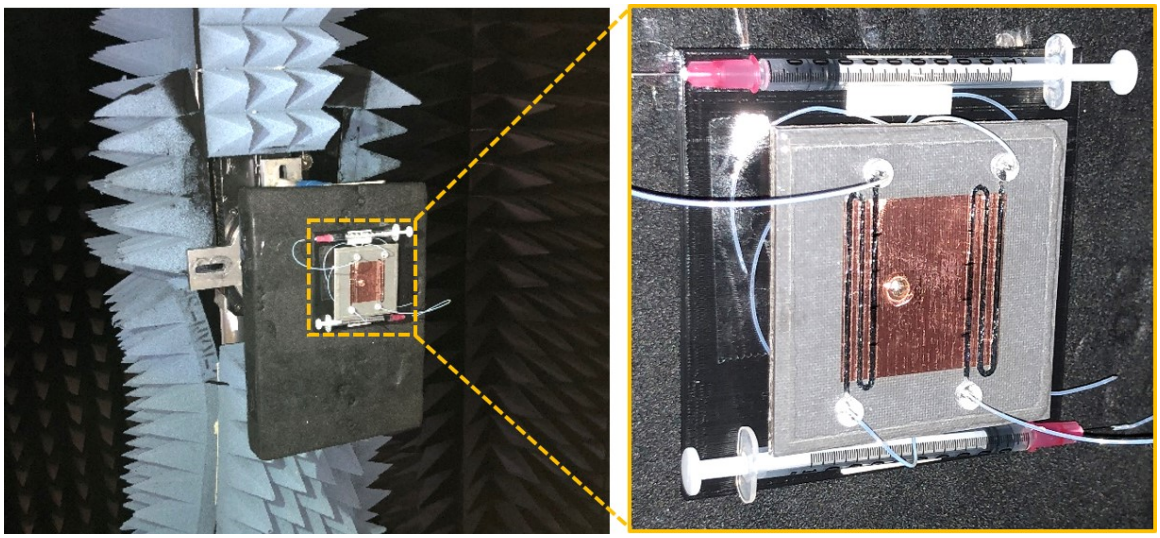

Figure 2.22: The radiation pattern measurements are performed in the UCLA spherical near-field chamber. The prototype wide-band frequency reconfigurable patch antenna is mounted on a 3D printed bracket in order to secure the position of syringes and tubes.

by tuning the C slots. As expected from simulations, the measurement results prove that radiation pattern is not significantly affected by slot tuning, with the cross-pol component remains in decent level for all the 6 measured states.

2.5 Summary

In this chapter, a wide-band and continuous frequency reconfigurable patch antenna based on 3D printed microfluidic channel and liquid metal has been demonstrated. The physical reconfiguration mechanism based on liquid metal tuning offers the ability to continuously change the properties of the antenna over a very wide frequency range. By integrating multiple pairs of liquid metal tuned composite slots on a rectangular patch antenna, a continuous wide frequency tuning bandwidth of around 70% is achieved with a narrow instantaneous bandwidth of 2% for each of the achieved states, without significant variations in the radiation pattern and efficiency. The mechanism of dual band operation for patch antenna with composite slots is discussed. Semi-empirical formulas for the dual-band resonant frequencies are established based on simulations and curve-fitting using PSO. The prototypes are fabri-

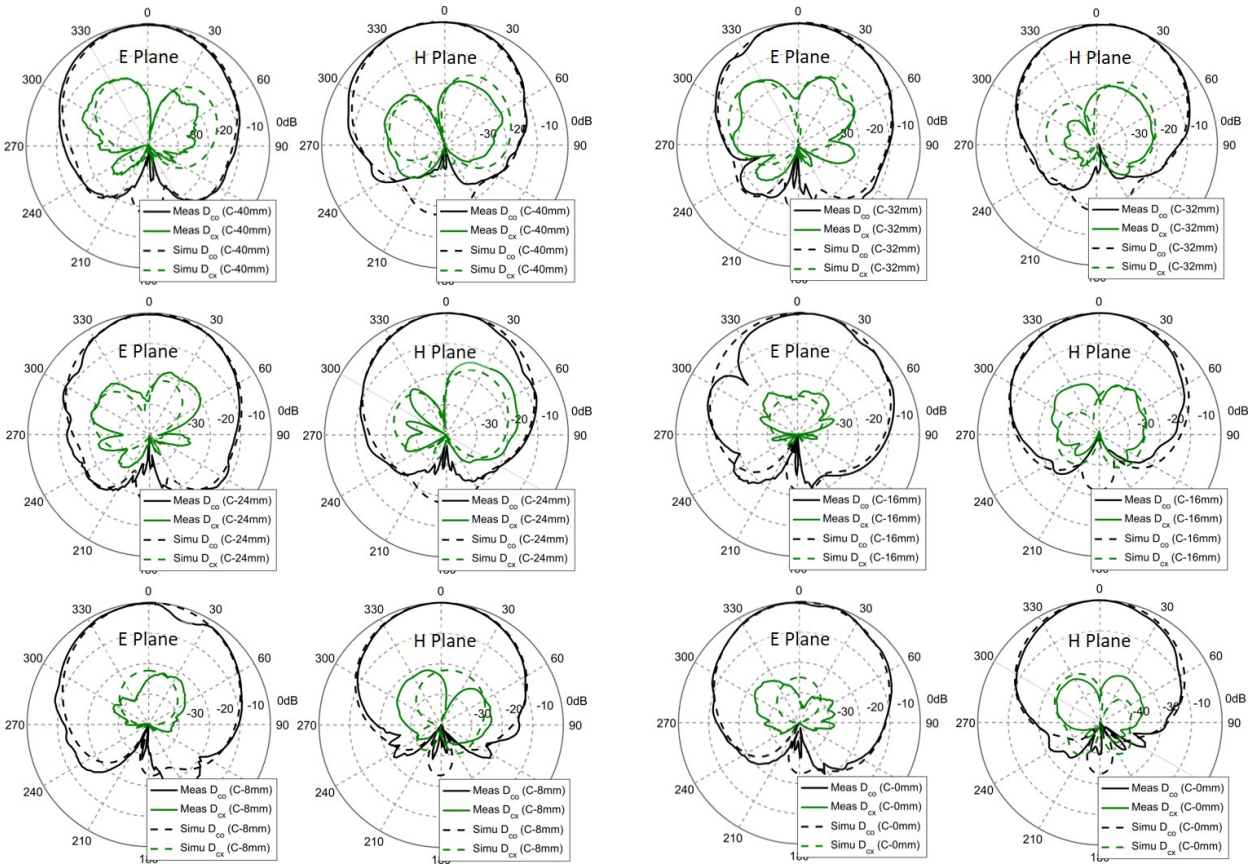

Figure 2.23: The far-field radiation pattern in E plane and H plane for 6 discrete states are scanned for both horizontal and vertical polarizations at their corresponding center frequencies. Measurement results (solid lines) are compared with the full-wave simulations (dashed lines) in Fig. 2.23 for the 6 discrete states with varied slot length L_s.

cated by attaching the 3D printed microfluidic module to the patch antenna on PCB with patterned adhesive layer. The proposed fabrication process is proved effective in constructing liquid metal antenna operating EGaIn with minimum skin residue. Liquid metal EGaIn carried by mineral oil has been used for prototyping and measurements. S_{11} and radiation pattern measurement results demonstrate good agreement with the full-wave simulations for prototypes with single and multiple pairs of slots. We believe that this design and prototype strategy can be applied to other potential topologies with various reconfigurable functionalities.

CHAPTER 3

Polarization Reconfigurable Extended E-Shaped Patch Antenna

In modern wireless systems that are designed to operate under complex and versatile environment, polarization is a critical factor in the determination of power level captured by receiving antennas. As a simple example, in a wireless communication system with randomly oriented devices carried by the users as illustrated in Fig. 3.1, polarization mismatch easily occurs if both transmitting and receiving antennas are single-polarized, resulting in reduced power efficiency. In the worst case scenario, the polarization states could be entirely mismatched if the transmit and receive antennas are linearly polarized (LP) with orthogonal orientations, or are circularly polarized (CP) with opposite sense of rotations. The development of multi-polarization reconfigurable antenna therefore holds great potential in mitigating the polarization mismatch in such wireless systems.

Reconfiguration of the radiation characteristics is conventionally achieved by incorporating tuning or switching elements, such as microelectromechanical systems (MEMS) switches [29], PIN diodes [30], varactor diodes [9], or combinations of those [31]. Based on these tuning technologies, some existing designs of polarization reconfigurable antennas demonstrated reconfigurations among a few LP states, or dual CP states, or even combination of both. In [39] 4 LP states $(0°, \pm 45°, 90°)$ were achieved with 8 PIN diodes. In [40] 24 PIN diodes were used to achieve 6 LP states covering two quadrants. In [41] dual CP and 3 LP states $(0°, 45°, 90°)$ were achieved using 6 PIN diodes with a crossed bow-tie dipole antenna. Since most of these designs are based on binarily operated devices, increasing the number of tuning states is challenging because of the increased number of tuning elements and complicated feeding and matching networks. Compared with conventional reconfiguration mechanisms,

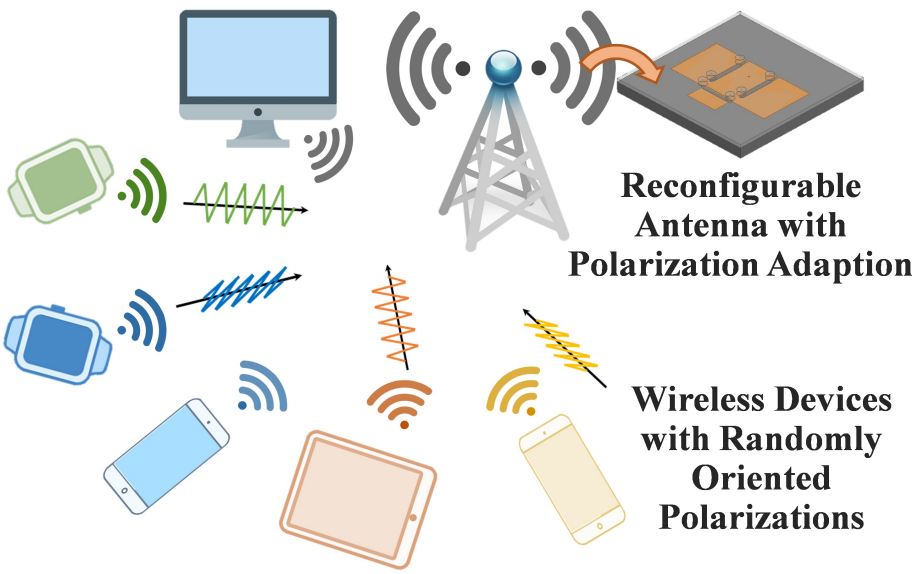

Figure 3.1: In a wireless communication system with randomly oriented devices carried by the users, polarization mismatch easily occurs if the receiving antenna is single-polarized, which results in reduced power efficiency.

liquid metal based reconfiguration has been demonstrated as a promising technique in terms of lower loss, more power handling, and greater tuning range [11, 42–45].

In this section, we propose a novel polarization reconfigurable antenna based on extended E-shaped patch antenna with 3D printed microfluidics and liquid metal tuning slots, with the antenna topology shown in Fig. 3.2. The proposed antenna is capable of multi-polarization reconfiguration among dual circular polarizations (RHCP and LHCP) and linear polarization with arbitrarily tunable orientation in the x-y plane, using a single feed. The reconfiguration is achieved by continuous physical movement of the liquid metal plugs inside the channel that covers the slots. A thorough and comprehensive circuit model analysis for asymmetric E-shaped patch is presented based on degenerate orthogonal modes. The design was prototyped and demonstrated with 3D printed microfluidics and eutectic gallium-indium (EGaIn) using optimized fabrication process flow based on [46, 47]. An additional sealing step is introduced to promote channel sealing and prevent channel degradation over long-term storage.

The paper is organized as follows: in Section II the polarization reconfigurable extended E-shaped patch antenna is introduced, which evolves from the LP and CP E-shaped patch

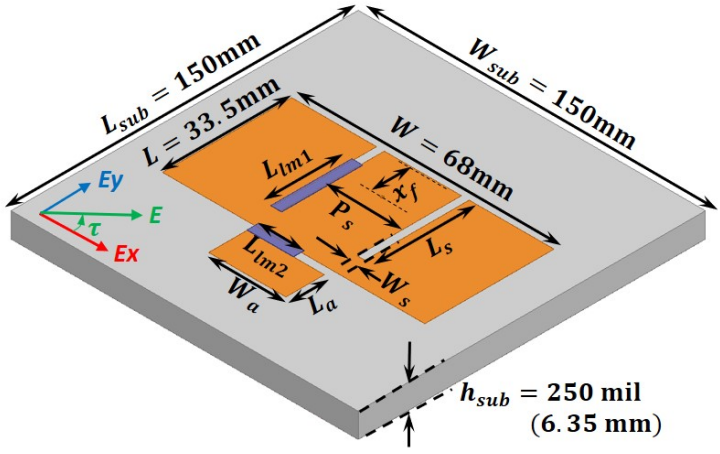

L	33.5 mm
W	68 mm
P_s	20 mm
L_s	1 mm
W_s	27 mm
L_a	10.5 mm
W_a	20 mm
x_f	10.4 mm

Figure 3.2: Antenna topology of the polarization reconfigurable extended E-shaped patch antenna with the dual CP and LP states with arbitrary orientation in x-y plane. The optimized parameters are listed.

antennas; in Section III, a circuit model analysis for asymmetric E-shaped patch is presented, proving the fundamental assumption in designing this multi-polarization reconfigurable patch; in Section IV, the design procedures aiming at impedance matching enhancement are discussed; in Section V, the process to prototype the proposed 3D printed microfluidics channeling liquid metal and its actuations are presented; and finally in the Section VI the measurement results demonstrate good agreement with the full-wave simulations.

The antenna topology evolves from the well-known linear-polarized and circular-polarized E-shaped patch antennas [48]. As shown in Fig. 3.3, the original LP E-shaped patch antenna

Table 3.1: Some representative polarization states and their corresponding slot length L_{lm1} and L_{lm2}.

L_{lm1} (mm)	L_{lm2} (mm)	L_{lm3} (mm)	Polarization State	L_{lm1} (mm)	L_{lm2} (mm)	L_{lm3} (mm)	Polarization State
21	2.5	0	$\tau = 10°$	0	2.5	21	$\tau = -10°$
21	6.5	0	$\tau = 30°$	0	6.5	21	$\tau = -30°$
21	20	0	$\tau = 45°$	0	20	21	$\tau = -45°$
11	20	0	$\tau = 60°$	0	20	11	$\tau = -60°$
0	20	0	$\tau = 90°$	0	20	0	$\tau = -90°$
21	*0*	*0*	LHCP	*0*	*0*	21	RHCP

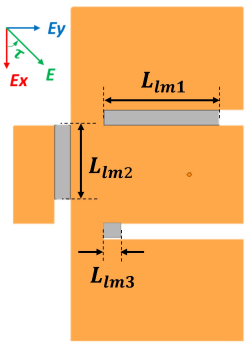

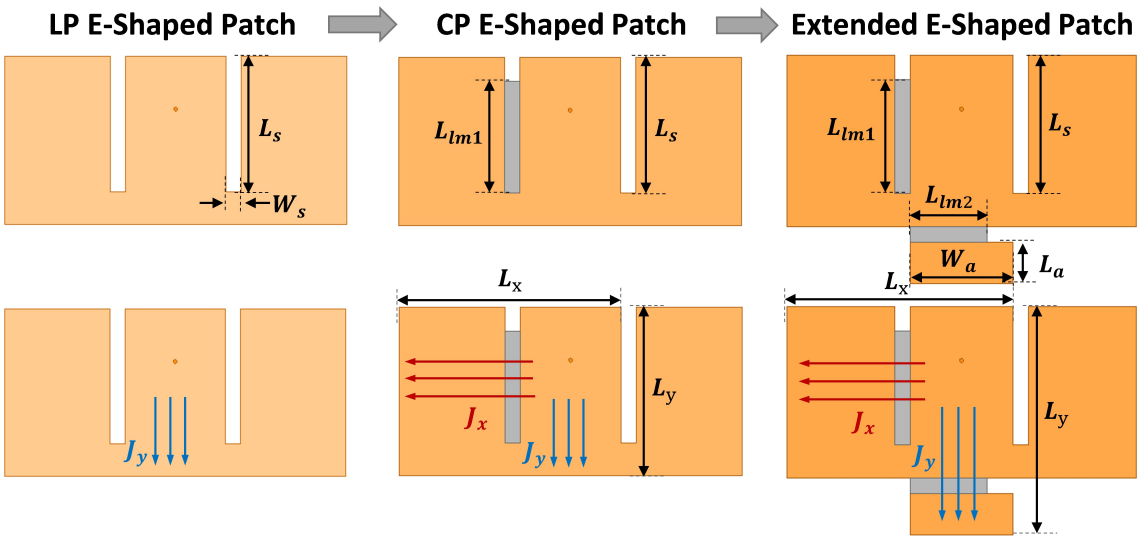

Figure 3.3: The antenna design evolves from the well-known linear-polarized and circular-polarized E-shaped patch antennas, with an extended element introduced to compensate the phase difference between the orthogonal field components imposed for CP state.

operating at 2.4 GHz consists of a rectangular patch with two symmetric parallel slots with the same length (L_s) and width (W_s). The LP E-shaped patch only excites the vertical mode of resonance with current J_y oriented vertically. The circular polarization can be achieved by making the two slots asymmetric, e.g. reducing the length of one slot by L_{lm1}. The dimensions are carefully selected so that both horizontal and vertical modes are excited. The horizontal current J_x is equal in magnitude to the vertical current J_y, with a 90° phase difference.

Based on the conventional CP E-shaped patch antenna, we propose a new topology by introducing an extended structure with dimension of $L_a \times W_a$, so that the horizontal and vertical lengths of resonance L_x and L_y are the same. The extended structure is connected to the original E-shaped patch with a partially filled slot of the length L_{lm2} as shown in Fig. 3.3. The extended patch compensates the phase difference between the two orthogonal modes and therefore, generates LP radiation. The orientation of the LP current is controlled by varying the ratio of the two current components J_x and J_y, by tuning the length of the two liquid metal plugs L_{lm1} and L_{lm2}. The original LHCP state can be achieved by fully

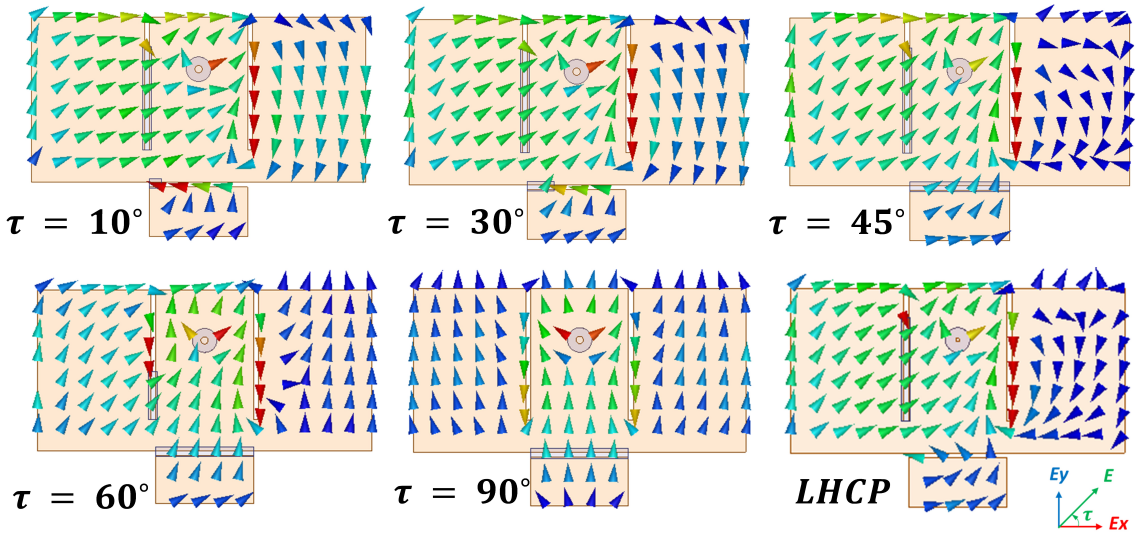

Figure 3.4: The vector current plots for the LHCP and LP states with $\tau = 10°, 30°, 45°, 60°$ and 90°, where τ denotes the polarization angle with respect to x axis. The results are based on full-wave simulation in HFSS.

disconnecting the extended structure with the main radiating element (with $L_{lm2} = 0$ mm).

Some representative polarization states and their corresponding slot lengths are listed in Table 3.1. Since the antenna topology exhibits mirroring symmetry over the y-z plane, the RHCP state and LP states in another quadrant ($\tau = 0°$ to $-90°$) can also be achieved by tuning the length of filling L_{lm3} for the second parallel slot, as illustrated in the inset figure in Table 3.1. Suppose the slot filling lengths L_{lm1}, L_{lm2} and L_{lm3} can be achieved with liquid metal injection and retraction, then by tuning the three liquid metal loaded slots, two CP states and LP states in any favorable orientations are realized. The vector current plots for some representative CP and LP states are shown in Fig. 3.4, with the rotation of polarization angle clearly observed.

The proposed multi-polarization reconfigurable patch antenna is based on the idea that current in an asymmetric E-shaped antenna could be decomposed into two orthogonal modes, whose magnitudes and relative phase difference could be manipulated by the asymmetric geometry design. In Section III, we presented a comprehensive circuit model analysis on asymmetric E-shaped patch antenna to further elaborate such observations and provide

design insights.

3.1 Circuit Model Analysis of Asymmetric E-Shaped Patch Antenna

This section deals with the circuit model aspects of designing asymmetric E-shaped patch antenna. We develop a circuit equivalence for the E-shaped patch antenna that is asymmetrically loaded and prove the effectiveness of considering two orthogonally polarized modes existing on the patch separately.

Standard microstrip patch antennas in general can be modeled as lossy resonant cavities enclosed by perfect magnetic walls on sides and perfect electric walls on the top and bottom. The field distribution in the cavity can be described in terms of eigen-modes, and the electric field can be expressed by the expansion of Helmholtz equation eigenfunctions. The impedance observed from the probe is equivalent to that of a network consisting of series of parallel RLC, with each mode of resonance related to the circuit parameter with the corresponding coefficient in the expansion [49]. Consider the fundamental mode (denoted as Mode 1) of a symmetric E-shaped patch antenna as shown in Fig. 3.5 (a). By introducing asymmetry into the patch element, Mode 1 degenerates from a single mode into two orthogonally polarized and overlapping modes, denoted as "Mode 1 Vertical (TM_v)" and "Mode 1 Horizontal (TM_h). Then the circuit equivalence of the asymmetric E-shaped patch consists of two series RLC tanks for TM_v and TM_h, together with a high frequency inductor which accounts for the effects of all the higher order modes. Notice that the current in the circuit equivalence is the common feed current for all the modes, and should be differentiated from the orthogonal radiating currents J_x and J_y for the two orthogonal polarizations as illustrated in Fig. 3.5 (b). The input impedance is therefore formulated as:

$$Z_{in}(\omega) = Z_v(\omega) + \xi(\omega) Z_h(\omega) + Z_\infty(\omega) \tag{3.1}$$

with the impedance of two orthogonal modes denoted as Z_v and Z_h, and the higher order

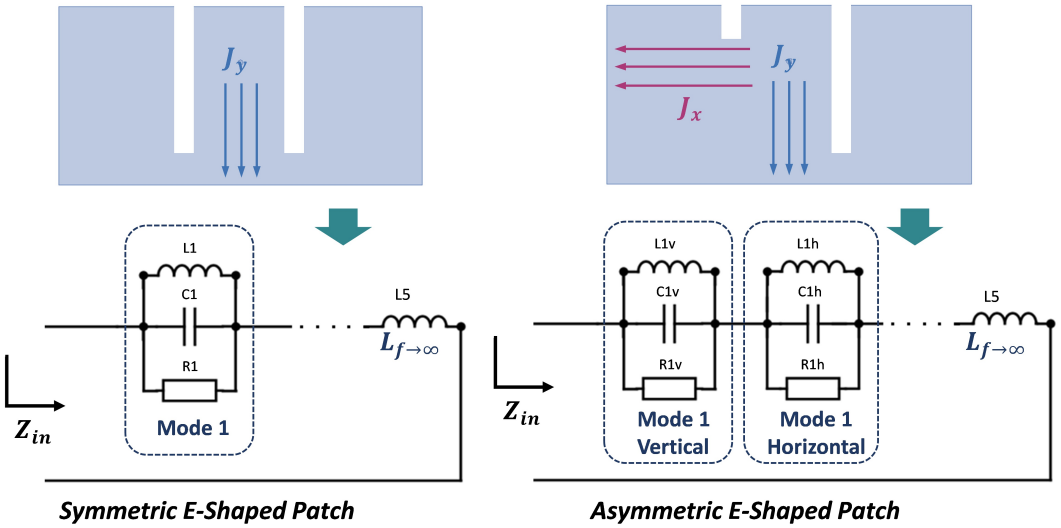

Figure 3.5: By introducing asymmetry into the patch element, a single initial mode degenerates into two orthogonally polarized and overlapping modes, denoted as "Mode 1 Vertical" and "Mode 1 Horizontal", that are connected in series. The vertical and horizontal modes can then be considered independently.

mode impedance as Z_∞, all as functions of the frequency ω. A phasing term ξ to imposed to account for the phase difference between two orthogonal modes. Z_v and Z_h can therefore be considered independently and then summed up with the imposed phase difference.

The vertical mode equivalent circuit is illustrated in Fig. 3.6. For the vertical degenerate resonance mode, the asymmetric E-shaped patch can be bisected into two half E-shaped patches, since the current only flows in vertical direction. For each of the half E-shaped patches, input impedances are two times of the corresponding symmetric full E-shaped patch, only with different slot lengths. The vertical mode impedance Z_v can therefore be found based on the impedance of two symmetric E-shaped patch Z_{1v} and Z_{2v} with slot length L_{s1} and L_{s2}, respectively:

$$Z_v(\omega) = (1/2Z_{1v}(\omega) + 1/2Z_{2v}(\omega))^{-1} \tag{3.2}$$

The impedance for symmetric E-shaped patch could be found according to the circuit equivalence illustrated in Fig. 3.6 (b) [48, 50]. The fundamental mode for a simple rectan-

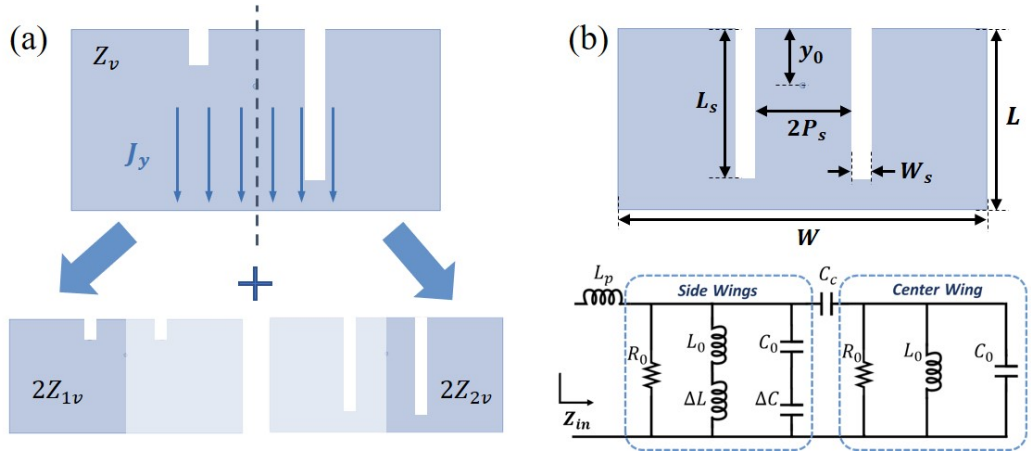

Figure 3.6: Equivalent circuit for the vertical mode of resonance. (a) The asymmetric slot length can be taken into account by bisecting the patch and considering two symmetric half E-shaped patches with different L_s. (b) For each of the symmetric patches, the circuit equivalence is constructed with parallel RLC resonators corresponding to center wing and side wings.

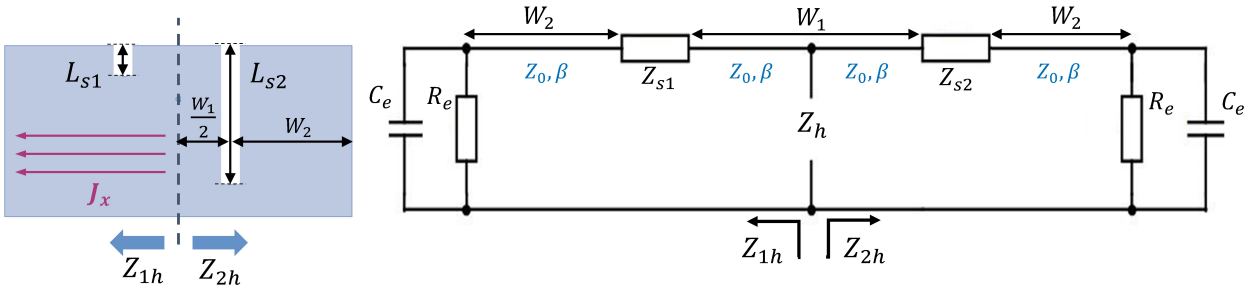

Figure 3.7: Equivalent circuit for the horizontal mode of resonance based on transmission line theory. The input impedance Z_h is found by considering the impedance looking from left (Z_{1h}) and right (Z_{2h}).

gular patch antenna can be modeled with the probe inductance L_p in series with a parallel RLC with circuit parameters R_0, L_0 and C_0. When two parallel and symmetric slots are incorporated into the patch, the current flows like a normal patch in the center wing, and therefore maintains the initial RLC circuit and the initial frequency of resonance. At the two side wings, additional series inductance ΔL and ΔC are incorporated to account for the effect of current flowing around the slots and the presence of notch capacitance. The two

resonators for center and side wings are coupled through a coupling capacitor C_c. Therefore, the vertical mode impedance for two different slot lengths Z_{1v} and Z_{2v} are related to the circuit parameters as [50]:

$$Z_{1,2v}(\omega) = j\omega L_p + [\frac{1}{Z_{center} + 1/j\omega C_c} + \frac{1}{Z_{side1,2}}]^{-1} \tag{3.3}$$

$$Z_{center}(\omega) = [\frac{1}{R_0} + \frac{1}{j\omega L_0} + j\omega C_0]^{-1} \tag{3.4}$$

$$Z_{side1,2}(\omega) = [\frac{1}{R_0} + \frac{1}{j\omega(L_0 + \Delta L_{1,2})} + j\omega(C_0 + \Delta C_{1,2})]^{-1} \tag{3.5}$$

Details for the analytical expressions of the vertical circuit parameters L_p, R_0, L_0, C_0, $\Delta L_{1,2}$, $\Delta C_{1,2}$ and C_c are provided in Appendix B.

For the horizontal degenerate mode, the asymmetric E-shaped patch can be analyzed from a transmission line perspective. This approach has been used to model the effect of transverse slit cut on rectangular patch antenna in [51]. As illustrated in Fig. 3.7, the patch is seen as two halves, each is a microstrip line of width L, and intercepted by a narrow slot of length L_{s1} and L_{s2}, at the distance $W_1/2$ away from the center, with slot impedance denoted as Z_{s1} and Z_{s2}, respectively. Parallel connected resistor R_e and capacitor C_e account for radiation and fringing fields of the patch edges, with a distance of W_2 away from the slots. The propagation constant β and characteristic impedance Z_0 are evaluated for microstrip line with width of L printed on 250 mil RT5880 substrate with $\epsilon_r = 2.2$. The loss tangent of substrate is < 0.001 at the frequency of 2.4 GHz. The effect of complex dielectric constant on the impedance calculation is very small. Therefore, the dielectric loss of substrate has been ignored in this calculation.

The horizontal mode impedance is therefore found by considering the input impedance looking from left (Z_{1h}) and right (Z_{2h}), seeing the transverse slots with lengths L_{s1} and L_{s2}, respectively:

$$Z_h(\omega) = (1/Z_{1h}(\omega) + 1/Z_{2h}(\omega))^{-1} \tag{3.6}$$

$$Z_{1,2h}(\omega) = Z_0 \frac{(Z'_e + Z_{s1,2}) + jZ_0 \tan(\beta W_1/2)}{Z_0 + j(Z'_e + Z_{s1,2}) \tan(\beta W_1/2)} \tag{3.7}$$

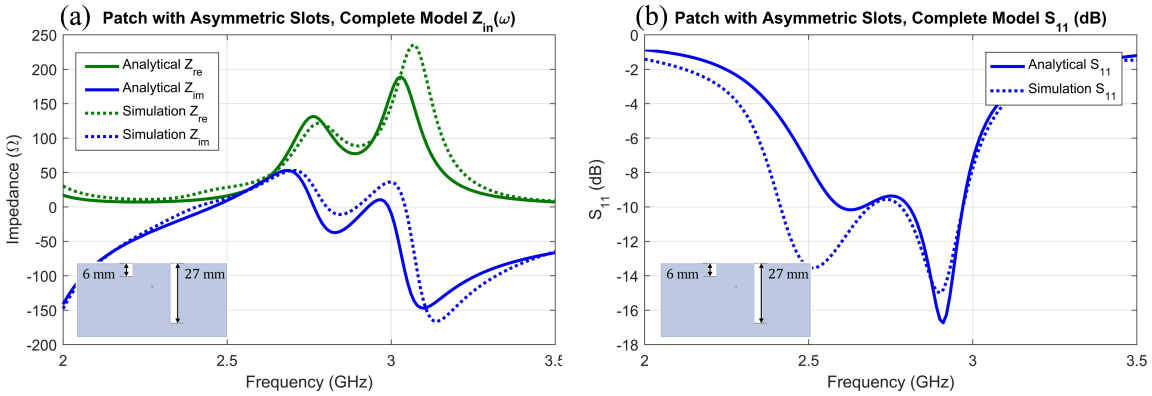

Figure 3.8: The input impedance and reflection coefficient calculated from the circuit equivalence with equations (3.1), (3.2) and (3.6) are compared with full-wave simulation for an asymmetric E-shaped patch with $L_{s1} = 6$mm, $L_{s2} = 27$ mm

$$Z'_e(\omega) = Z_0 \frac{(R_e + 1/j\omega C_e) + jZ_0 \tan(\beta W_2)}{Z_0 + j(R_e + 1/j\omega C_e)\tan(\beta W_2)} \tag{3.8}$$

Again the details for the analytical expressions of the circuit parameters Z_0, C_e, R_e and $Z_{s1,2}$ are provided in Appendix B.

As a representative case, the input impedance and reflection coefficient calculated from the circuit equivalence with equations (3.1), (3.2) and (3.6) are compared with full-wave simulation for an asymmetric E-shaped patch with $L_{s1} = 6$mm, $L_{s2} = 27$ mm, as shown in Fig. 3.8. The imposed phasing term in (3.1) is set as $\xi(\omega) = e^{j\pi/2}$, corresponding to 90° phase difference between vertical and horizontal modes, resulting in CP radiation. Plots for more cases with symmetric or asymmetric slots are also provided in Appendix. Good agreement between circuit equivalence and full-wave simulation is observed. It proves the effectiveness of the circuit equivalence for asymmetric E-shaped patch antenna by considering two orthogonal and overlapping modes. The two modes can be considered independently with their relative phase and magnitude manipulated based on designing the asymmetric geometry, which is the underlying strategy in designing the multi-polarization reconfigurable patch as presented in Section II.

3.2 Design Procedures for Improved Impedance Matching

Optimization of the geometric parameters for the extended E-shaped patch is a challenging task. As listed in Fig. 3.2, there are eight parameters need to be optimized, aiming at efficient polarization reconfiguration as well as good impedance matching for all the polarization states around the same frequency. The thickness of substrate has been dictated by the available options of RT5880 PCB board. Implementing optimization algorithms, e.g. Genetic Algorithm (GA) [52], particle swarm optimization (PSO) [36], is the typical approach to address high-dimensional complex design problems. In our case, however, running optimizations might not be efficient, since the fitness is defined with antenna performance in multiple tuning states. Suppose the S_{11} for one CP and three LP states are used to determine the fitness, then for each fitness calculation four full-wave simulations should be computed. The computational load is significantly increased comparing to typical antenna optimization problems. Therefore, in this section we provide design guidelines for the proposed polarization reconfigurable antenna. After following the procedures to achieve an initial design, fine tuning of the parameters via optimization algorithms can be conducted to further improve the performance. Chapter 7 in this thesis discusses two global optimization algorithms (particle swarm optimization and brain-storm optimization) and their hybridization. The interested readers are encouraged to review Chapter 7 for other relevant references on this topic.

The design procedures are illustrated in Fig. 3.9 and summarized as follows:

Step I. The first step is selecting a LP E-shaped patch topology for a specified substrate thickness and dielectric constant. The desirable choice of initial LP patch topology should with a relatively small slot width W_s and $L_x = (W + P_s)/2 > L$.

Step II. The selected LP patch topology is then modified with asymmetric slot length to achieve CP radiation with small axial ratio (< 0.5 dB), and further optimized under the geometric constraints of (a) $W_s < 2$ mm, for the ease of liquid metal tuning implementation, and (b) $(W+P_s)/2-L > (0.1 \sim 0.2)L$, giving space for adding the extended-element, aiming at a good impedance matching over the operating frequency band. Two types of impedance

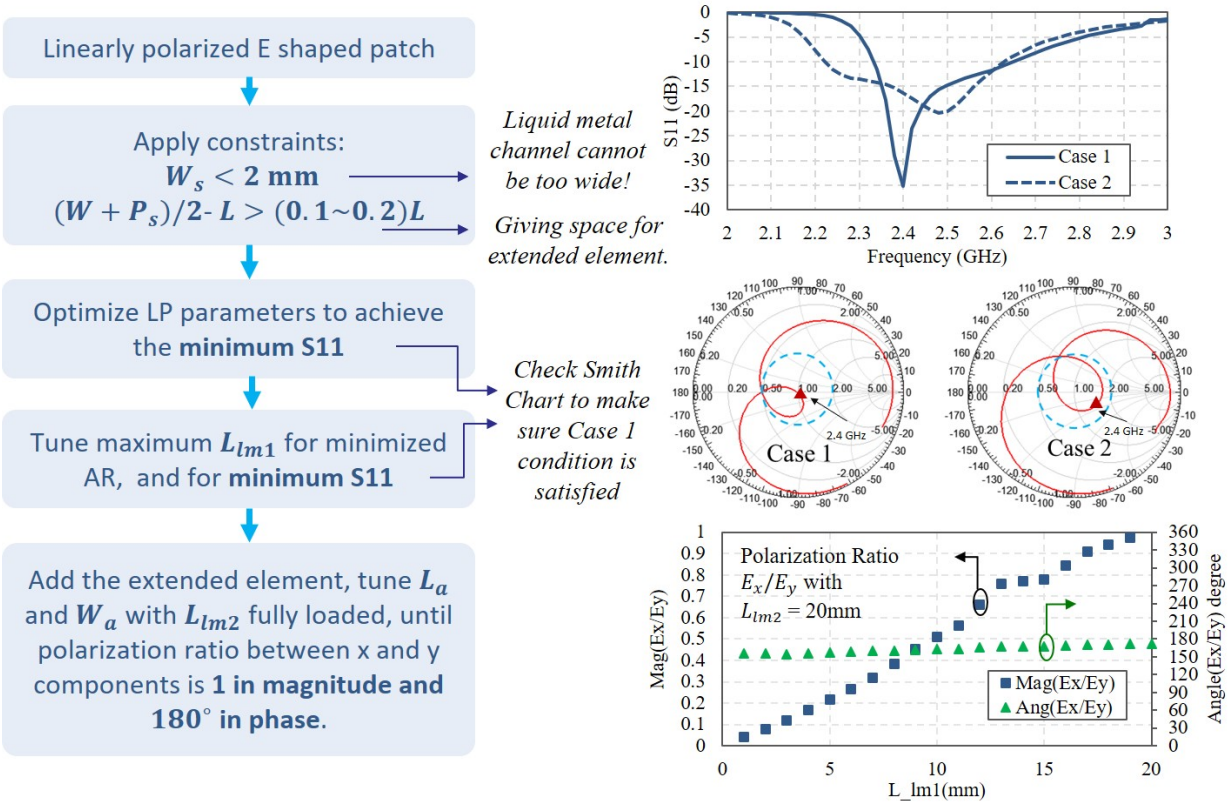

Figure 3.9: Design guidelines for the proposed polarization reconfigurable antenna. The first step is selecting a LP E-shaped patch topology as the starting point, and then optimize the selected LP patch with the design constraints and specific impedance matching goal. The extended element is then added with dimensions selected based on the LP state with $\tau = 45°$.

matching conditions are illustrated with Smith Charts in Fig. 3.9. Case 1 denotes the condition with very good impedance matching (-30 dB) in a relatively narrow band with the center frequency almost located at the center of Smith Chart, while the total -10 dB bandwidth has not been maximized (12.5% in this example). Case 2 achieves the maximum total bandwidth (19.5 %) with more locus enclosed by the VSWR = 2 circle than Case 1, but not necessarily passing through the center of Smith Chart. In most applications Case 2 is preferred since it offers decent S_{11} performance over a large bandwidth. For this design, however, we would prefer Case 1 with a deeper notch in S_{11} over Case 2 with a larger bandwidth, since the later incorporation of the multi-polarization states would

degrade the S_{11} level and shift the original center frequency in general. This is due to the modified vertical length of resonance L_y as the extended element is introduced and tuned via L_{lm2}. Optimization algorithms can be implemented to achieve the AR and S_{11} goals for the CP E-shaped patch antenna under the geometric constraints, since it remains a single-design problem up to this point, involving only one simulation per fitness calculation, and is therefore not very computationally consuming. The optimization of LP and CP E-shaped patch in Step I and II can be accelerated by linking optimization algorithms to the circuit model analysis presented in Section III, compared to solving full-wave simulations.

Empirically, the choice of Case 1 over Case 2 can be interpreted by considering the locus of the 2.4 GHz frequency point. Switching of the polarization states always introduces additional reactive loading due to switching and tuning of the slots, and as a result perturbs the impedance matching. Considering Case 1, where the 2.4 GHz point is located at the center of the Smith chart. As additional reactive loading is introduced, there is still a decent range of loading condition where the center frequency remains in the blue circle. Whereas in Case 2, where the 2.4 GHz point is intentionally detuned from the center in order to achieve maximum bandwidth, the 2.4 GHz point can hardly reach the center with any amount of series/shunt loading. The range of loading condition where the center frequency remains in the blue circle is also smaller than that in Case 1. Therefore, starting from Case 2, it would be more difficult to achieve decent impedance matching for all polarization states. The Smith chart plots for varying L_{lm1} and L_{lm2} are shown in Fig. 3.10. According to the Gamma contours, to the first order, it appears that increasing L_{lm1} results in additional series capacitive loading, while increasing L_{lm2} results in additional series inductive loading. The resulted variation of Gamma contour is significant with the required slot tuning. The selection of a reasonable initial point is therefore important in achieving decent impedance matching for all the polarization states.

Step III. Once a CP E-shaped design satisfying the requirements is achieved, an extended element is added to the bottom of the E topology with length L_a and width W_a. These two dimensions are adjusted with the bottom slot fully loaded (e.g. $L_{lm2} = W_a$), until the polarization ratio E_x/E_y is 1 in magnitude and 180° in phase (or 0°, depending on the

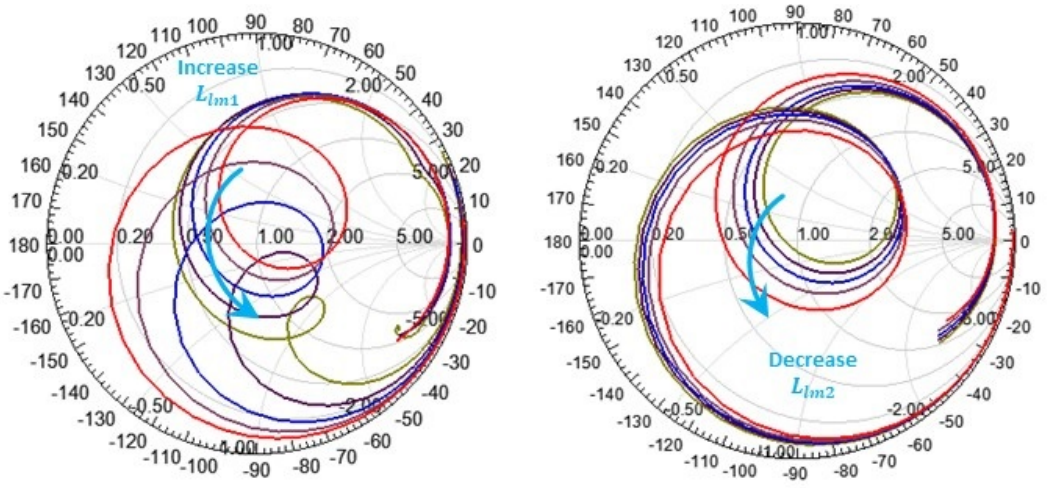

Figure 3.10: Smith chart plots with varying slot length L_{lm1} and L_{lm2}. Increasing L_{lm1} results in additional series capacitive loading, while increasing L_{lm2} results in additional series inductive loading. The dimensions corresponding to L_{lm1} and L_{lm2} are illustrated in Fig. 3.3.

orientation of coordinate system). The LP polarization reconfiguration states are almost always imposed with careful selection of L_a and W_a. When the slots L_{lm1} and L_{lm2} are fully loaded, the condition of $(W + P_s)/2 \approx L + L_a$ indicates similar resonance length L_x and L_y for horizontal and vertical current components, giving in-phase radiation for the orthogonal modes. Further tuning of the maximum vertical component with W_a should easily achieve $|E_x/E_y| = 1$, which results in a LP state with $\tau = 45°$. The design is then fixed once L_a and W_a are properly selected.

Using a thick substrate for bandwidth enhancement is a well-recognized approach for patch antenna designs. Here a 250 mil RT5880 substrate is used to improve the bandwidth, giving more freedom to trade-off polarization reconfiguration capability. Another design approach is to modify the size of the feeding pin r_{pin} for impedance matching improvement without sacrificing the polarization reconfiguration [53]. Fig. 3.11 compares S_{11} of the CP state (without loading L_{lm2}) for different pin sizes from 0.3 to 0.6 mm. It is clearly observed that reducing the pin size helps to improve the impedance matching, by providing an increased probe inductance. In Fig. 3.11 (c) and (d), the S_{11} for a few discrete states

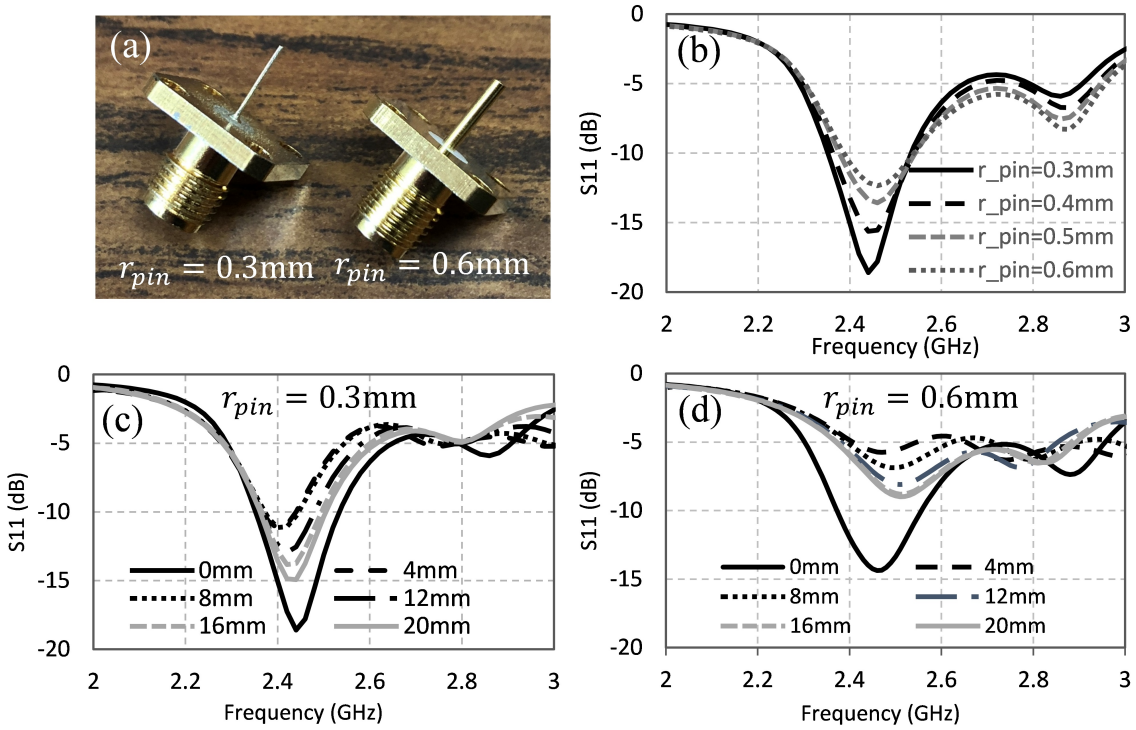

Figure 3.11: Reducing the pin size helps to improve the impedance matching. In (a) SMA connectors with different pin size r_{pin} = 0.3 mm and r_{pin} = 0.6 mm are shown, in (b) the simulated S_{11} of the CP state (without loading L_{lm2}) for different pin sizes from 0.3 to 0.6 mm.In (c) and (d), S_{11} with varying L_{lm2} are plotted for $r_{pin} = 0.3$ mm and $r_{pin} = 0.6$ mm, clearly demonstrates the improvement.

with varying L_{lm2} are plotted for r_{pin} = 0.3 mm and r_{pin} = 0.6 mm, respectively, clearly demonstrated the improvement of impedance matching performance with reduced pin size.

3.3 Prototyping and Liquid Metal Tuning Implementation

The prototypes of reconfigurable patch antenna with liquid metal tuning slots are fabricated using an improved process based on our previous works [46, 47], by employing an additional sealing step with thermal epoxy. As illustrated in Fig. 3.12, the microfluidic module made of optically clear acrylic material (VeroClear [37], Stratasys, USA) is 3D printed and attached to patterned PCB using double sided adhesive film. The microfluidic module design is directly

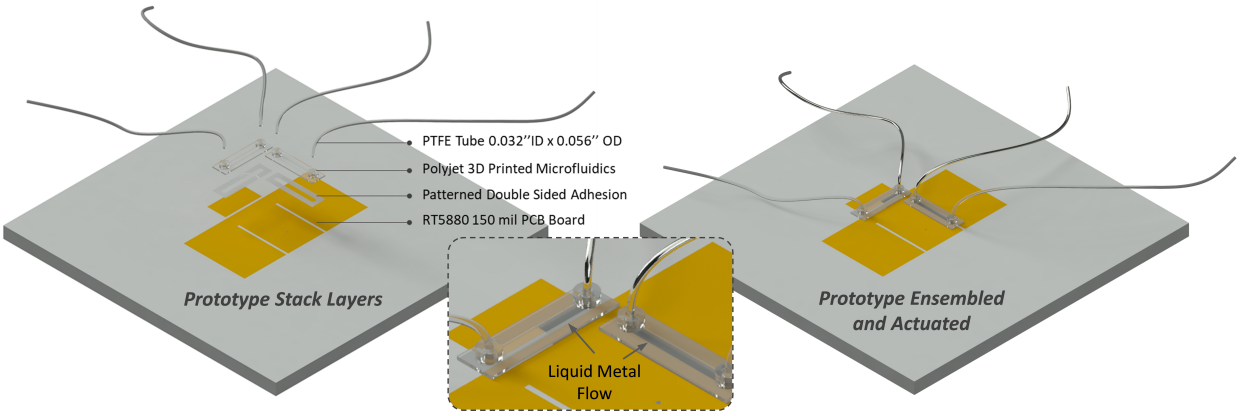

Figure 3.12: The multilayer prototype assembly. The prototyped liquid metal reconfigurable extended E-shaped patch antenna is assembled by attaching a Polyjet 3D printed microfluidics to the patch antenna on 250 mil RT5880 PCB substrate via a patterned double-sided adhesive layer. PTFE tubes are then inserted and sealed with UV and thermal epoxy.

exported from HFSS and printed by a 3D printing service (Fictiv, USA). The Polyjet 3D printer (Eden 260V, Stratasys, USA) is selected over Fused Deposition Modeling (FDM) for its high resolution (0.016 mm as claimed by the manufacturer) and smooth channel surface. Individual microfluidic modules are used for each slot to minimize the printing part volume as well as the fabrication cost. Microfluidic modules are designed with integrated inlet/outlet stubs and 0.3 mm channel height as optimized in [47]. A thinner channel reduces the required EGaIn volume, but becomes more prone to unreliable electrical contact due to incomplete filling of EGaIn at channel edges. Increasing channel height requires more EGaIn and actuation pressure to effectively manipulate liquid segment, leading to higher manufacturing cost and slower reconfiguration speed. The channel width is designed to be 2 mm over the 1 mm slot, leaving 0.5 mm-wide contact region between liquid metal and periphery copper on each side of the channel.

The extended E-shaped patch antenna was made on a 250 mil RT5880 substrate (Rogers, USA). The 3D printed modules were then bonded to the PCB with optically clear double-sided adhesive film (8146-2, 3M, USA). Mechanical compression was applied at room temperature overnight to achieve better adhesion. During the compression, we compensated

the height of inlet/outlet with a ABS 3D printed module so that the compression force was uniformly applied over the entire module. Poly-tetrafluoroethylene (PTFE) tubes (0.032" ID × 0.056" OD) were then assembled and sealed with Ultraviolet (UV) cured epoxy.

An additional sealing step was introduced compared with the previous process flow reported in [47] to promote channel sealing and prevent channel degradation over long term storage. We applied a transparent thermal epoxy (Scotch-Weld DP270 Clear) over the microfluidics modules and baked the module above an IR heater set at $85°C$ for three hours. The fully cured thermal epoxy well encapsulates the channel and provides compressive stress that improves the adhesion between PCB and channel, and therefore significantly enhances channel sealing and isolates liquid metal from air. With the final sealing step, we found the PTFE channel coating implemented in previous designs could be skipped but still maintain satisfactory minimal residue, without any blockage of liquid metal control. Fabricated prototypes preserved satisfactory quality through out multiple measurements with liquid metal flows back and forth in the channel, which helps achieve the good agreement between simulation and measurement results as shown in the later section.

Full-wave simulations in HFSS are conducted to study the effects of the presence of 3D printed microfluidic channel and thermal epoxy layer. The Veroclear used in 3D printing module has a reported dielectric constant of $\epsilon_r = 3.1$ and a loss tangent of $\tan\delta = 0.02$ [37]. The thermal epoxy has a dielectric constant of $\epsilon_r = 3.5$ and a loss tangent of $\tan\delta = 0.02$ [54]. In Fig. 3.13 the simulated S_{11} with and without the 3D printed microfluidics and sealing epoxy layer for different L_{lm1} and L_{lm2} are plotted and compared. Presence of the fluidic channel on top of the E-shaped patch antenna results in a slight lower frequency shift by 10 to 20 MHz, since the thickness of the channel is relatively small comparing to the wavelength ($< 0.005\lambda$ at the frequency of 2.4 GHz).

The simulated broadside gain and radiation efficiency for different polarization states are listed in Table. 3.2. The radiation efficiencies listed in Table. 3.2 as "LM" account for the conductive loss of EGaIn. While the cases listed as "LM & Fluidics" account for both conductive loss of liquid metal and dielectric loss of 3D printed microfluidics, epoxy layer and carrier liquid. Since the conductivity of EGaIn is relatively high (3.4×10^6 S/m),

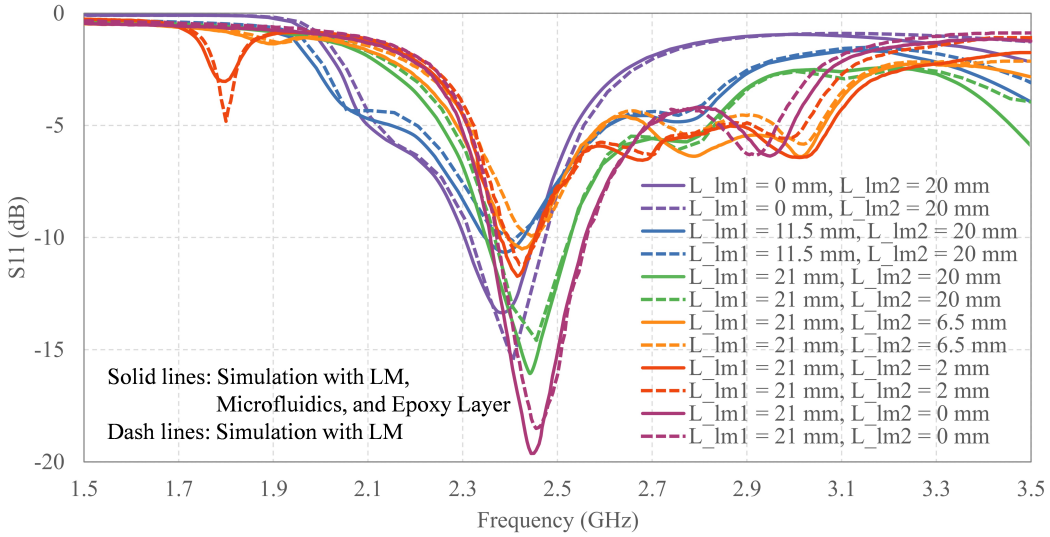

Figure 3.13: The simulated S_{11} with (solid lines) and without (dashed lines) the 3D printed channel and epoxy layer for 6 representative polarization states.

the degradation in radiation efficiency due to the loss of liquid metal is not significant. Simulations with complete model maintain a 90% efficiency for each of the polarization states. The simulated antenna broadside gain and radiation efficiency at the frequency of 2.4 GHz have not changed significantly with the slot length tuned by liquid metal, with a broadside gain maintains as 7-8 dB. The efficiency and realized gain measurements for this proposed antenna are not conducted due to the limitations on measurement capability. Some existing works with efficiency and gain measurements for liquid metal based antennas could serve as good references. In [55] a liquid metal monopole antenna was built and the realized efficiency from 80% to 85% was reported, across the operating frequency range. There was around 6% degradations comparing the measurements to simulations, which could be due to the imperfect liquid metal contact and inaccuracy in dielectric constant. Therefore, we expect the realized gain for our cases should exhibit a similar amount of deviation to the simulation. In general, we would expect a realized efficiency greater than 84% for all the polarization states listed here.

Liquid metal EGaIn carried by mineral oil was used to load the slots while measurements are conducted. The liquid metal plugs formed direct physical and electrical contact with the periphery copper elements, tuning the physical length of the exposed slots L_{lm1} and L_{lm2}.

Table 3.2: The simulated radiation efficiency and peak gain for different cases of slot length L_{lm1} and L_{lm2}, with and without microfluidic channel.

L_{lm1} (mm)	L_{lm2} (mm)	L_{lm3} (mm)	Polarization State	Peak Directivity	Efficiency (LM)	Peak Gain (LM)	Efficiency (LM & Fluidics)	Peak Gain (LM & Fluidics)
21	2.5	0	$\tau = 10°$	7.71 dB	98.6%	7.65 dB	90.7%	7.27 dB
21	6.5	0	$\tau = 30°$	7.84 dB	98.3%	7.76 dB	89.0%	7.33 dB
21	20	0	$\tau = 45°$	8.10 dB	99.0%	8.05 dB	90.3%	7.65 dB
11	20	0	$\tau = 60°$	8.46 dB	99.1%	8.42 dB	91.6%	8.08 dB
0	20	0	$\tau = 90°$	8.31 dB	98.5%	8.24 dB	91.0%	7.90 dB
21	*0*	*0*	LHCP	8.31 dB	99.8%	8.29 dB	92.3%	7.96 dB

The use of carrier liquid encapsulates the EGaIn plug and prevents the formation of skin residue due to oxidation. Mineral oil is selected as the carrier liquid with its low dielectric loss at radio frequency ($\tan\delta < 0.01$ [38]). The liquid metal loading and actuating procedures to minimize the formation of skin residues has been elaborated in [47]. For this prototype, the PTFE tubings are connected to 30 mL syringes are manually actuated. Typical time required to transit between two adjacent states is within 1 second, while for two distant states (e.g. LHCP and LP $\tau = 90°$) the transit time is 5 to 10 seconds, depending on the applied pneumatic pressure. Reduction of the transition time are expected with future developments in advanced microfluidic systems.

3.4 Measurements and Discussions

Two types of prototypes are fabricated and tested to validate the proposed design. The "ideal tuning" case denotes the prototype using cut copper foil tape (with copper thickness of 0.03 mm) to directly bridge the gap of slots at the positions corresponding to the slot length for various polarization states, and then properly soldered with the edges of the slots to ensure reliable contact, as shown in Fig. 3.14 (a). It represents the most ideal situation without material or contact loss introduced by the tuning elements, and is used to represent the first-pass proof of concept for the antenna design. The "liquid metal (LM) tuning" case denotes and prototype assembled with microfluidics, tubing and syringes, and actuated with EGaIn tuning according to the procedures presented in Section V, as illustrated in Fig. 3.14

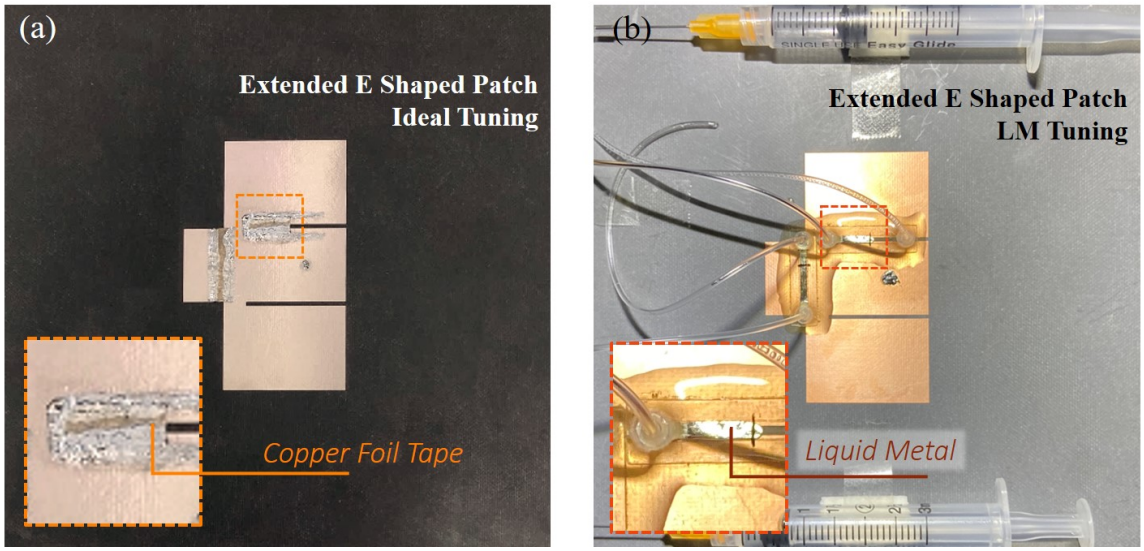

Figure 3.14: Prototypes fabricated and measured for the multi-polarization reconfigurable extended E-shaped patch. (a) The "ideal tuning" case denotes the prototype with copper foil tape directly bridging the gap of slots. (b) The "LM tuning" case denotes prototype assembled with microfluidics, tubing and syringes and actuated with liquid metal tuning.

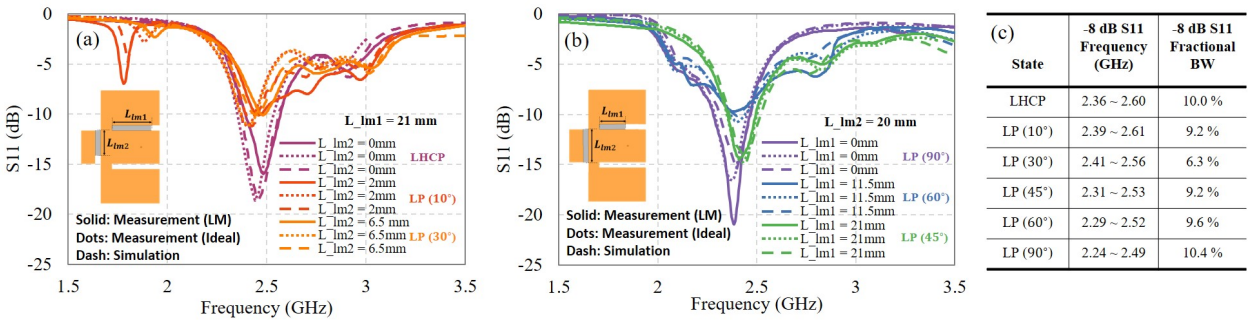

(c)

State	-8 dB S11 Frequency (GHz)	-8 dB S11 Fractional BW
LHCP	2.36 ~ 2.60	10.0 %
LP (10°)	2.39 ~ 2.61	9.2 %
LP (30°)	2.41 ~ 2.56	6.3 %
LP (45°)	2.31 ~ 2.53	9.2 %
LP (60°)	2.29 ~ 2.52	9.6 %
LP (90°)	2.24 ~ 2.49	10.4 %

Figure 3.15: The measured S_{11} with ideal tuning (dots lines) and LM tuning (solid lines) prototypes comparing with full-wave simulations (dash lines), for 1 LHCP state and 5 LP states with $\tau = 10°, 30°, 45°, 60°$ and 90°. (a) $L_{lm1} = 21$ mm is fixed and fully loaded with liquid metal, and L_{lm2} is tuned to 0 mm, 2 mm, and 6.5 mm; (b) $L_{lm2} = 20$ mm is fixed and fully loaded, while L_{lm2} is tuned to 0 mm, 11.5 mm, and 21 mm; (c) The measured -8 dB impedance matching bandwidth for the CP and LP states with LM tuning.

(b).

In practice, the length of the slots can be tuned continuously with liquid metal, with

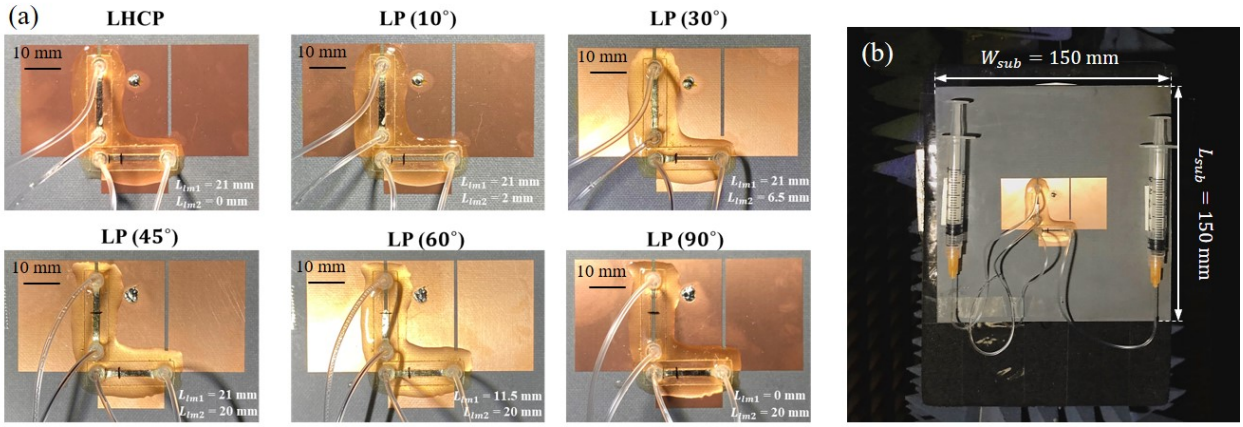

Figure 3.16: (a) Pictures for the 6 measured polarization states with LM tuning. The variation of liquid metal loading inside microfluidics can be clearly observed. (b) The prototype polarization reconfigurable patch antenna is mounted in the UCLA spherical near-field anechoic chamber with a 3D printed bracket in order to secure the position of syringes and tubes.

the LP polarization angle scanning within two quadrants in the x-y plane. The number of achievable LP polarization states is only limited by the accuracy of pneumatic liquid control in the designed channel, which largely depends on the used of actuation method. Here only 6 discrete states are measured for the prototypes with ideal tuning and LM tuning, including one LHCP state and five LP states with $\tau = 10°, 30°, 45°, 60°$ and $90°$, which are consistent with the simulation cases presented in Section II, with their corresponding slot lengths listed in Table 3.1.

Fig. 3.15 (a) and (b) shows the measured S_{11} for the 6 states with ideal tuning (dots lines) and LM tuning (solid lines) prototypes comparing with full-wave simulations (dash lines). In Fig. 3.15 (a), $L_{lm1} = 21$ mm is fixed and fully loaded with liquid metal, and L_{lm2} is tuned to 0 mm, 2 mm, and 6.5 mm, achieving 1 LHCP and 2 LP states with $\tau = 10°$ and $30°$. In 3.15 (b), $L_{lm2} = 20$ mm is fixed and fully loaded, while L_{lm1} is tuned to 0 mm, 11.5 mm, and 21 mm, achieving 3 LP states with $\tau = 45°$, $\tau = 60°$ and $90°$. The simulated and measured reflection coefficient shows that the design satisfies the criteria of -10 dB at 2.4 GHz for all the states. The comparison between the simulated and measured data shows very good

agreement, for both ideal tuning and LM tuning cases. Fig. 3.15 (c) tabulates the realized -8 dB impedance matching bandwidth for the CP and LP states measured with LM tuning. The achieved fractional bandwidth ranges from maximum of 10.4% (for 90° LP state) to minimum of 6.3% (for 30° LP state). It is shown that although the impedance matching performance varies among different polarization states, the achieved operating bandwidth remains decent for all the measured polarization states. For each of the polarization states, a picture is shown in Fig. 3.16 (a), in which the variation of liquid metal loading is clearly observed.

Possible approaches to further improve bandwidth performance for the extended E-shaped patch are similar to those for other patch antenna topologies, including the use of thicker substrate (larger h_{sub}) and smaller dielectric constant (smaller ϵ_{sub}), aiming at reducing the quality factor of the resonance cavity formed by the patch antenna. Other potential extrinsic techniques for bandwidth enhancement employ parasitic coupling elements [56, 57], electromagnetic band gap structures [58, 59], or multilayer stacked topologies [60]. The E-shaped patch antenna, from which our extended E-shaped patch is evolved, is one of the popular designs with effective bandwidth enhancement (typically with bandwidth 20% to 30%). Fig. 3.17 shows the bandwidth trends of a direct fed single layer rectangular patch antenna relative to substrate permittivity and thickness [61]. Referring to our cases with $\epsilon_{sub} = 2.2$ and $h_{sub} = 250\text{mil} \approx 0.05\ \lambda_0$, the intrinsic achievable bandwidth for a simple rectangular patch is around 7.5%, which is close to what we have achieved in this design. Therefore, we believe that the achievable bandwidth performance for the extended E-shaped patch is similar to what expected for simple rectangular patch antennas.

The radiation pattern measurements are carried out in the spherical near-field chamber at University of California, Los Angeles (UCLA). The prototype polarization reconfigurable patch antennas are mounted on a 3D printed bracket to secure the position of syringes and tubes, as shown in Fig. 2.22 (b) for the LM tuning case. A relatively large ground plane of 150 mm × 150 mm (over 2 times the effective wavelength) is used here to block the effects of backside positioning equipments during the radiation pattern measurements. The 3D printed bracket behind the antenna-under-test is also blocked by the large ground plane

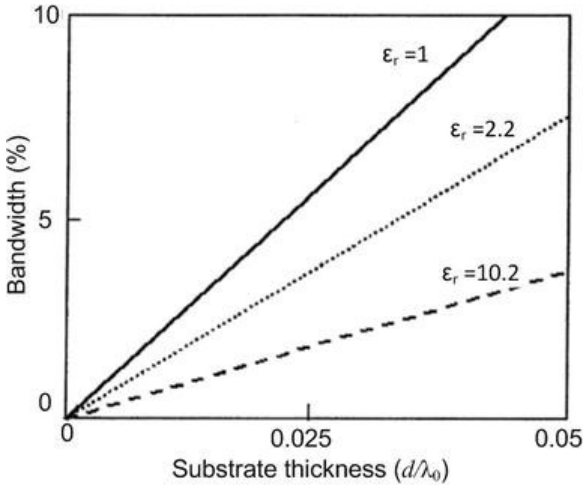

Figure 3.17: Bandwidth trends of a direct fed single layer rectangular patch antenna relative to varying substrate permittivity and thickness [61].

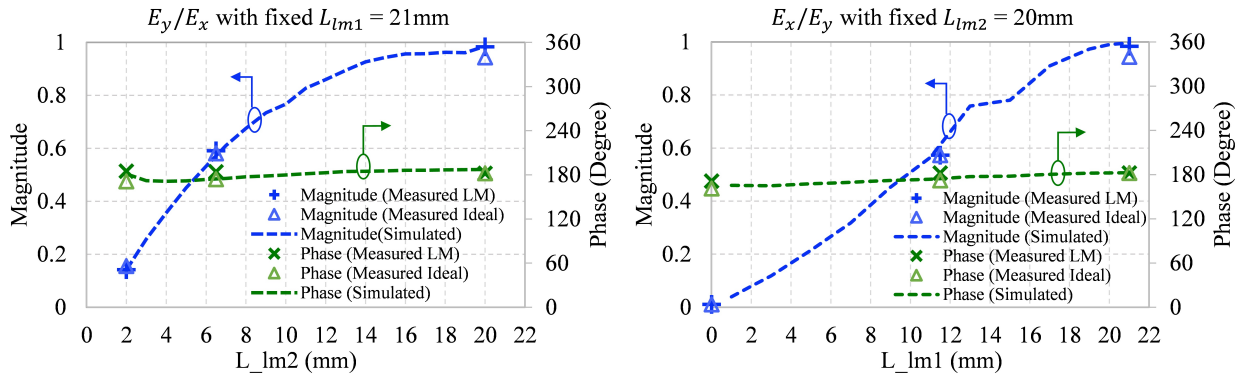

Figure 3.18: The simulated and measured far-field polarization ratio between horizontal and vertical components for (a) LP states with polarization angle τ from 45° to 90° and (b) with τ from 0° to 45°, indicating the rotation of polarization angle.

and is therefore not appeared in Fig. 2.22 (b), and also is not included in the full-wave simulations since its effect is expected to be very small. The radiation characteristics for the six polarization states are scanned for both horizontal and vertical polarizations at the frequency of 2.4 GHz. For ideal tuning cases, complete near-field scans are performed for all the states, while for LM tuning cases, far-field scans are performed at two representative far-field cuts corresponding to E and H planes for each of the states.

The far-field polarization ratio between horizontal and vertical components measured in

far-field is plotted in Fig. 3.18 in both magnitude and phase, for the 5 LP states achieved via ideal and LM tuning. In Fig. 3.18 (a) and (b), the magnitude of E_y/E_x and E_x/E_y are varied from 0 to 1, respectively, with the phase remains almost constant at 180°, indicating the LP orientation is varied from 0 to 90° with the slot tuning. Both ideal (Δ markers) and LM tuning ($\times$ markers) effectively achieved the polarization angle tuning, and demonstrate good agreement with simulations (dash lines). From the simulated and measured polarization ratio, the angle of polarization for the LP states can be determined by:

$$\tau = \tan^{-1}|E_x/E_y| = 90^\circ - \tan^{-1}|E_y/E_x| \tag{3.9}$$

The measured broadside axial ratio (AR) and total field directivity for the 6 states with ideal and LM tuning are listed in Table 3.3. The broadside AR for ideal and LM tuning are computed from the measurement in two orthogonal polarizations. For LHCP state a small AR (< 0.5 dB) is observed, indicating good circular polarization. For LP states the large broadside AR (> 28 dB) indicates good linear polarization, with the major axis well aligned to their corresponding polarization angles. The total field directivity measured for ideal cases agrees well with simulations, which maintained around 8 dB with ± 0.5 dB variation among different states. According to the simulated and measured axial ratio for different states, the cross-pol component is very low at broadside, and the total field directivity is therefore very close to the co-pol directivity component, for each polarization state. Note that the directivity is measured in a relative manner, referring to the total power density evaluated through integrating the power intensity (the antenna pattern) captured in all directions. This should not be confused with the realized gain, in which an additional standard gain antenna is typically needed to determine the absolute gain of the antenna-under-test (AUT) through gain comparison.

Fig. 3.19 plots the simulated and measured co-pol and cross-pol radiation patterns in E and H planes for the 6 discrete polarization states, actuated by LM tuning, at the frequency of 2.4 GHz. For the LHCP state the E and H planes are defined by $\phi = 0^\circ$ and $\phi = -90^\circ$, while for LP states the E planes are defined by $\phi = \tau$ and $\phi = \tau - 90^\circ$, according to the polarization angle for each of the states. The measurement results show that the

Table 3.3: The measured broadside AR and total field directivity for CP and LP states with ideal and LM tuning.

Polarization State	L_{lm1} (mm)	L_{lm2} (mm)	Directivity (Simulation)	Directivity (Ideal)	Broadside AR (LM)	Broadside AR (Ideal)
LHCP	21	0	8.31 dB	7.94 dB	0.17 dB	0.41 dB
LP (10°)	21	2	7.71 dB	7.68 dB	41.2 dB	31.5 dB
LP (30°)	21	6.5	7.84 dB	7.81 dB	45.1 dB	51.2 dB
LP (45°)	21	20	8.10 dB	8.06 dB	28.5 dB	30.4 dB
LP (60°)	11.5	20	8.46 dB	8.10 dB	28.8 dB	31.7 dB
LP (90°)	0	20	8.31 dB	7.91 dB	38.2 dB	49.0 dB

polarization reconfiguration has been well achieved for all the 6 measured states, with the cross-pol component in decent level. The radiation pattern in the two principle cuts has not changed appreciably among the CP and LP polarization states, at the frequency of 2.4 GHz. Measurements agrees well with simulations for broadside elevation angles. The deviations at angles from 90 to 270 degree are due to the existence of positioner, mounting fixture, and cable.

3.5 Discussions on Liquid Metal Reconfiguration

As proposing a new reconfiguration technique, it is critical to carefully characterize the properties of switching speed, power handling, insertion and isolation, etc. This chapter summarizes and compares the important properties of liquid metal and other popular switching techniques. The major properties as summarized in Table 3.4.

Since liquid metal reconfiguration relies on the physical motion of relatively linear conductive materials rather than electronic changes in a semiconductor, it is generally believed that liquid metal based devices are capable of handling higher power with better linearity. A recent study in [63] presents a good reference. In this study, two tunable monopoles are built with varactor and liquid metal. Their linearity and power-handling capabilities are tested

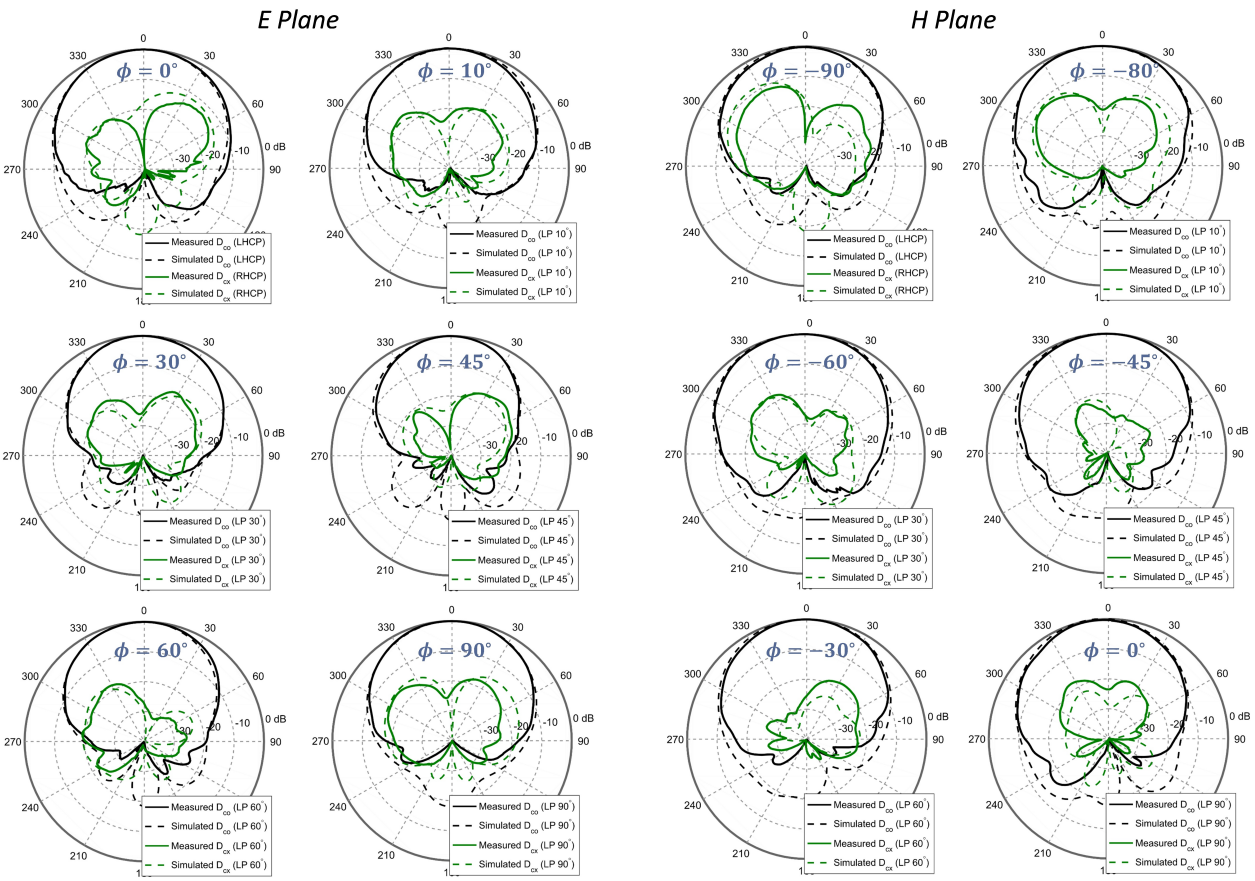

Figure 3.19: The normalized far-field radiation pattern in E and H planes for for 1 LHCP state and 5 LP states with $\tau = 10°, 30°, 45°, 60°$ and 90°, scanned for both horizontal and vertical polarizations at 2.4 GHz. Measurement results (solid lines) are compared with the full-wave simulations (dashed lines).

and compared. The results show that the linearity of the tunable liquid metal monopole is at least 40 dB better than that of the active varactor monopole (characterized by the measured IM3 level). The reconfigurable liquid metal antenna also handles higher power (31 dBm) before failure than the active varactor-tuned antenna (24 dBm).

In terms of isolation and insertion loss, it is also believed that liquid metal based devices should present similar performance to RF-MEMS, since both of them relies on the formation of mechanical contact between conductors. In this study, we built a transmission line switch and characterized the isolation and insertion behavior of the liquid metal based switch. An insertion loss of 0.5 to 1.2 dB is observed from our measurement. While the numbers are

Table 3.4: The circuit model parameters for patch antennas using copper and embroidery patterns with different stitch densities [62].

Electrical Properties	RF-MEMS Switch	PIN Diode	Optical Switch	Varactor Diode	Liquid Metal
DC Voltage (V)	20-100	3-5	1-2	0-30	-
DC Current (mA)	~0	3-20	0-100	0-20	-
Switch Speed	~200 μs	~100 ns	~10 μs	~ ns	~ seconds
Isolation	Very High	High	High	-	Very High
Insertion Loss (dB)	0.05-0.2	0.3-1.2	0.5-1.5	-	0.5-1.2
Linearity	Very High	Medium	Very High	Low	Very High
Tuning Type	Binary	Binary	Binary	Continuous	Continuous

not as good as typical MEMS switch, these are still comparable to PIN diode and optical switch as listed in Table. R2. We believe that these numbers can be further improved by switching to carrier liquid with lower loss (e.g. liquid Teflon).

Regarding the tuning range, liquid metal based reconfiguration is a clear winner over all the existing techniques. Most of the current techniques operate in binary, i.e. on and off. The only exception is varactor diode, which can be continuously tuned over a certain range by varying the biasing voltage. However, the tuning range of varactors are very limited, typically from a few pF to less than 20 pF. Comparing with all the existing techniques, liquid metal holds great potential in achieving more flexible and continuous reconfiguration. The enhanced control over the conductor length and location provided by liquid metal greatly enhances the tuning range.

Despite the advantages of large tuning range and good power handling, one drawback of liquid metal tuning is the switching speed. Current methods of reconfiguring liquid metal resort physical control using syringes and micro-pumps in a closed fluid path. The switching speed required for this kind of physical reconfiguration is not comparable to electrical switching using PIN, MEMS, varactor etc. In our case, the typical time required to transit between two adjacent states is within 1 second, while for two distant states (e.g. $L_s = 40$ mm and $L_s = 0$ mm) the transit time could be as long as 5 seconds. Therefore, the required

time to select each band actually depends on the starting state, and is typically within a few seconds.

There are other important aspects need to be kept in mind, e.g. cost, ease of packaging and miniaturization. Current methods of liquid metal handling generally relies on fluidic control using syringes and pumps. At this point, implementing accurate fluidic control can be costly and sometimes creates a bulky device. Many recent researches in microfluidics focus on the miniaturization of functional fluidic systems. Since the technology itself is still under active research, we believe that with the advance in microfluidics and modern manufacturing, more desirable solutions of liquid metal implementation are expected in the future.

In summary, the drawbacks of liquid metal reconfiguration comparing to other techniques lies in the issue of tuning speed. Cost and packaging might be another factor limiting its application, however, the advance in microfluidics has the potential to provide better solution in the future. Despite these limitations, integrating liquid metal systems into a reconfigurable antenna or microwave system has the potential to deliver a larger number of tunable states, maintaining a high linearity level and a high power handling property. These aims, though difficult to achieve using conventional reconfiguration techniques, are possible with a further in-depth exploration of LM systems.

3.6 Summary

We propose a novel polarization reconfigurable antenna by adding an extended element to the well-know E-shaped patch antenna, and continuously tuning the slots with liquid metal EGaIn. The proposed antenna achieves multi-polarization reconfiguration with a simple and single-feed topology. By tuning liquid metal in the three designed microfluidic channels, the antenna could realize dual CP states and LP states with scanned orientation within two quadrants in x-y plane. We present a thorough circuit model analysis for asymmetric E-shaped patch, which proves the underlying assumption for degenerate orthogonal modes. The design procedures aiming at impedance matching enhancement are also discussed, pro-

viding design guidelines for readers. The prototypes are fabricated, assembled, and measured with real-time liquid metal actuation. Improved fabrication process including an additional sealing step is implemented to promote channel sealing and prevent channel degradation over long-term storage, which helps achieve the good agreement between simulations and measurements.

CHAPTER 4

Organ-tuned Coaxial Monopole Antenna Design for Interstitial Microwave Ablation System

Microwave-induced thermal ablation has emerged as an effective strategy in oncology for treating early stage malignancies of the liver and lung [64]. There are a number of significant advantages of microwave ablation over other types of thermal ablation technologies, including radio-frequency ablation, high-intensity focused ultrasound (HIFU), and laser ablation, with higher temperatures, larger ablation volumes, and shorter ablation times [65]. During a microwave ablation procedure, a coaxial antenna is inserted under computed tomography (CT) or ultrasound guidance percutaneously into the target tumor tissue. Electromagnetic energy is transmitted through an interstitial antenna and delivered into the tissue to cytotoxic temperatures. The end goal of thermal ablation procedures is to heat targeted tissue regions to cytotoxic temperatures with sufficient margins beyond the tumor, all while minimizing damage to non-targeted tissue regions [66]. This minimally-invasive approach often leads to fewer complications, quicker recovery and virtually no blood loss compared to surgical resection [67].

The success of thermal ablation has led to its adoption as first line treatment in patients with early stage liver cancers, with overall survival rates approaching those who undergo surgical resection [68]. Microwave ablations have also demonstrated similar superior efficacy in lung tissue compared to prior ablation modalities, creating hotter and larger ablation zones [69]. And while the clinical data for lung ablation with microwave systems is not as mature as other treatment modalities, the benefits of shorter procedural time and fewer comorbidities continues to present an attractive treatment alternative to surgery [70].

A microwave ablation system consists of ablation antenna or applicator, cooling system and imaging guidance system tailored to specific clinical application. The antenna or applicator is a crucial element for microwave ablation device and has a significant impact on the ablation pattern and ablating power efficiency. The major requirements of ablation antennas including: (a) small diameter for ease of insertion; (b) good impedance matching for efficient power transmission; (c) localized spherical ablation pattern for accurate treatment. Ablation patterns are often characterized in ex-vivo animal tissue, with the size and shape of ablation zone defined by tissue discoloration at elevated temperatures after certain ablation time [71].

In this chapter, we describe analytical solutions for insulating monopole immersed in lossy dielectric media, and based on that, propose a coaxial antenna that can be adaptively tuned with liquid metal to maintain the optimal impedance matching in a varying lossy dielectric environment, as the ablation antenna is applied to different organs or different states of tissue (dehydrated, desiccated, charred), at the frequency of 2.45 GHz. We performed simulations for a tunable coaxial monopole antenna within environments that mimicked the electrical properties of liver, bone and various states of lung tissue, and reflection coefficients are comparing before and after tuning. Ablation performances are validated in ex vivo porcine liver and lung tissue.

4.1 Interstitial Monopole Antennas for Microwave Ablation

Multiple antenna designs have been investigated for percutaneous microwave ablations, including the monopole, dipole, triaxial, slot and floating sleeve antennas [72]. While the size and shape of the final ablation zone has often been cited as the important metrics for evaluating microwave antenna performance, the key performance criteria remains in minimizing the amount of reflected power [73]. The most simple and widely used antenna in microwave ablation is the interstitial monopole antenna, which can be easily constructed from a thin, semi-rigid coaxial cable. There are many types of monopole antenna designs, some of which involve a tip weighting mechanism including open-tip monopole, dielectric-tip monopole, as well as the metal-tip monopole, which uses a metal cap at the distal end of the extended

dielectric-covered inner conductor [74]. Within these variations of a monopole antenna design, power deposition has been theoretically optimized when the length of the elongated conductor was $\lambda_{eff}/4$, where λ_{eff} represents the effective wavelength of the electromagnetic wave within the target tissue. However, the majority of prior optimization studies of the monopole design utilize an iterative process, combining the results of parametric numerical simulation. In an early study exploring the various monopole antenna designs, Nevels et al. and Labonte et al described an optimized monopole design that was iteratively obtained via experimental testing of both the numerical model and the experimental validation within a phantom material [74, 75]. These two studies were able to demonstrate via numerical modeling that the 13 mm exposed monopole antenna had the lowest reflected coefficient. More recently, a design optimization process was described using not only the reflected coefficient but also incorporating specific absorption rate (SAR) and temperature based models into the optimization cost function [76]. The optimal model utilizing an 086 semi-rigid coaxial cable in all of these optimization models has been centered around the 13 mm. Despite general acceptance of this 13 mm length in the 086 cable most likely represent a $\lambda_{eff}/4$, there has not been a demonstrable analytical solution for the λ_{eff} term. In this study we treated our monopole antenna model as an extension of a center-driven insulated dipole, previously described for the purposes of hyperthermia cancer therapy and shale oil extraction [77].

Most clinical microwave ablation systems operate at 915 MHz and 2.45 GHz, frequencies in the industrial, scientific, and medical band that are regulated by the ITU Radio Regulations. The microwave antennas themselves are constructed from coaxial cables, usually composed of a dielectric material sandwiched between a metallic center and outer conductor. Part of the dielectric is exposed through the outer conductor to deliver the microwave energy into the tissue. The configuration and dimensions of the exposed dielectric dictate how well the electromagnetic waves can be delivered into the target tissue. If the load of the ablation antenna is not well matched, there will be high levels of reflected power and the entire shaft of the coaxial cable can experience excessive heating. Modulating the geometry of the coaxial antenna can affect how much energy can be delivered into the tissue, as well as the shape of the heating zone.

When designing the optimal antenna for microwave ablation, a common metric to utilize is the antenna return loss, which is calculated by the ratio of power delivered to the antenna to the power reflected back to the source due to impedance mismatch between the transmission line and antenna, or:

$$\text{Reflection Coefficient } (\Gamma) = 10 \log_{10} \frac{\text{Reflected Power}}{\text{Input Power}} \tag{4.1}$$

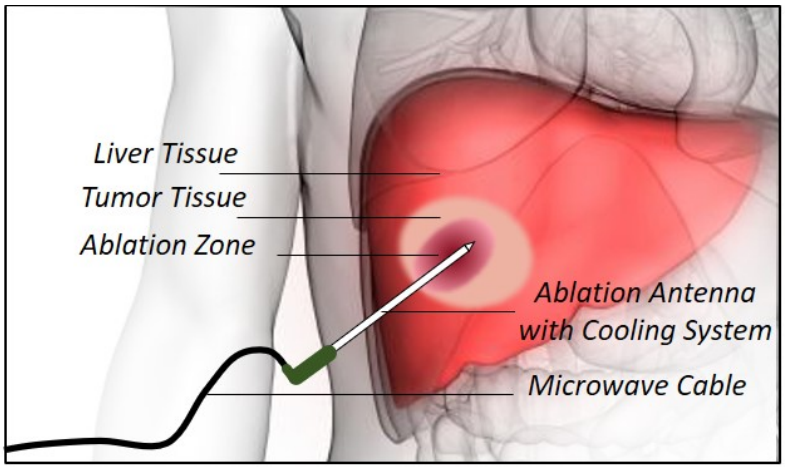

Figure 4.1: A schematic diagram of microwave ablation for liver tumor treatment. An interstitial antenna was inserted into the target tissue to deliver high level microwave power from the cable and destruct cancerous tissue.

Inefficiently designed antennas will reflect more power back into the generator and thus require a user to deliver higher levels of power to create the necessary ablation zone to encompass an entire tumor. Suboptimal attenuation within the feeding transmission line can lead to heating of the applicator, which can spread the ablation zone backwards, causing peritoneal or skin burns in a patient. While active cooling strategies, either via water or gas-cooling, can be utilized to minimize this shaft heating, minimizing the reflected power via efficient antenna design geometry should be prioritized because they reduce the burden on cooling of the feeding transmission line.

The monopole antenna design has been described in current literature, along with its ability to be tuned to liver and lung tissue [74, 75, 78, 79]. These studies have described

similar antenna geometry dimensions for a liver-tuned monopole antenna design using an 0.086" coaxial cable [76]. However, these studies utilized an iterative approach via numerical simulation or experimental method, without a clear analytical approach to explain how the antenna geometry related to the electrical properties of the liver. In this study, we describe an analytical solution for the electromagnetic field generated by an organ-tuned monopole antenna design with a specified dielectric load. In this particular case we chose to utilize the liver and the lung – organs with vastly different dielectric properties due to their varying concentrations of parenchyma, blood and air. We utilized this analytical solution to construct a microwave antenna using a semi-rigid 0.086"coaxial copper cable. Microwave ablation zones using these organ-tuned antennas were then created to validate their energy delivery efficiency in a volume-controlled ex vivo ventilated lung and an ex vivo porcine liver model.

4.2 Analytical Modeling for an Insulating Monopole Antenna Immersed in Lossy Medium

Semi-rigid coaxial cables have been widely used as feeding transmission lines between power generator and applicator, and most microwave ablation antennas are readily integrated by modifying the geometry of the end of cable. In this section, we analyze a monopole antenna formed by stripping off a section of outer conductor at the end of coaxial cable by length of $L_{ant} = \lambda_{eff}/4$, where λ_{eff} represents the effective wavelength for the coaxial antenna design. Fig. 4.2 illustrates the structure of a coaxial monopole antenna.

The effective quarter wavelength can be analytically found through the insulating antenna theory for an inner conductor wrapped with multiple dielectric layers and immersed into lossy dielectric medium [77]. The theory was originally developed for an insulating antenna immersed in a homogeneous dissipative medium such as sea water [80]. In our case, the insulating monopole antenna consists of a central conductive cylinder with radius a and length h (representing the inner conductor of coaxial cable), wrapped by cylindrical dielectric region with radius b and dielectric constant ϵ_2 (representing the Teflon filled in coaxial cable),

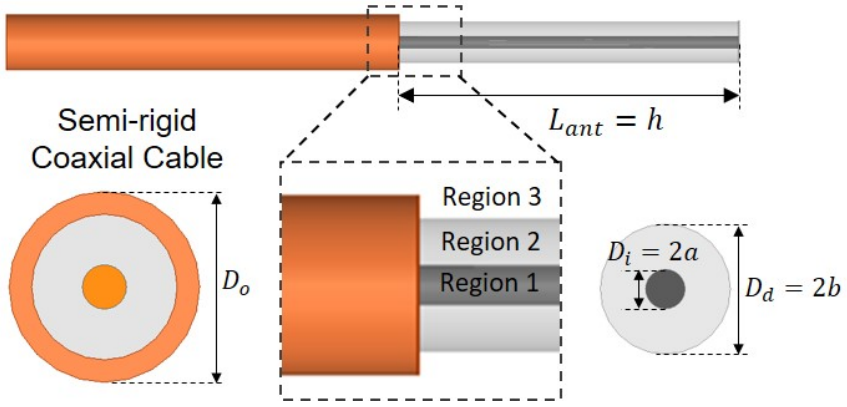

Figure 4.2: Coaxial monopole antenna formed by stripping off a section of outer conductor at the end of coaxial cable by $\lambda_{eff}/4$, with the dimensions corresponding to 086 and 021 standards listed below.

immersed in infinite homogeneous medium with dielectric constant ϵ_3 and conductivity σ_3. The three regions corresponding to different dielectric properties are identified in Fig. 4.2. The wavenumber in the insulating and lossy dielectric regions are therefore:

$$k_2 = \omega\sqrt{\mu_0\epsilon_2}, \quad k_3 = \omega\sqrt{\mu_0(\epsilon_3 + j\sigma_3/\omega)} \tag{4.2}$$

where μ_0 is the free space permeability assumed to apply in all regions. The theory required that the wavenumber in ambient medium is greater than that of the insulating dielectric, and the cross section of the antenna is electrically small [77]:

$$|k_3/k_2|^2 \gg 1, \quad (k_2 b)^2 \ll 1 \tag{4.3}$$

Assuming the antenna is excited with voltage source V_0^e, the current carried by the antenna central conductor is given as [77]:

$$I(z) = -j\frac{V_0^e}{2Z_c}\frac{\sin k_{eff}(h - |z|)}{\cos k_{eff} h} \tag{4.4}$$

And the characteristic impedance Z_c and the effective propagation constant k_{eff} are given by [77]:

$$Z_c = \frac{\omega\mu_0 k_{eff}}{2\pi k_2^2}[\ln\frac{b}{a} + \frac{k_2^2}{k_3^2}\frac{H_0^{(1)}(k_3 b)}{k_3 b H_1^{(1)}(k_3 b)}] \tag{4.5}$$

$$k_{eff} = k_2[\frac{\ln(\frac{b}{a})k_3 b H_1^{(1)}(k_3 b) + H_0^{(1)}(k_3 b)}{\ln(\frac{b}{a})k_3 b H_1^{(1)}(k_3 b) + \frac{k_2^2}{k_3^2}H_0^{(1)}(k_3 b)}]^{1/2} \tag{4.6}$$

where $H^{(1)}$ represents Hankel function of the first kind. It can be readily verified that as k_3 approaching to k_2, the effective propagation constant k_{eff} also approaches to k_2, reducing the case to a bare conducting monopole antenna immersed in lossless dielectric medium. The effective propagation constant k_{eff} can be directly linked to the effective wavelength $\lambda_{eff} = 2\pi/k_{eff}$, from which the optimal length of monopole antenna is determined. For the expression of Z_c, it has been proven that (4.5) is applicable (with error within 5%) only under the condition of $|k_3|^2 \geq 14.4|k_2|^2$ [80].

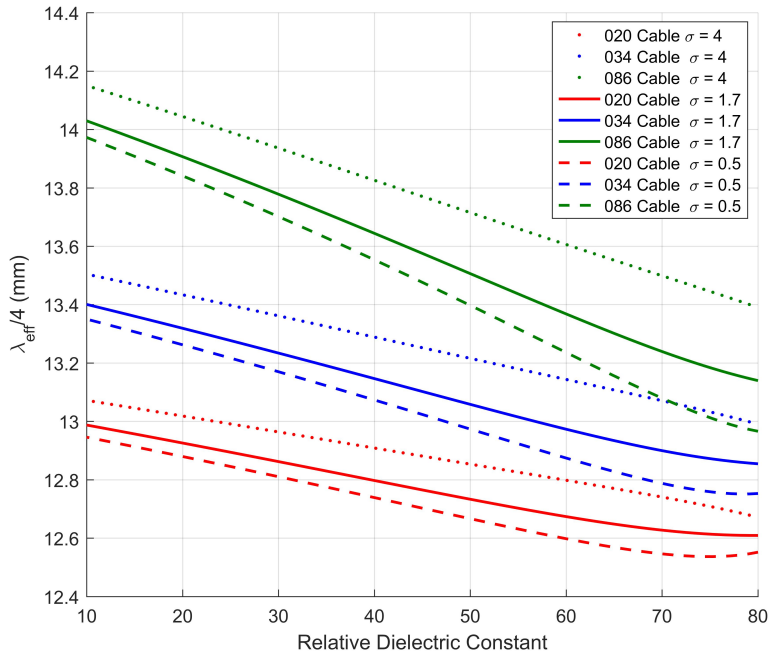

Figure 4.3: The effective quarter wavelength according to the insulating antenna theory, for the coaxial antenna consisting of an inner conductor wrapped with dielectric coating and inserted into lossy dielectric medium.

The effective quarter wavelength was computed with $\lambda_{eff}/4 = \pi/2k_{eff}$ and plotted in

Table 4.1: The dimensions of coaxial cable with the 086, 034 and 020 standards and the dielectric properties for lung and liver tissues.

Cable	Dielectric ϵ_r	D_i (mm)	D_d (mm)	D_o (mm)
086	2.1	0.51	1.68	2.21
034	2.1	0.20	0.66	0.86
020	2.1	0.10	0.38	0.51

Fig. 4.3 for 086, 034 and 020 cable standards with varying tissue dielectric constant and conductivity. The dimensions of coaxial cable are listed in Table 4.1. At relative dielectric constant around 40, it is interesting to note that the effective quarter wavelength ranges from 12.7 to 13.8 mm for the 3 cable standards. The use of 13 mm coaxial monopole has been widely adopted for microwave ablation procedures in liver, which agrees with the analytical solution [74, 76].

From the analytical solution, we found that the effective quarter wavelength is not very sensitive to the variation of tissue dielectric property, which varies only within the range of ± 1 mm for ϵ_r from 10 to 90 and σ_r from 4 to 0.5 S/m. However, the small deviation of impedance matching condition could result in a relatively large increase in the reflected power, due to the high power level of incident power (typically in the range of 50 to 150 W). To our best knowledge, this is for the first time that the use of 13 mm is explained analytically by equation (4.6).

4.3 Experimental Validation

A monopole antenna was constructed from polytetrafluorethylene (PTFE) filled, semi-rigid coaxial cable (UT-085C; Micro-Coax LLC, Pottstown, PA) with an active length of 13.0 mm and 15.5 mm, respectively. An industrial high-powered solid state microwave generator (Sairem, Neyron, France) was used to create the ablation zones.

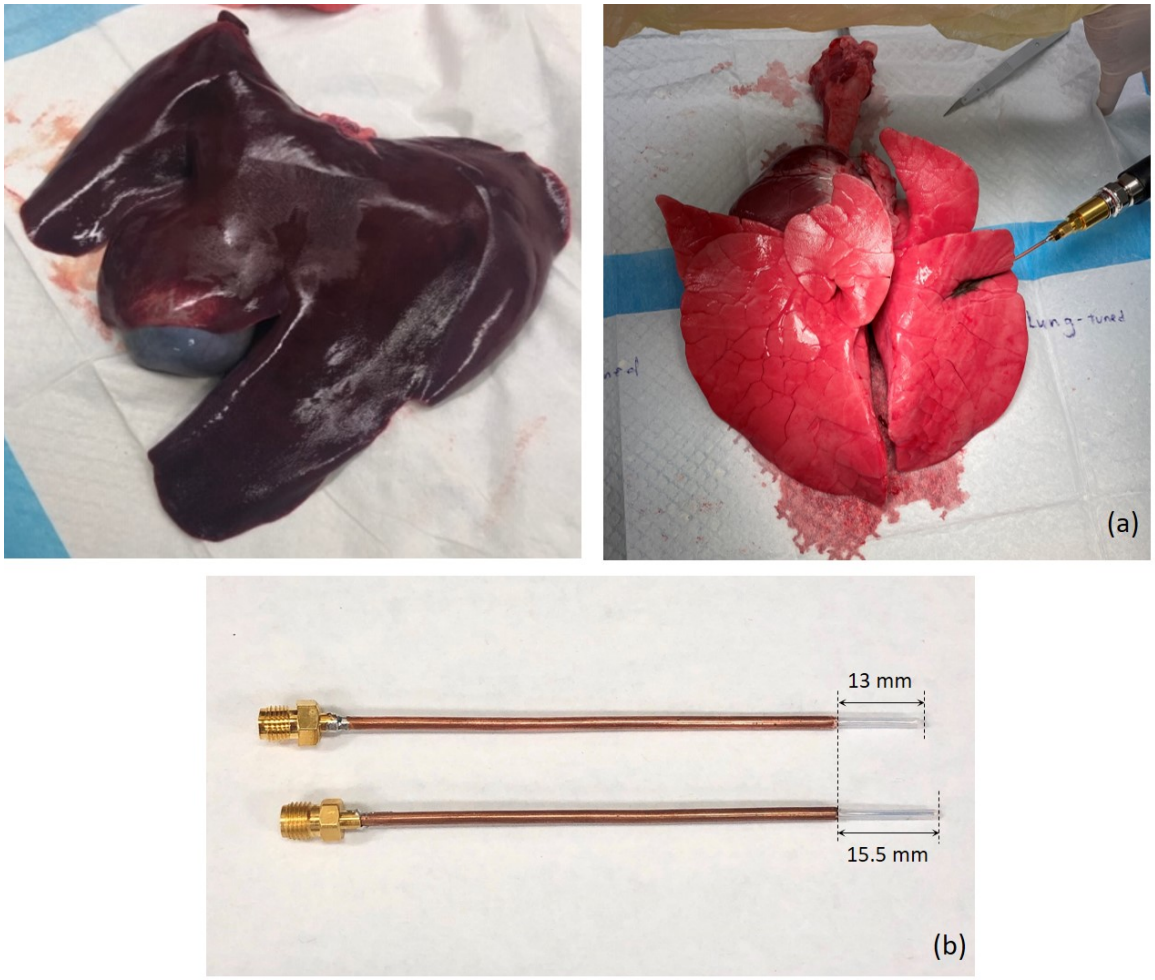

Figure 4.4: (a) Sample set up of the ex vivo porcine liver and lung study. (b) Images of the liver-tuned and lung-tuned monopole antennas, with exposed monopole lengths of 13 mm and 15.5 mm, respectively.

Microwave ablation experiments were performed on freshly excised ex-vivo porcine lung tissues with attached airways. The lung tissue was mechanically ventilated to maintained a 600 mL volume controlled airspace to mimic a fully expanded lung. The lung tuned antenna built from an 086 semirigid coaxial cable with a 15.5 mm radiating segment was inserted into the upper, middle and lower lung fields in the left lung. Likewise, ablations were created using a 13 mm radiating segment in the right lung. Images of the two antennas and the ventilated lung are demonstrated in Fig. 4.4. Microwave power was delivered from SAIREM GMS200W Microwave Generator at 50 W for 1 minute with reflected power being recorded in

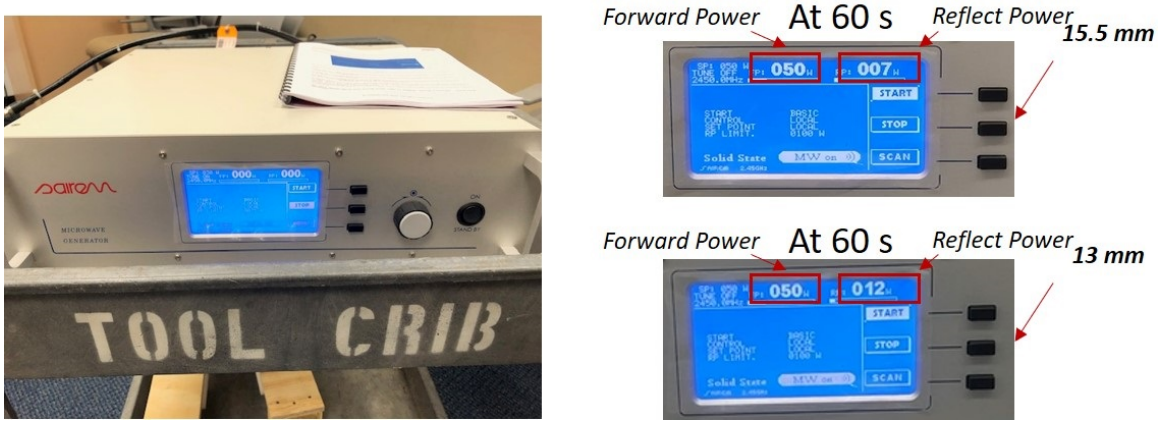

Figure 4.5: SAIREM GMS200W Microwave Generator was used to deliver 50 W microwave power into the interstitial ablation antenna. Input and reflected power were recorded from the panel with 5 seconds intervals.

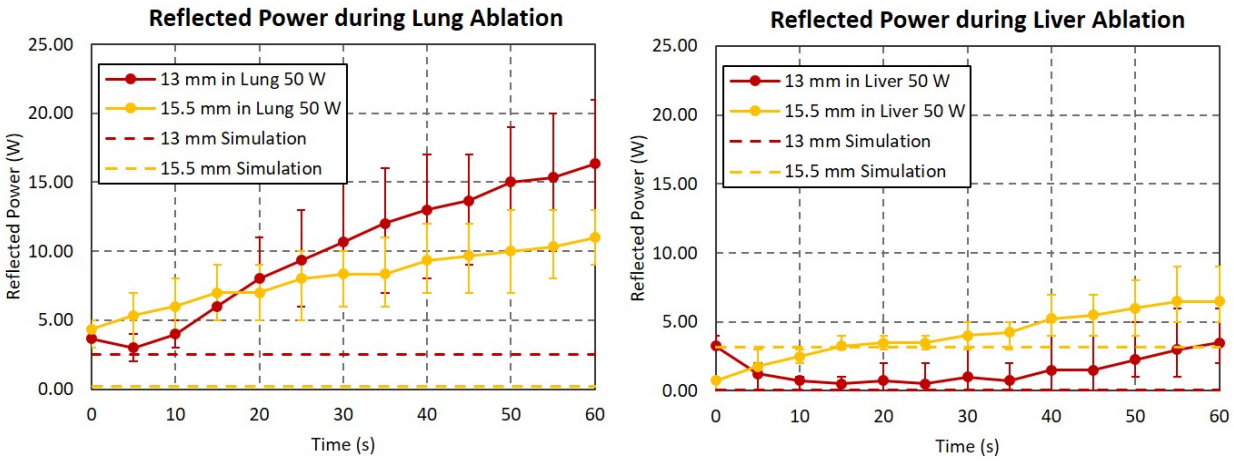

Figure 4.6: Reflected power across each organ-tuned antenna in the: (a) ex vivo ventilated porcine lung model and (b) ex vivo porcine liver model. Within the lung model, the lung-tuned antenna had significantly less reflected power compared to the liver-tuned antenna. Likewise, in the liver model, the liver-tuned antenna had significantly less reflected power compared to the lung-tuned antenna.

5-second intervals, as shown in Fig. 4.5. Ablation zones were also created on freshly excised ex-vivo porcine liver. A total of n = 7 ablation zones were created with the lung-tuned

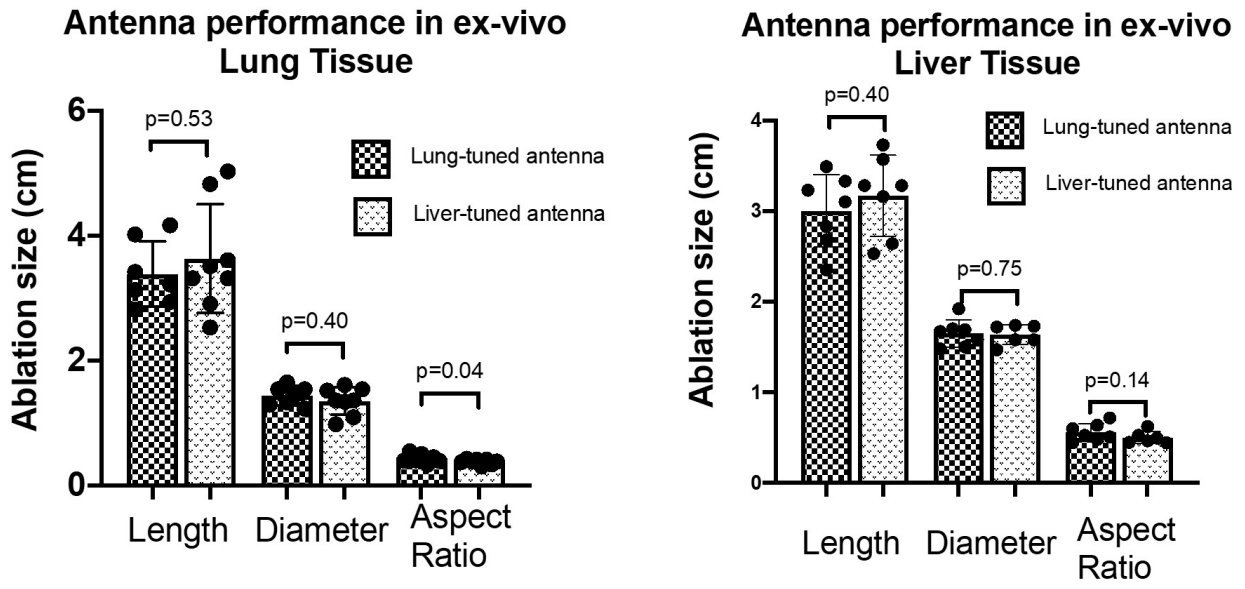

Figure 4.7: Microwave ablation measurements in: (a) lung Tissue and (b) liver tissue. Ablation sizes between lung and liver tissue were not significantly different in length and diameter. However, the lung-tuned antenna had a significantly higher aspect ratio compared to the liver-tuned antenna, suggesting a more spherical ablation zone. This may be due to the significantly less reflected power seen in lung-tuned antennas, which can extend the length of an ablation zone, compared to the liver-tuned antennas.

antenna and liver-tuned antenna.

After the ablations were completed, ablation zones were sectioned across their insertion path, revealing a cross section of the ablation zone. The congestive component of the ablation zone was measured, as well as the inner charred component. Ablation length and width were recorded and compared between antennas. Student t-test was performed to evaluate differences in each ablation zone metric.

Monopole antennas were constructed from polytetrafluorethylene (PTFE) filled, semi-rigid coaxial cable (UT-085C; Micro-Coax LLC, Pottstown, PA). Lung-tuned antennas had an exposed PTFE length of 15.5 mm while liver-tuned microwave antennas had an exposed PTFE length of 13.0 mm. Both monopoles were having their inserted section of copper

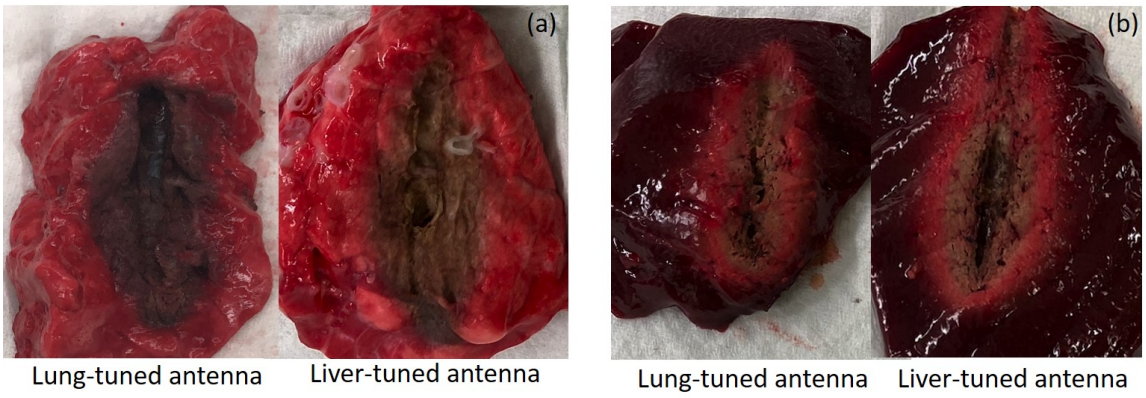

Figure 4.8: (a) Sample of ablated lung tissue: Right - lung tuned antenna vs left - liver tuned antenna. Note that the lung-tuned antenna created a more spherical ablation zone compared to the liver-tuned antenna. (b) Sample bloc of ablated liver tissue: Right - lung-tuned antenna and left - liver tuned antenna. The liver tuned antenna created a significantly larger area of charring in the center of the ablation zone (yellow arrow) compared to the lung-tuned antenna, likely due to more efficient energy delivery into the tissue.

wrapped with PTFE film to promote insertion.

Within the lung tissue, both the liver-tuned and lung-tuned antenna exhibited a monotonic increase in reflected power over time. The lung-tuned antenna had a significantly smaller reflection coefficient at the end of the ablation session (11.80±3.03 vs 16.3±3.09 W, p=0.03). Within the liver tissue, the liver-tuned antenna was able to deliver energy more efficiently measuring significantly less reflected power compared to the lung-tuned antenna (3.00±1.52 vs 6.57±01.61 W, p=0.0005) (Fig. 4.6).

Within the ex-vivo ventilator-inflated lung tissue, the lung tuned antennas demonstrated a larger ablation zone width (1.43±0.15 vs 1.35±0.22 cm, p=0.40) but shorter ablation length (3.38±0.52 vs 3.63±0.87, p=0.53), although neither differences were found to be statistically significant. However, the lung-tuned antenna had a larger ablation aspect ratio compared to the liver (0.43±0.07 vs 0.38±0.04, p=0.04) (Fig. 4.7 (a)). The charred component of the microwave ablation zone in the lung was non-measurable.

In the ex-vivo liver tissue the lung-tuned antennas demonstrated a similar ablation zone

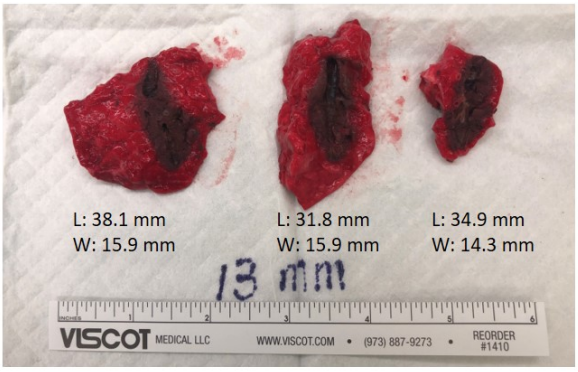

Average L: 34.9 mm; W: 15.4 mm

Average L: 33.4 mm; W: 15.1 mm

Average L: 29.8 mm; W: 16.3 mm

Average L: 34.2 mm; W: 17.9 mm

Figure 4.9: The total samples of lung and liver tissues after ablations.

width (1.64±0.15 vs 1.62±0.12 cm, p=0.75) and ablation length (3.00±0.40 vs 3.20±0.45 cm, p=0.40), although neither differences were found to be statistically significant. The lung tuned antenna had a larger ablation aspect ratio compared to the liver (0.56±0.09 vs 0.42±0.20, p=0.14), although this difference was not significant. The charred component of the ablation zone in the liver for the liver-tuned antenna was significantly larger compared to that in the lung-tuned antenna (0.36±0.09 vs 0.24±0.05 cm, p=0.01) (Fig. 4.7 (b)).

4.4 Tunable Coaxial Monopole Antenna for Optimal Impedance Matching for Varying Tissue Properties

The effective quarter wavelength is not very sensitive to the variation of tissue dielectric property, which varies only within the range of ±1 mm for ϵ_r from 10 to 90. However, the

small deviation of impedance matching condition could result in a relatively large increase in the reflected power, due to the high power level of incident power (typically in the range of 50 to 150 W). Adaptive tuning for the coaxial antenna is therefore desirable to accommodate various tissue properties among different organs. Fig. 4.10 plots the full-wave simulation results of S_{11} with monopole length tuned for different tissue (inflated and deflated lung tissue in (a) and (b), bone, and normal liver tissue in (c) and (d)), comparing with a fixed 13 mm monopole. At the operating frequency of 2.45 GHz, 5 to 10 dB improvement in S_{11} was observed, with only minor tuning on the monopole length within a 3 mm range. Fig. 4.11 illustrates the fullwave simulation results for the specific absorption rate (SAR) in the inflated lung tissue with 13 mm and 15.5 mm monopoles. It is cleared observed that the monopole with 15.5 mm in length delivers microwave power more efficiently in the specific tissue region.

4.5 Liquid Metal Implementation for Tunable Coaxial Antenna

The aforementioned tuning requirement can be well-addressed by pressure-actuated eutectic gallium-indium (EGaIn). EGaIn is a liquid metal alloy at room temperature that demonstrates low toxicity, high conductivity (3.4×10^6 S/m) and very good flexibility [47]. Besides the advantages stated in Chapter 3, implementing liquid metal-based tuning with flexible tubes to build interstitial antenna with mechanical flexiblility facilitates less invasive ablation procedures, with the applicator reaching the target lung tissue through air way. Fig. 4.12 illustrates the design of liquid metal actuated tunable coaxial monopole. 086 coaxial cable was stripped off with exposed inner conductor at the end and interconnected to a section of polytetrafluoroethylene (PTFE) tube with 1/16" inner diameter, which was then connected to another section of PTFE tube with 1/32" inner diameter. The liquid metal was partially filled within the tubes and passes across the interface. The remaining volume of the tubes was filled with carrier liquid mineral oil, with optical transparency and low loss in radio frequency (with $\tan\delta < 0.01$). Since the inner connector was in direct contact with liquid metal plug, the total monopole length was measured from the end of outer conductor to right

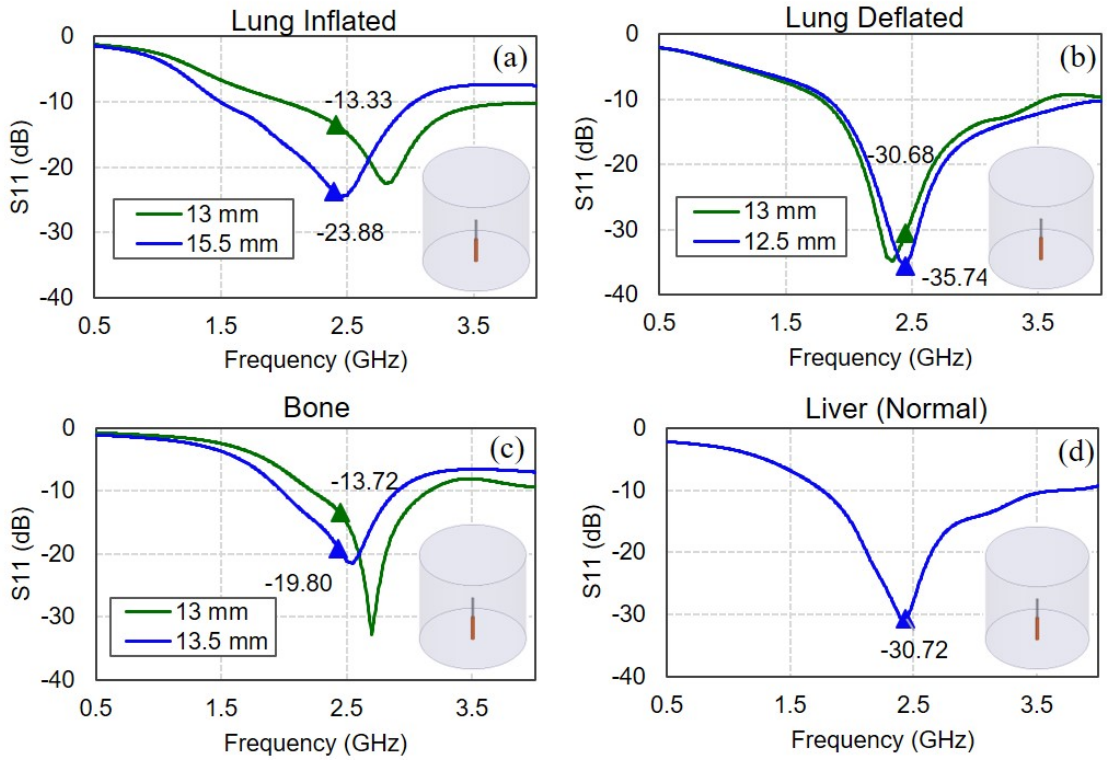

Figure 4.10: Full-wave simulation of S_{11} with tuned monopole length for inflated (a) and deflated (b) lung, bone (c), and normal liver (d) tissue, comparing with a fixed 13 mm monopole. The inset figure illustrates the model setup in HFSS, with a coaxial monopole inserted into a cylindrical lossy dielectric box mimicking the surrounding tissue.

interface between liquid metal and oil. The section of air sealed at the end of th 1/32" tube provided a reversible tuning range of a few millimeter, that was pneumatic driven by syringe or pressure regulator. The liquid metal coaxial monopole could therefore operate with a tunable length to achieve the optimal impedance matching under varying tissue dielectric properties.

4.6 Summary

In this study, we created an analytical model that optimized the traditional monopole design to minimize the reflected coefficient in an ex-vivo porcine lung and liver model. To our

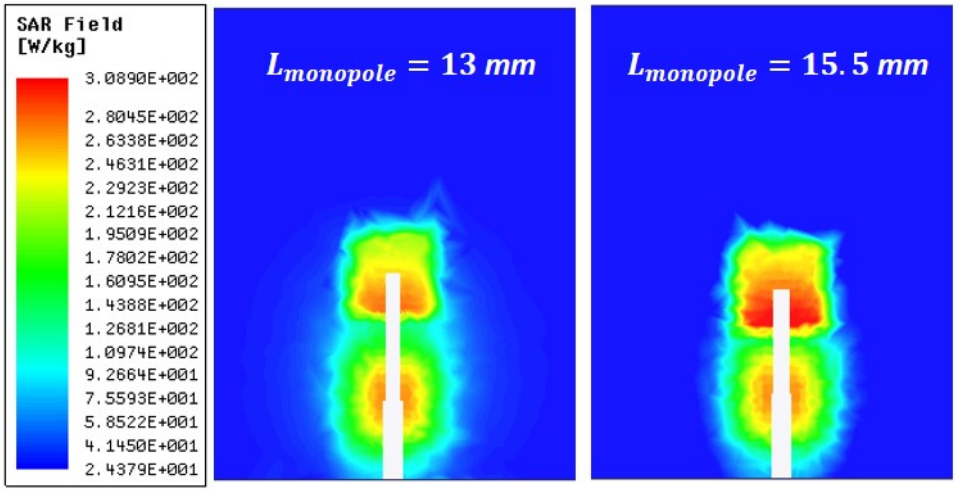

Figure 4.11: Simulated SAR in inflated lung tissue with 13 mm and 15.5 mm monopoles. It is observed that 15.5 mm monopole delivers microwave power more efficiently in the tissue region.

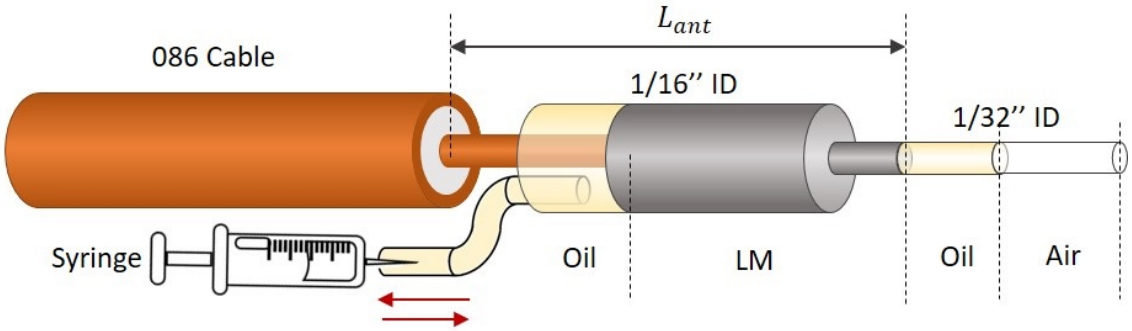

Figure 4.12: The design schematics of the liquid metal tunable coaxial monopole antenna actuated by syringe.

knowledge, this is the first model that took into account the air content within an ex-vivo porcine lung model. During validation, a clinical-grade ventilator was used to maintain the air content for the duration of the ablation procedure. This study showed that a lung-tuned antenna experienced significantly less reflected power, and created significantly more spherical ablation zones compared to liver-tuned antennas within the ventilated ex-vivo lung tissue. Our study also showed significantly more charred tissue volume in a liver using a liver-tuned antenna. While these improved heating metrics between tuned antennas in their

respective tissue organs did not change overall ablation dimensions, the results suggest that organ-tuned antennas can deliver energy more efficiently into their respective tissue.

Antenna tuning for the purposes of organ-specific microwave ablation remain an important area of research in the field of interventional oncology. We propose a tunable coaxial antenna for microwave ablation capable of maintaining the optimal impedance matching in different organs of treatment. The tuning was achieved by small physical motion of liquid metal plug actuated by syringe. Future works on the proposed tunable antenna including ex-vivo and in-vivo testing on the reflected power and ablation pattern in various tissues with liquid metal tuning implemented.

Part II

Conformal Patch Antennas based on Electro-Textile for Body-Area Network Applications

CHAPTER 5

Embroidered Textile Antenna Design and Accurate Modeling

The recent advances of wearable electronics gives an increasing need for developing wearable antennas that are compact, robust, low cost and easy to use [81]. In the literature, a variety of solutions to develop textile integrated antenna or circuit has been developed. Embroidered techniques [82–85], nonwoven solutions [86], designs based on using several fabrics with different electromagnetic behaviors [87, 88], or inkjet-printed patterns over textile substrates [89–91] are some of the most cited solutions. Embroidery-based technique have large potentials to meet many of these requirements, with the modern computerized embroidery machines that are fast and cost effective in pattern generation. Most commonly the fabrication involves weaving of conductive threads onto a non-conductive textile substrate. Available conductive threads include X-Static [92], Shieldex [93], Amberstrand [94] etc.

In order to accurately characterize the embroidery-based antenna, several important features need to be carefully considered. First, the conductive and dielectric material properties need to be characterized. Second, embroidered antennas generally have double-sided nature since the conductive threads form surfaces on both top and bottom of the fabric. The threads are aligned in a preferred direction and are not in perfect contact with each other along their full lengths. Finally, the embroidery pattern is not as uniform as the conventional conductive materials, especially on the bottom layer. The thread residues defined by the fabrication process also affect the structure on edges significantly. Owing to these limitations, it is not easy to define an electromagnetic model that accurately describes the properties of the embroidered antenna while maintaining a clear link with the structure of the prototype.

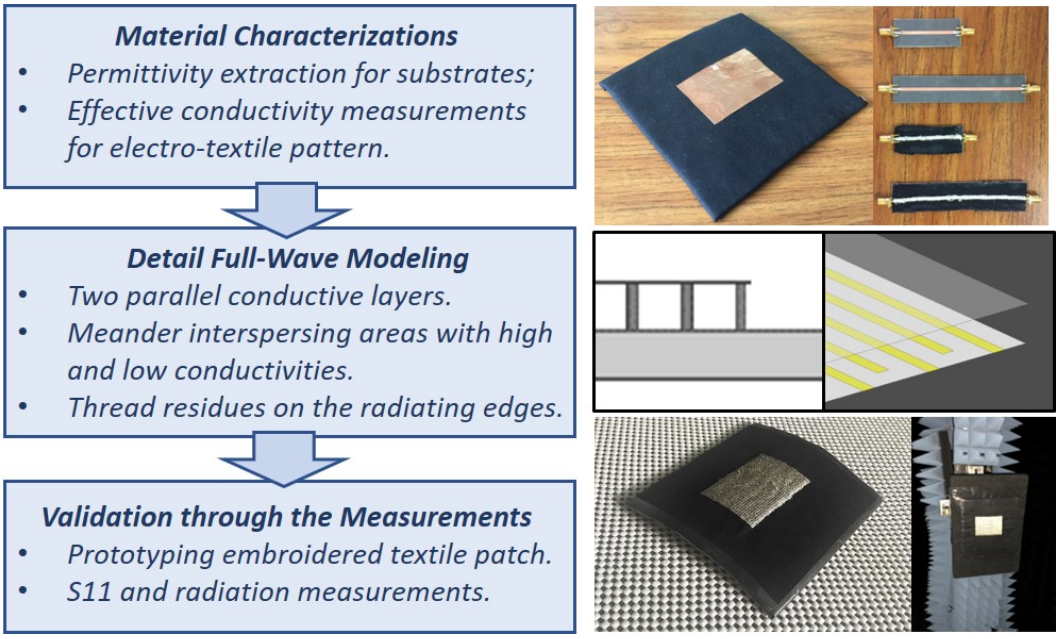

Figure 5.1: A flowchart illustrating the modeling procedures for the embroidery-based textile rectangular patch antenna.

In this chapter, the methodology of material characterization and modeling strategies have been presented for embroidered textile rectangular patch antennas. A flowchart that illustrates the modeling procedures is shown in Fig. 5.1, with details discussed in the following sections.

5.1 Textile Material Characterization

The study of electro-textile antennas starts with the detailed characterization of the material. The accurate description of the substrate permittivity is the key to the accurate tuning of the patch antenna resonant frequency. The determination of the effective conductivity is critical for the prediction of radiation efficiency and the input impedance.

The methods to determining the substrate permittivity varies. In this work the method of patch antenna resonant frequency matching method is utilized. We first constructed the patch antenna using copper foil with known thickness and conductivity, and measured the resonant frequency. A full-wave simulation is then conducted in HFSS to match the measured

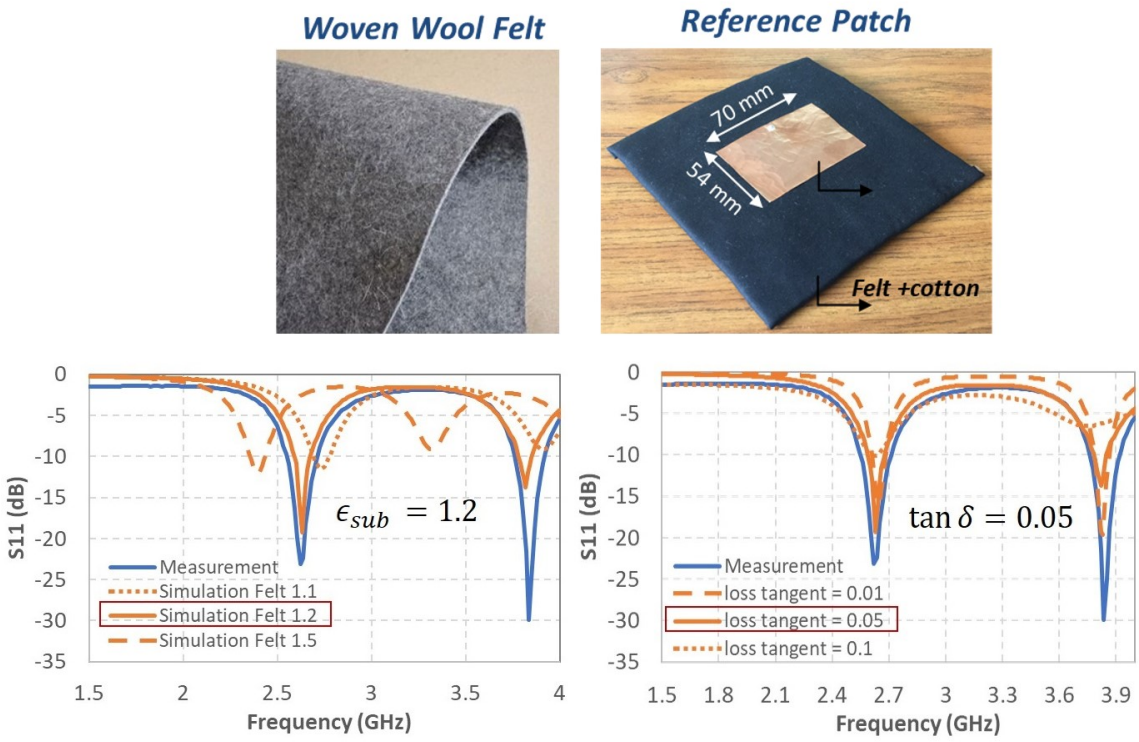

Figure 5.2: The dielectric constant and loss tangent of the substrate is characterized by matching the measurement result with the simulations in various cases.

resonant frequency by sweeping the permittivity of the substrate. Adhesive back felt fabric is used as the substrate material, and its dielectric constant is determined to be 1.2. The loss tangent is specified as 0.05.

The conductivity of the electro-textile pattern embroidered using computerized embroidery machine is not obvious even if the linear conductivity of the electro-textile threads are given. The effective conductivity depends on the stitch type, density and the measurement direction because the electro-textile patterns are anisotropic. The full wave simulation of embroidered structure is difficult because the detailed structure of embroidery are not easy to model. The effective conductivity of the electro-textile pattern can be characterized with a four-micro-strip line method proposed in [23]. The method constructs four micro-strip lines with different lengths: two copper lines with copper on the top and bottom with two different lengths, two electro-textile lines with electro-textile pattern on the top and copper on the bottom, with the same lengths as the copper lines. The steps to determine the effec-

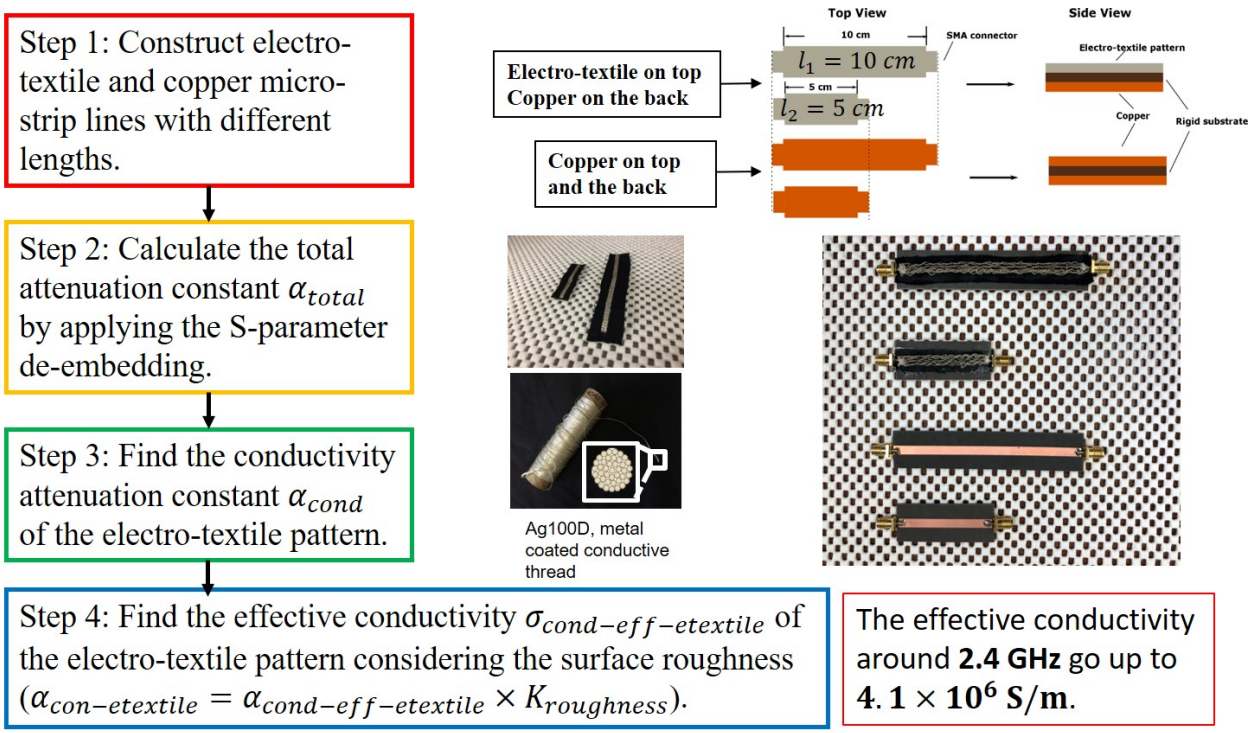

Figure 5.3: The steps to get the effective conductivity of the electro-textile patterns using four-micro-strip line method.

tive conductivity of the electro-textile conductive surface is illustrated in Fig. 5.3. In Step 1 the four microstrip lines are constructed. In Step 2 the magnitude of the S_{21} are measured for each of the four cases. The total attenuation constants for copper and electro-textile microstrip lines are calculated based on the measured S_{21}. In Step 3, by assuming that the dielectric and radiation loss are the same among copper and electro-textile lines, the conductivity attenuation constant of the electro-textile patterns are separated from the the dielectric and the radiation losses. In Step 4, the effective conductivity of the electro-textile pattern can be determined by comparing with the known copper conductivity, considering the effect of surface roughness. The surface roughness factor can be calculated by [95, 96]:

$$K_{roughness} = 1 + \frac{2}{\pi} \tan^{-1}(1.4 \frac{\Delta_{surface\ roughness}}{\delta_{skin}}) \tag{5.1}$$

where $\Delta_{surface\ roughness}$ is the height of the rough surface triangle from the bottom to the top of the embroidery pattern, and δ_{skin} is the skin depth.

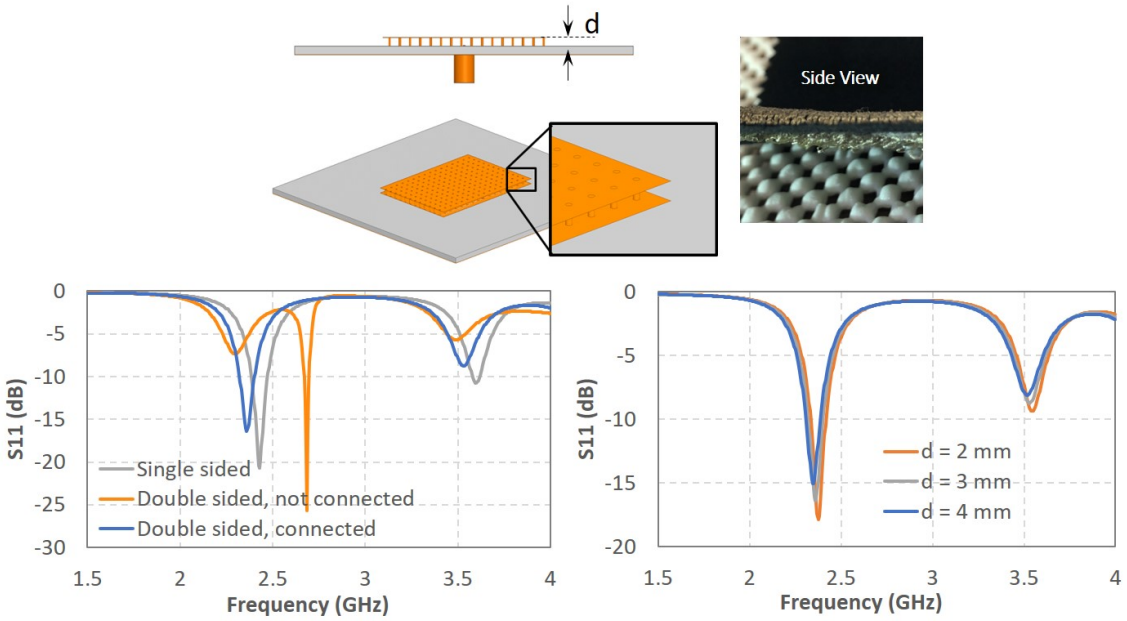

Figure 5.4: The double-layer nature of embroidered pattern is modeled by 2 conductive layers separated by distance d, and connected by 12×16 vias. The double-sided patch results in lower shift of resonant frequency. By increasing the separation d between the two conductive layers, the lower shift also slightly increases.

Additionally, the loss and perturbation of the connectors are also de-embedded during this process. For electro-textile pattern embroidered with Syscom Ag100D using running stitches, 0.8 mm distance between the adjacent lines, and 5 stitch/cm, the effectivity conductivity is around 4.1×10^6 S/m around 2.5 GHz.

5.2 Detail Modeling Strategies of Embroidered Patch Antenna

The double-sided nature of the embroidery pattern is modeled by two parallel conductive layers separated by a distance of $d = 3$ mm, which is selected based on measuring the embroidery pattern produced by the same embroidery machine. To emulate the interconnection between the two parallel layers, they are connected by a 12×16 conductive cylinder-array with diameter of 0.5 mm that distributed over the surfaces. The modeling of double layer

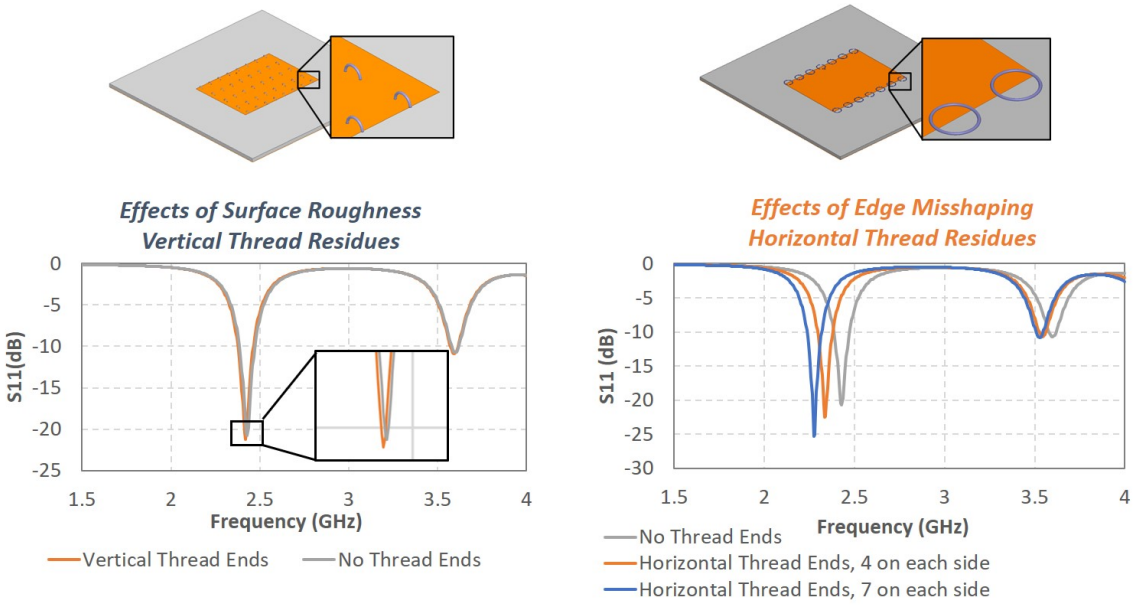

Figure 5.5: The modeling of thread residues. Lower shift of resonant frequency is observed for horizontal thread ends, and no significant effects of the vertical thread ends is observed.

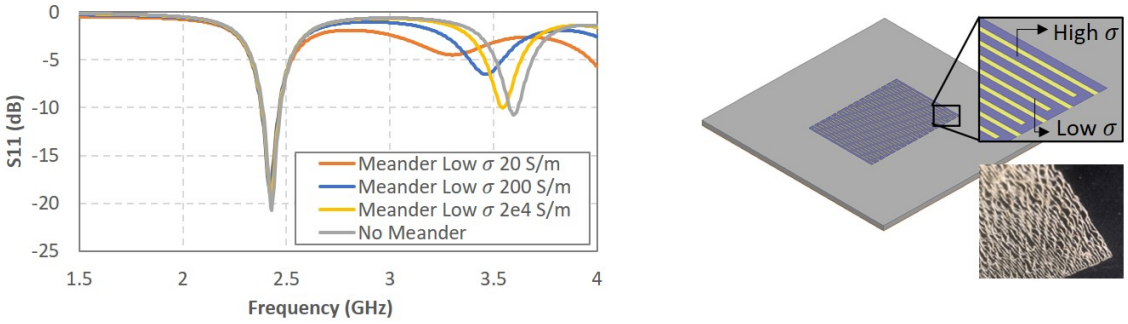

Figure 5.6: The surface is modeled by meander "fiber" with high conductivity separated by low conductivity material.

is illustrated in Fig. 5.4. It is observed that the double sided patch results in lower shift of resonant frequency. By increasing the separation d between the two conductive layers, the lower shift also slightly increases.

Besides the double layer structure, the thread residues that irregularly distributed along the two radiating edges also significantly affect prediction of the resonant frequency, owing to the additional thread that the sewing machine takes when it is routed to change direction

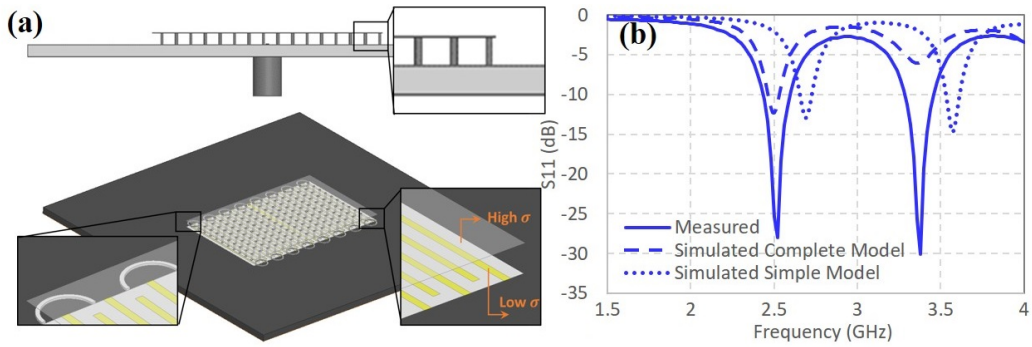

Figure 5.7: (a) A detailed full-wave model that accounts for the double-sided embroidery nature of the electro-textile patch antenna. (b) The simulation S_{11} with the complete and simple models are compared.

between two adjacent stitches. Fig. 5.5 illustrates the modeling of thread residues that distribute vertically and horizontally. Element ring-arrays are assigned with diameter of 3 mm for each of the ring elements. The dimensions of the rings that used to model the thread residue is related to the stitch density of the embroidery pattern. We observe a lower shift of the resonant frequency with the horizontal thread residues. And we also found that there is no significant effect of the vertical thread residues.

In order to model the nonuniform conductivity distribution over the surface, a similar approach as proposed in [97] is used. The embroidered conductive surface is modeled by interspersing good conductive areas that emulate the threads with lower conductivity areas to provide a model for the higher resistance paths between adjacent threads. The conductive areas that models the embroidery thread form a meander pattern aligned in the stitching direction and distributed across the surface. The high-conductivity areas are formed by a series of rectangular strips with width of 1.5 mm and conductivity assigned as 4.1×10^6 S/m. The high-conductivity strips are connected end-to-end, while the gaps are filled by areas with low-conductivity assigned as 100 S/m.

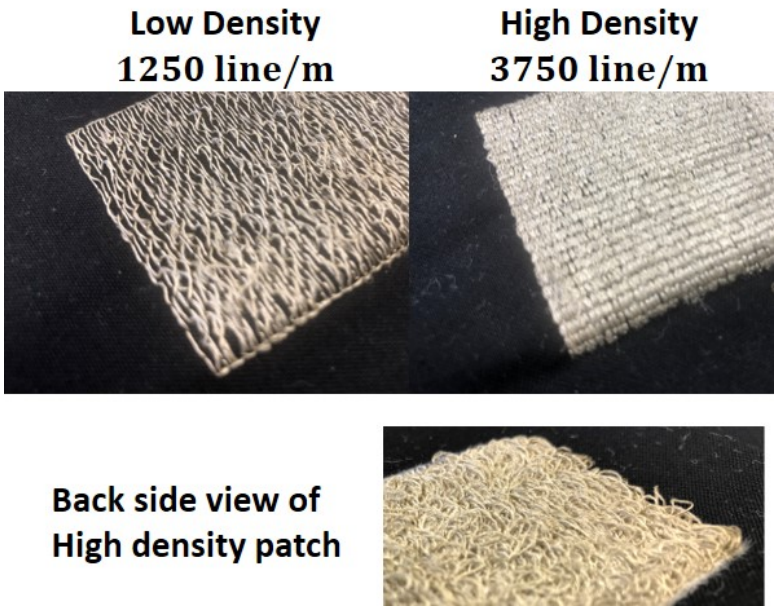

Figure 5.8: The pictures for embroidery pattern with low (1250 lines/m) and high (3750 lines/m) stitch densities.

Table 5.1: The detailed full-wave model parameters for high and low stitch densities.

Density	Double Layer Thickness d	Thread Residue Torus r	Meander Low Conductivity σ
1250 line/m	0.5 mm	1.2 mm	50 S/m
3750 line/m	3.0 mm	3.2 mm	200 S/m

5.3 Stitch Density Study

The stitch density of the embroidery pattern is a critical parameter in designing and fabricating electro-textile patch antennas. The effect of stitch density should be properly reflected by the detail full-wave model parameters, e.g. the double-layer thickness d, the ring radius r, and the interspersing high-low conductivities σ_h and σ_l. Two cases of stitch densities (1250 line/m and 3750 line/m) are studied to compare the variations in full-wave modeling parameters. The prototypes with different stitch densities are fabricated, and S_{11} for each case is measured and compared with the detailed full-wave models to find the proper parameters, as listed in Table. 5.1.

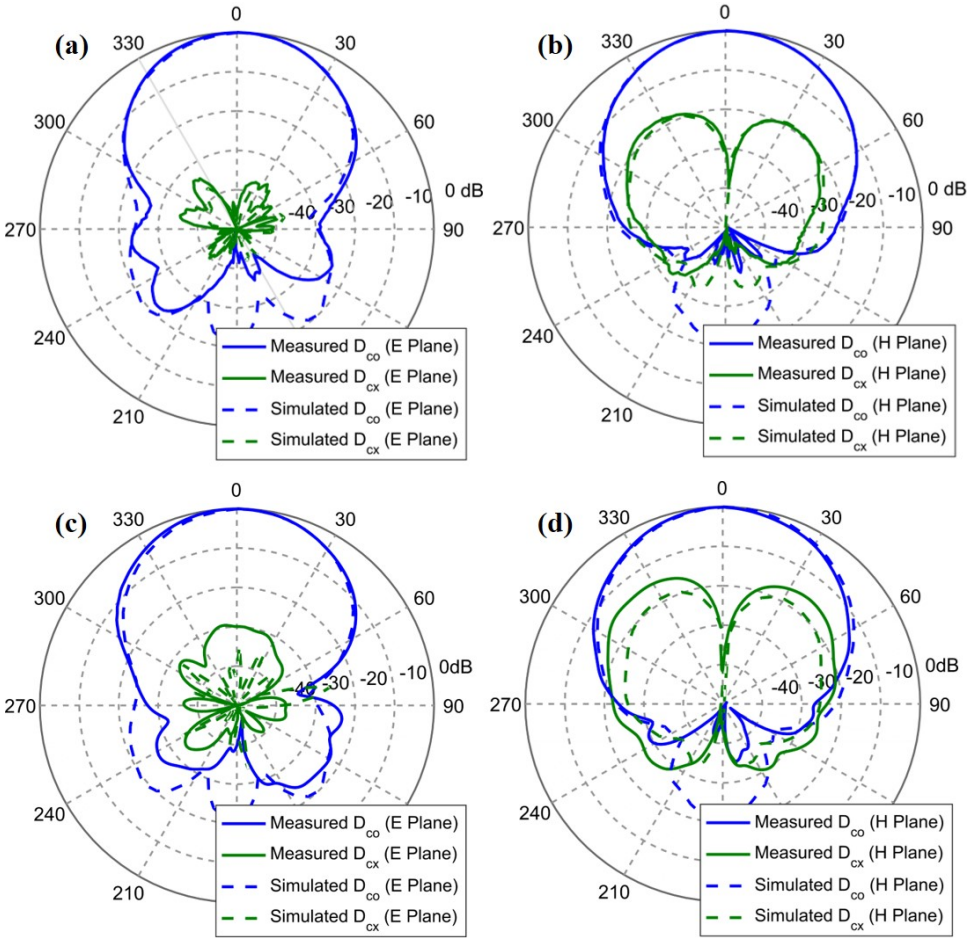

Figure 5.9: The measured radiation pattern for embroidery patch antennas with low stitch density in (a) and (b), and high stitch density in (c) and (d).

The radiation pattern of the embroidery patch antennas with low and high stitch densities are measured in the UCLA spherical near-field chamber. The results shown in Fig. 5.9 demonstrate good agreement between simulations and measurements for both co-pol and cross-pol radiations for antennas embroidered with low and high stitch densities.

Fig. 5.10 illustrates the few cases with stitch density below 1000 lines/m (10 lines/cm). The lower limit of stitch density has been found as 1000 lines/m (10 lines/cm), below which the ripples in S_{11} starts to appear, indicating unexpected reactive coupling mechanisms. The backside of the patch plays an important role to ensure that the good S_{11} performance is preserved. When the lines in the direction of low conductivity begins to be separated, the ripple appears due to reactive coupling between adjacent lines.

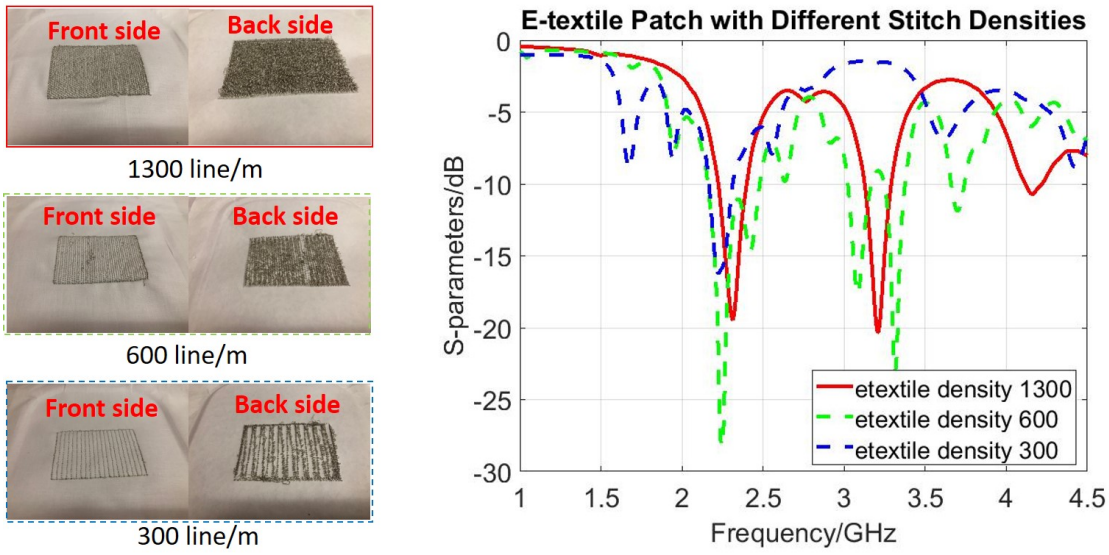

Figure 5.10: The lower limit of stitch density has been found as 1000 lines/m (10 lines/cm), below which the ripples in S_{11} starts to appear, indicating unexpected reactive coupling mechanisms.

A generalized lumped element circuit model can be utilized to study the effect of stitch density for embroidery patch antenna. With the multi-resonance circuit model linked with particle swarm optimization (PSO), the accurate Z parameter and S parameter over a wide frequency spectrum can be reconstructed with only a limited number of simulated frequency points required. A similar approach has been used to study the rectangular patch antenna bending effects as reported in [98]. The general expression for the input impedance of the

Table 5.2: The circuit model parameters for patch antennas using copper and embroidery patterns with different stitch densities.

Circuit Parameters	Density Study Cases			Circuit Parameters	Density Study Cases		
	High	Low	Copper		High	Low	Copper
C_0(pF)	21.12	23.04	43.50	L_5(nH)	0.566	0.697	0.007
$R_1(\Omega)$	171.46	289.65	437.26	$R_2(\Omega)$	114.14	188.11	451. 81
C_1(pF)	3.674	2.353	2.304	C_2(pF)	3.104	3.051	2.066
L_1(nH)	1.840	2.611	2.667	L_2(nH)	1.073	1.085	1.474

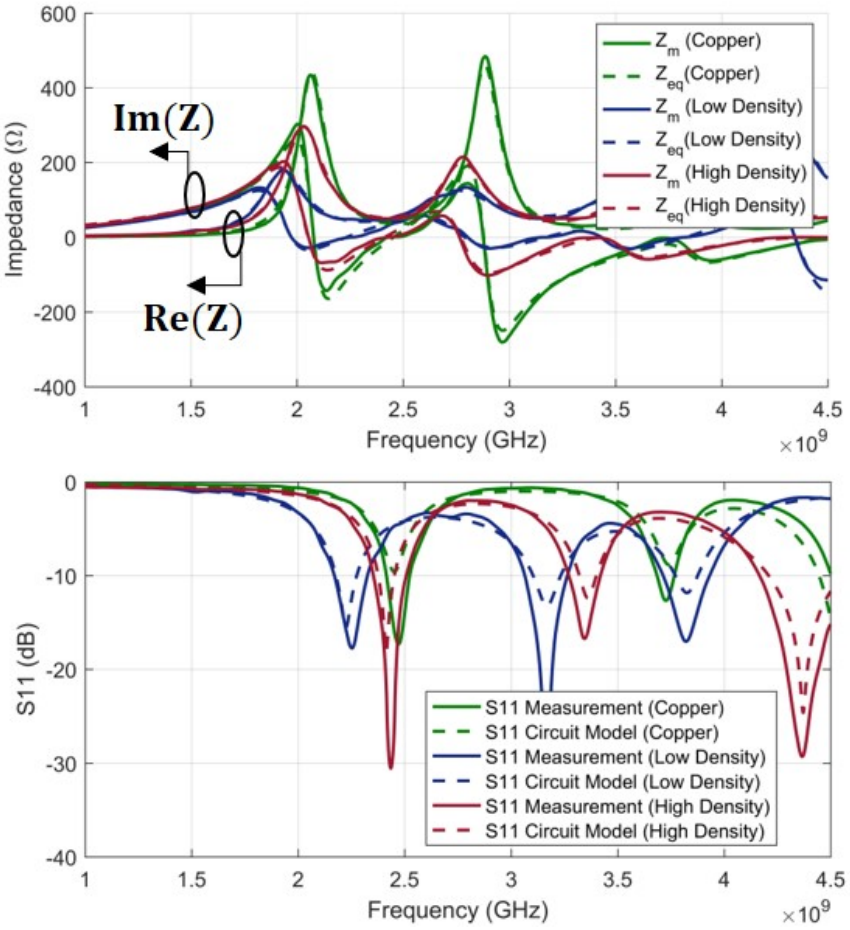

Figure 5.11: The input impedance and S_{11} from the optimized circuit parameters comparing with the simulation results for the 3 cases with copper, high density and low density embroidery patterns.

equivalent circuit written as [98]:

$$Z_{eq} = j2\pi f L_5 + \frac{1}{j2\pi f C_0} + \sum_{i=1}^{M}(\frac{1}{R_i} + \frac{1}{j2\pi f L_i} + j2\pi f C_i)^{-1} \tag{5.2}$$

where M denotes the number of resonances in the frequency band of interest, R_i, C_i, L_i are the equivalent lumped resistance, capacitance and inductance for the ith number of resonant mode. 3 cases have been studied for copper, high density (3750 line/m) and low density (1250 line/m) embroidery patterns. A normalized error function has been defined as the fitness function. By minimizing the fitness function, PSO finds the best parameters for the equivalent circuit model which generates the impedance curve closest to the measured results

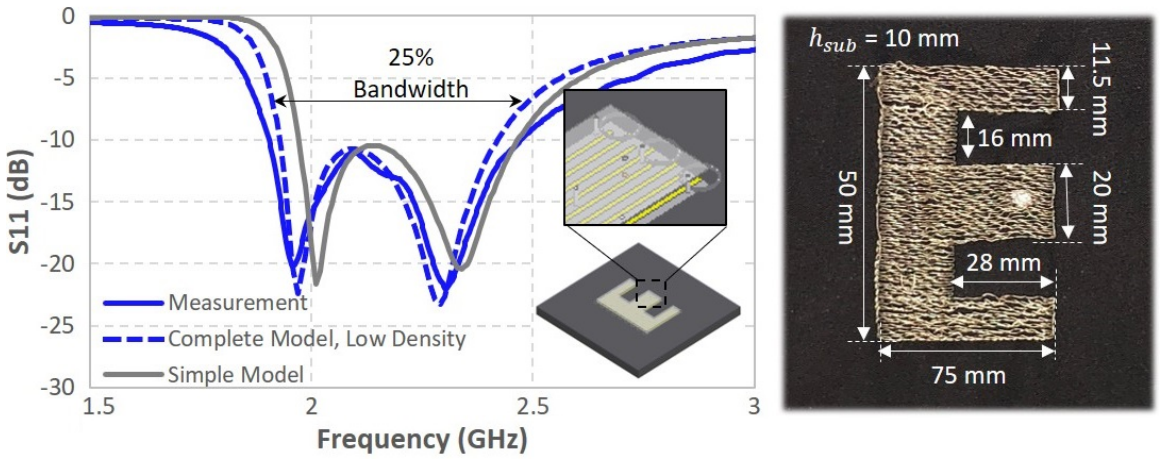

Figure 5.12: An E-shaped embroidery patch antenna with low stitch density is built and measured to validate the stitch density study.

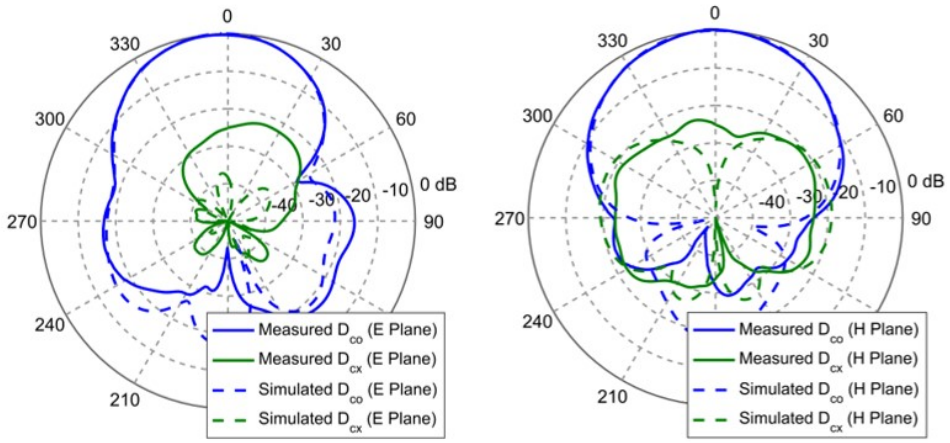

Figure 5.13: The measured radiation pattern for embroidery E shaped patch antennas with low stitch density.

for each case.

Table 5.2 lists the optimized circuit parameters for patch antennas using copper and embroidery patterns with different stitch densities. It is observed that comparing to copper, the embroidery patch antenna gives an increasing C_1 and decreasing L_1. The LC product increases, which results in a decreased resonant frequency. Comparing to the high-density, the low-density case has smaller variation to the case using copper as conductive material. Low density patch antenna performance is more similar to copper patch antenna. The major

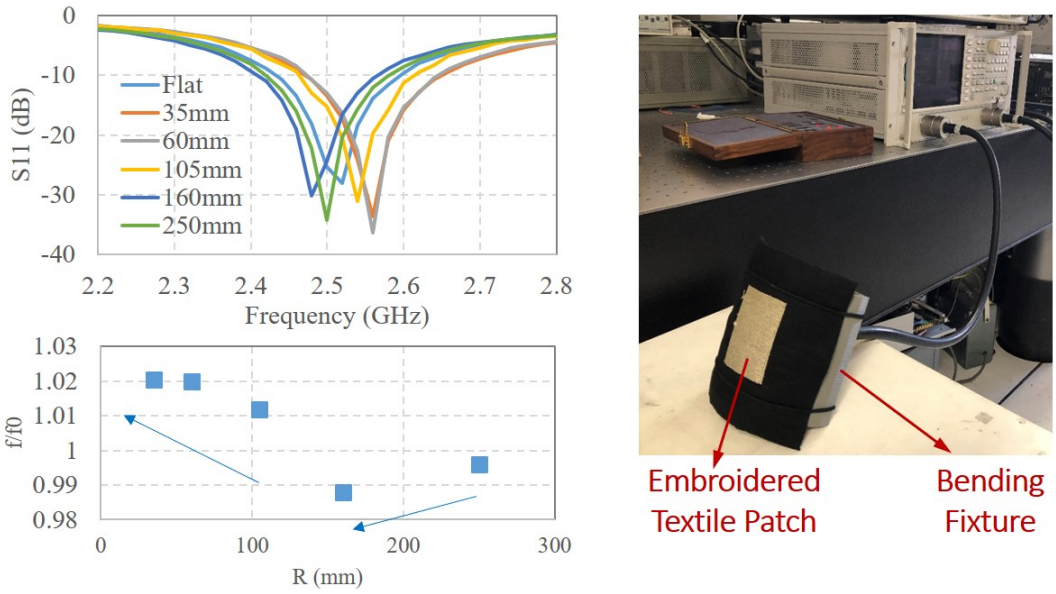

Figure 5.14: The measured radiation pattern for embroidery E shaped patch antennas with low stitch density.

reason is that the high density patch antenna has more complicated structure on the back than the low density ones.

As the final step of the study, an E-shaped patch antenna with low stitch density is built and tested to validate the modeling strategies and stitch density study. As shown in Fig. 5.12, the detailed full-wave modeling strategy with parameters listed in Table. 5.1 are used to generate the simulated S_{11} results and compared to measurements. The simulations with detailed modeling shows better agreement to measurement than the result for simple model.

5.4 Summary

This chapter presents the methodology of material characterization and detail modeling towards the accurate simulation of embroidery-based patch antennas. It is shown that these modeling strategies are effective in predicting the resonance and radiation properties of the prototyped embroidery patch antenna.

To conclude this chapter, surface bending measurements are conducted, by bending the

high density embroidered patch antenna onto 3D printed cylindrical bending fixtures with pre-defined bending radii. As illustrated in Fig. 5.14, we observe frequency down shift for large bending radius (300 mm, 160 mm), and up shift for small bending radius (105 mm, 60 mm, 35 mm). The frequency shift is within 3% with respect to the center frequency at flat condition. The patch antenna bending effect will be discussed in depth in the following chapter.

CHAPTER 6

Patch Antenna Bending Effects for Wearable Applications

Recent advances in the field of wearable technology have fostered an increasing need for the development of reliable and robust wearable antennas [99]. Generally, there are two major challenges in designing wearable antennas [100]. First, the proximity of lossy human tissue results in a reduction of antenna efficiency and limits the maximum transmit power due to heating concerns. Secondly, the bending effects degrade the performance of antennas compared to their flat condition. And even if the antenna is designed for a certain bending radius, the inter-person bending variation can be significant in determining the antenna performance.

Several articles focusing on wearable antennas have been published in the development of wireless body area networks (BANs) [101] and other various applications including spacesuits [102] and telemedicine [103]. Many of them target a specific antenna design for a given application, and the antenna bending effects are examined by simulation or measurement for fixed bending conditions. In [104] and [105] the authors discussed how the performance of wearable patch antenna is affected by bending. Two bending radii along two principle planes have been applied in the resonant frequency, bandwidth and radiation pattern measurement for three different patch antennas (conventional patch, electromagnetic band gap (EBG), and U-slot antennas). In [106] and [107], the bending effect of a textile planar inverted-F antenna (PIFA) under three bending radii and three crumping conditions has been investigated. The resonant frequencies and radiation patterns have been investigated based on numerical and experimental methods, and results yielded significantly degraded antenna performance.

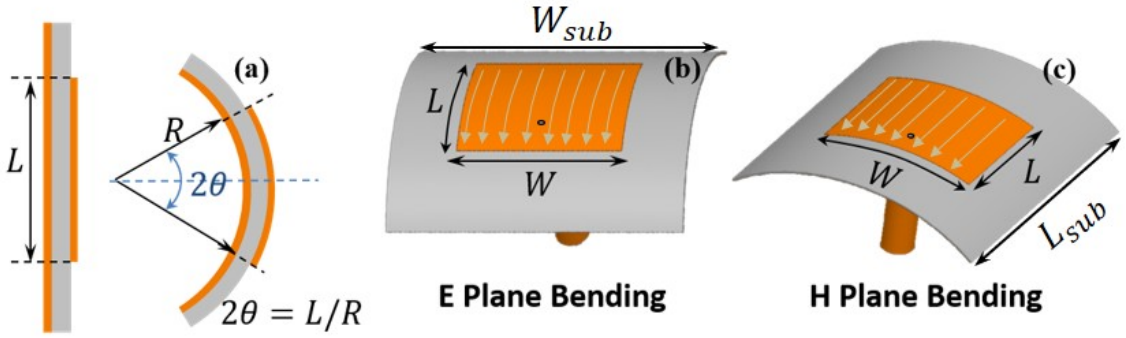

Figure 6.1: Characterization of rectangular patch antenna bending effects. (a) The illustration of bending angle 2θ and bending radius R (for the limiting case of flat condition, the bending angle $2\theta = 0°$ and the bending radius $R = \infty$). The E plane bending and H plane bending cases are shown in (b) and (c), respectively. The patch dimensions L and W are kept constant as 2θ and R are varied throughout the study.

The bending effects of other types of antenna have also been discussed as supporting study for designs targeting wearable application, including polymer coated wire antenna [108], inkjet-printed series-fed two-dipole antenna [109], textile monopole array antenna [100] and circular patch antenna [110]. Some publications specifically focusing on the antenna bending effects are also available. In [111] the authors focused on back radiation reduction when antenna was placed on a bent surface. In [112] and [113], the polynomial chaos theory was combined with simulation for curved textile antennas to statistically predict the variation and uncertainty in the antenna's resonance frequency under random bending conditions. A cylindrical-rectangular cavity model for bent patch antenna has been proposed in [114] and [115]. However, no measurement result has been presented for comparison.

In this work, a systematic and comprehensive investigation of the bending effects of wearable rectangular patch antennas is presented. In Section II, we present the resonant frequency and radiation pattern variations due to bending in two principle planes by simulating patch antennas in a full-wave model. A frequency shift plot with respect to bending radius has been generated to target antennas for various wearable applications. It has been demonstrated that the bending angle vs. normalized frequency shift is a universal criterion that remains consistent over frequency scaling, and is thus suitable for comparing the bend-

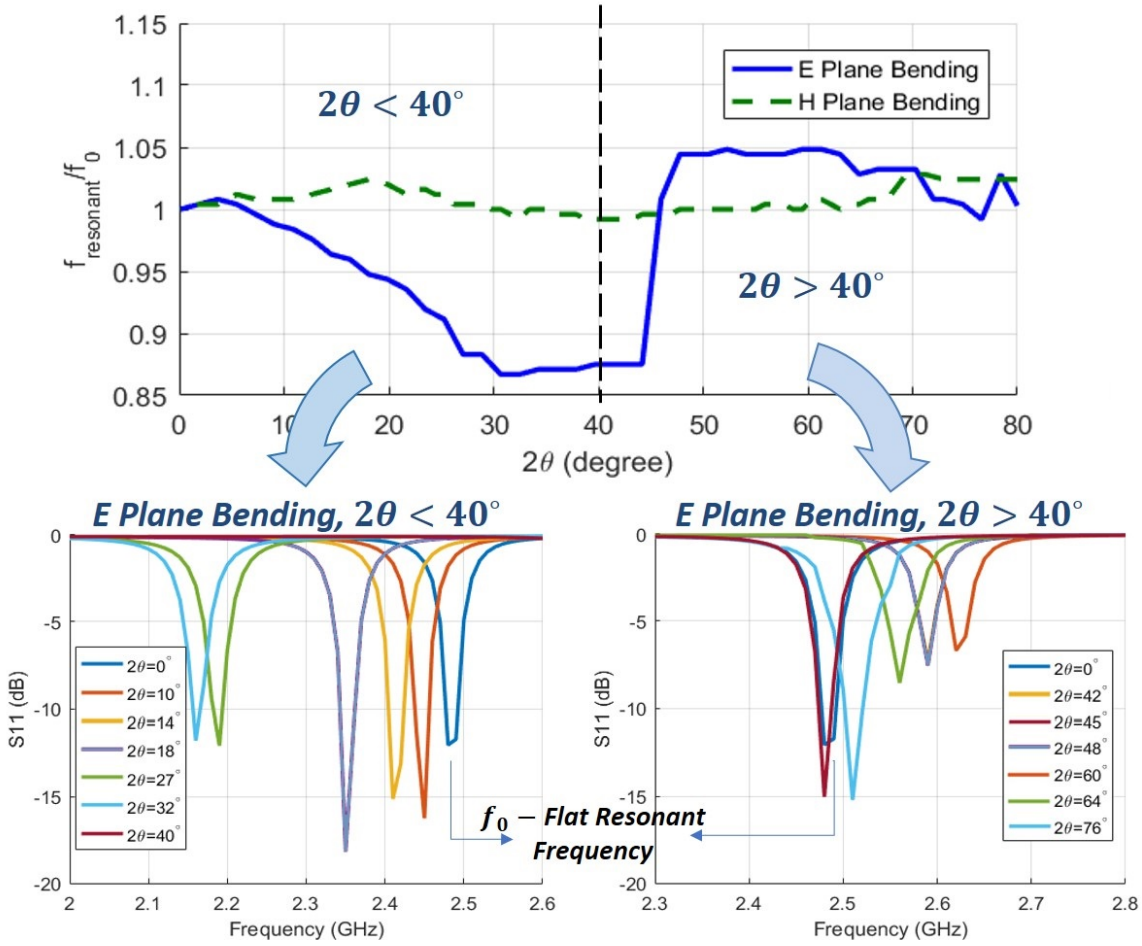

Figure 6.2: Frequency variations of the bending effects on both E and H planes. (a) The normalized frequency shift is plotted with respect to bending angles for the rectangular patch antennas. The E plane frequency shift due to bending splits into two regions, with left shift on slightly bent region ($2\theta < 40°$), and right shift on severely bent region ($2\theta > 40°$).

ing robustness among various types of antennas. In Section III, an analytical approach has been used to study the effect of resonant frequency shifting for both E plane and H plane bending. An equivalent lumped element circuit model has been developed to study E plane bending in Section IV. The analytical model and circuit model approaches provide physical insights on the complex mechanism of bending effects, and also offer the advantage of using only limited computation resources to calculate the effects of bending. Finally, measurement results using 3D printed bending fixture is discussed and compared with simulations in Section V. One of the main objectives of this work is to generate useful design curves to help

antenna engineers to incorporate the effects of bending more efficiently for various wearable applications.

6.1 Modeling of Patch Antenna Bending

In general, the effects of antenna bending could be considered by applying different approaches: (a) fixing the size of the patch antenna as it is in the flat condition and apply the bending without changing dimensions of the patch; (b) modifying the size of the patch for each of the bending conditions and retune the frequency shift to the flat resonant frequency; and (c) incorporating an adaptive concept, eg. reconfiguration mechanism, which allows the retuning of the patch antenna for each of the bending situations. In order to provide an insight into the significance of bending on the functionality of patch antennas, approach (a) has been applied in this study.

The antenna bending has been characterized by the bending angle, which is defined as the angle of arc formed by bending one dimension of the patch over a cylinder with radius of R, as illustrated in Fig. 6.1 (a). For a patch antenna with fixed dimensions, each bending angle θ uniquely corresponds to a bending radius R. An antenna model has been built in ANSYS high frequency structure simulator (HFSS), in which the bending angle is varied from 0° (flat) to 90° (severely curved).

The effects on material properties due to bending is important in analyzing electro-textile based antennas. However, throughout this chapter including simulations and analytical studies, we assume the stretch on patch and compression of substrate are negligible, the reasons are as follows: (a) Among the various conductive textile materials with different mechanical properties, many of them present much lower elasticity than traditional fabric such as cotton and polyester, due to the stronger property of the metal-hybrid yarns as well as increased woven density (in order to improve the surface conductivity). In [116], the electric and mechanical properties of high-performance woven electromagnetic shielding materials are presented, showing that under certain tensile strain, the electro-textile fiber used in woven conductive fabric has much lower elongation than the traditional polyester

fiber (1.29% vs. 57.57%). (b) The amount of compression and stretching on the substrate is related to the original substrate dimension, the bending radius R and substrate thickness h [117]. For a thin substrate with $h = 1$ mm, the compression or stretching of the substrate is only around 1% even for a small bending radius $R = 35$mm. Therefore, we believe that ignoring the substrate stretching or compression in the analysis of bending for thin substrate is a reasonable approximation.

A simple $\lambda/2$ (corresponding to wavelength in the substrate) rectangular patch antenna is studied at the frequency of $f = 2.49$ GHz, with the patch dimensions $L = 39.5$ mm (slightly smaller than $\lambda/2 = c/(2f\sqrt{\epsilon_r}) = 41$ mm due to the fringing field effect [118]) and $W = 50$ mm. The choice of patch dimensions provide the resonant length and reasonable impedance matching and bandwidth. The substrate of the patch antenna has been modeled with dimensions of $L_{sub} = W_{sub} = 100$mm, dielectric constant of $\epsilon_r = 2.1$ [119] and thickness of $h = 1$ mm, corresponding to the material properties of cotton substrate, which is typically considered for wearable antenna designs [81]. Two types of bending situations in the two principle planes are defined as E plane bending (bent along the length dimension) and H plane bending (bent along width dimension), as illustrated in Fig. 6.1 (b) and (c), respectively.

The one port reflection coefficient for various cases of bending are extracted from the full-wave simulation. Fig. 6.2 plots the resonant frequency shift when the antenna is bent by different angles 2θ along E and H planes. The bending angle is varied from 0° (flat case) to 90°, and resonant frequency f_{res} is normalized to the original resonant frequency in flat condition (f_0) and plotted for each case. By observing the E plane bending effect shown in Fig. 6.2 (a), we could see that the frequency shift phenomenon splits into two regions with respect to the bending angle θ. For bending angle $2\theta < 40°$ (slightly bent), the resonant frequency shifts to lower frequency (or shifts left), while for bending angle $2\theta > 40°$ (severely bent) the resonant frequency shifts to higher frequency (or shifts right), as shown in Fig. 6.2 (b) and (c), respectively. By comparing the bending effects for E and H plane, it also shown that E plane bending generates up to ±15% of normalized frequency shift, while the effect of H plane bending is less than ±4%. This could be explained by the fact that the E-plane bending affects the resonance path more significantly than the H-plane bending does,

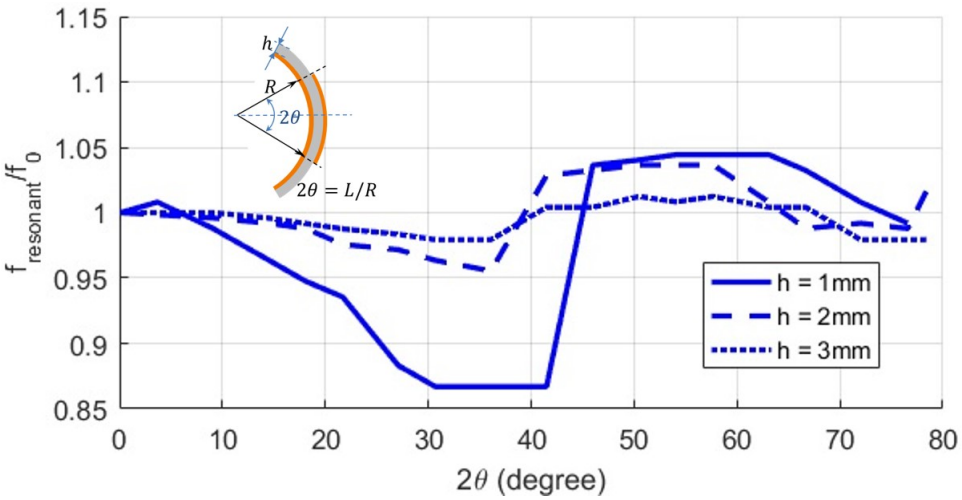

Figure 6.3: Simulated frequency shift with bending applied in E plane, for patch antenna with varied substrate thickness h.

particularly for the fundamental mode of resonance [105], as shown by the direction of the current plotted in Fig. 6.1 (b) and (c).

According to the frequency shift plot for E plane bending in Fig. 6.2, the critical bending angle of $2\theta = 40°$ could be identified, around which the transition from left-shift to right-shift occurs. To study the effect of substrate thickness h on the frequency shift and critical bending angle, patch antennas with the original dimensions (L and W) and varied thickness (h) are simulated, and results for the frequency shifts with E plane bending are plotted in Fig. 6.3. According to the simulation results, patch antennas with thicker substrate are less affected by the bending, with a normalized frequency shift of $\pm 5\%$ for the case of $h = 2$ mm and $\pm 2.5\%$ for the case of $h = 3$ mm. However, for all the three cases ($h = 1$ mm, 2 mm, 3 mm) we observe the frequency shift curves split into two regions, with the critical bending angle 2θ lying around 40°.

The effects of bending on radiation pattern are investigated in simulations as well. Fig. 6.4 shows the simulated E plane cut of the radiation pattern for the 2.49 GHz patch antenna configuration. For slight bending in E plane (Fig. 6.4 (a)) the co-pol radiation pattern (D_θ) is similar to that in flat condition, with the cross-pol (D_ϕ component) remained in a decent level. For the case with severe bending in E plane (Fig. 6.4 (b)) the co-pol radiation pattern

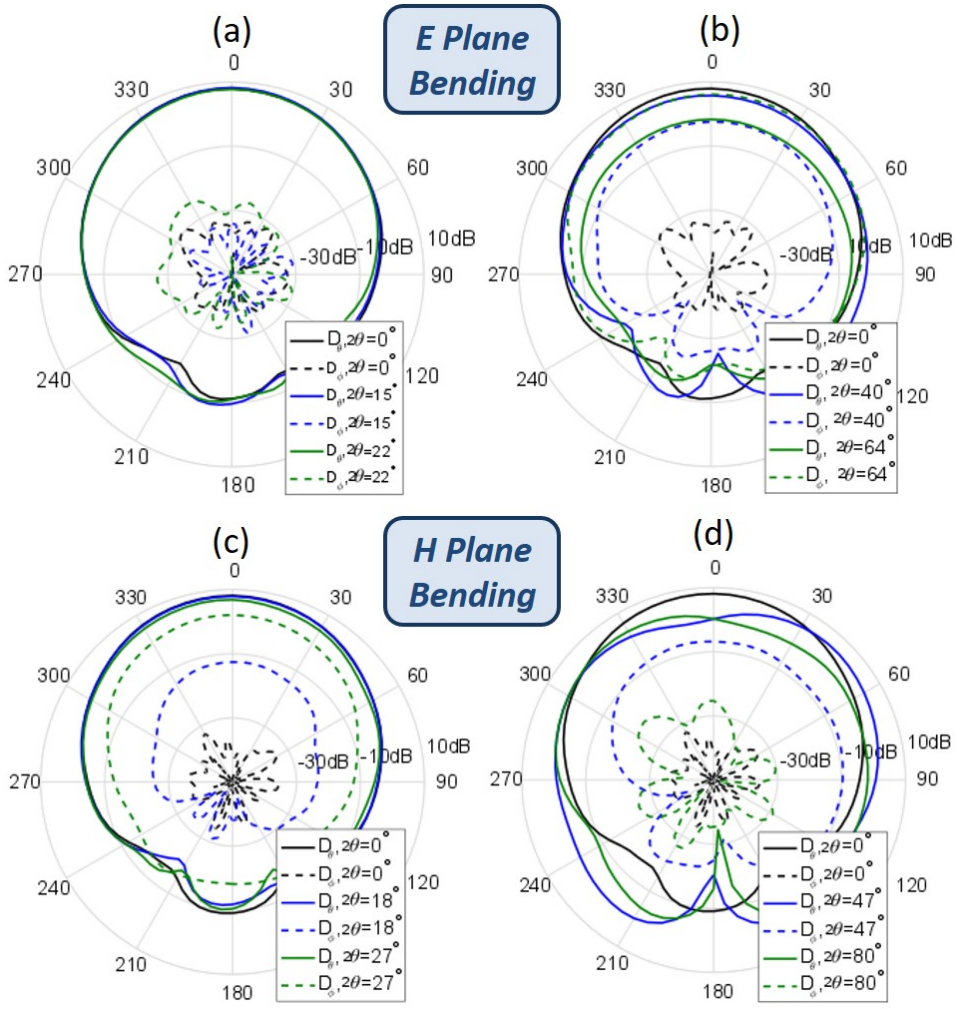

Figure 6.4: Radiation pattern variations with respect to bending angles for E plane bending in (a) and (b), and H plane bending in (c) and (d).

deviates from that in the flat condition and cross-pol increases significantly, resulting in poor resonance. For the case of H plane bending, as shown in Fig. 6.4 (c) and (d), although the resonant frequency is not significantly affected by bending in H plane, the radiation pattern is broadened at large bending angles ($2\theta = 47^\circ$ and $2\theta = 80^\circ$), and the cross-pol arises even at small bending angles ($2\theta = 18^\circ$ and $2\theta = 27^\circ$). We also observed a radiation efficiency degradation from 91.3% to 87.5% with 63° bending, for the patch antenna $h = 1$mm.

In order to study the effect of bending on patch antennas corresponding to different operating frequencies in their flat states, the original antenna topology with a flat-condition resonance at 2.49 GHz has been scaled in size to create another two patch antennas, with

the resonant length corresponding to a higher frequency band (L_{patch} = 18.9mm for f_0 =4.9 GHz) and a lower frequency band(L_{patch} = 79.5mm for f_0 = 1.25 GHz), respectively. W_{patch} and thickness h are scaled accordingly with the length dimension L_{patch}. The three different antennas with resonant frequencies at 1.25, 2.49 and 4.9 GHz are denoted as LF (low-frequency band), MF (middle-frequency band) and HF (high-frequency band), and target the following wireless communication spectrum:

1. High-frequency with f_r = 4.9 GHz targets the fixed and mobile services in support of public safety (4.940 GHz to 4.990 GHz);

2. Middle-frequency with f_r = 2.49 GHz targets the Bluetooth spectrum for personal communication and potential applications in body-area networks (BAN) (2.385 GHz to 2.490 GHz);

3. Low-frequency with f_r = 1.25 GHz targets the satellite application spectrum in support of space research and earth explorations (1.215 GHz to 1.300 GHz).

Fig. 6.5 plots the normalized resonant frequency with respect to the bending radius (to target various potential wearable applications), where the frequency shift for the antennas corresponding to three different flat-condition resonant frequency bands are separated from each other. Observation from Fig. 6.5 reveals that choosing smaller antenna with higher resonant frequency is in general an effective way to enhance antenna bending robustness (reduce the amount of normalized frequency shift) for rectangular patch antennas. This is especially true for applications that require severe bending, since the separation between curves in Fig. 6.5 increases as the bending radius R decreases.

As shown in Fig. 6.6, for the same bending angle, the normalized frequency shift occurs almost identically for the three antennas with size and flat resonant frequency scaled accordingly. It proves that the bending angle vs. normalized frequency shift is a universal criterion that if almost independent to size scaling, and is therefore suitable as a general standard for comparing the bending tolerances among various types of commonly used antennas.

In general, the proximity of lossy human tissue results in a reduction of antenna efficiency

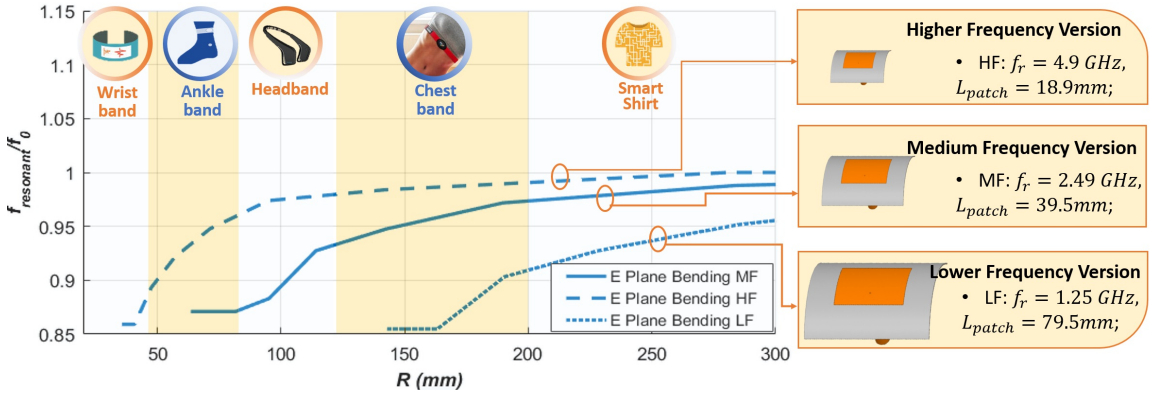

Figure 6.5: Normalized frequency shift (f_{res}/f_o) with respect to bending radius R, targeting at various potential wearable applications. The original antenna dimensions are scaled to generate a higher frequency and a lower frequency version.

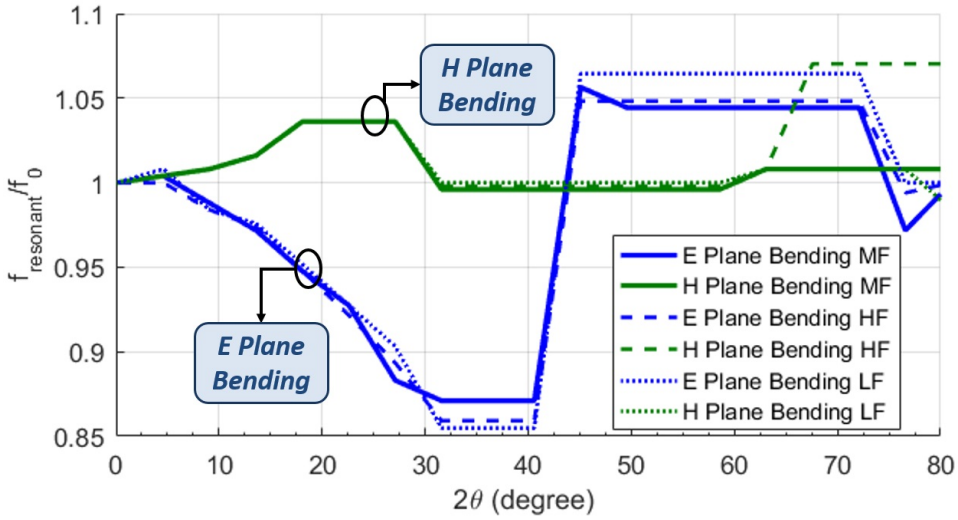

Figure 6.6: The normalized frequency shift (f_{res}/f_o) plotted with respect to the bending angle (2θ) for the three versions of rectangular patch antennas.

and affects the resonant characteristics. However, for patch antenna with ground plane, the effect of human tissue is not significant. As shown in Fig. 6.7, we simulate the patch antenna with cylindrical body phantom (averaged material properties are used $\epsilon_r = 50$, $\sigma = 1S/m$) [120]. E plane bending is applied with varying bending angle ($2\theta = 0°, 18°, 25°, 54°$, and $60°$). The simulated S_{11} has shown that the presence of lossy tissue for patch antenna with ground plane does not significantly affect the frequency shift due to antenna bending, with

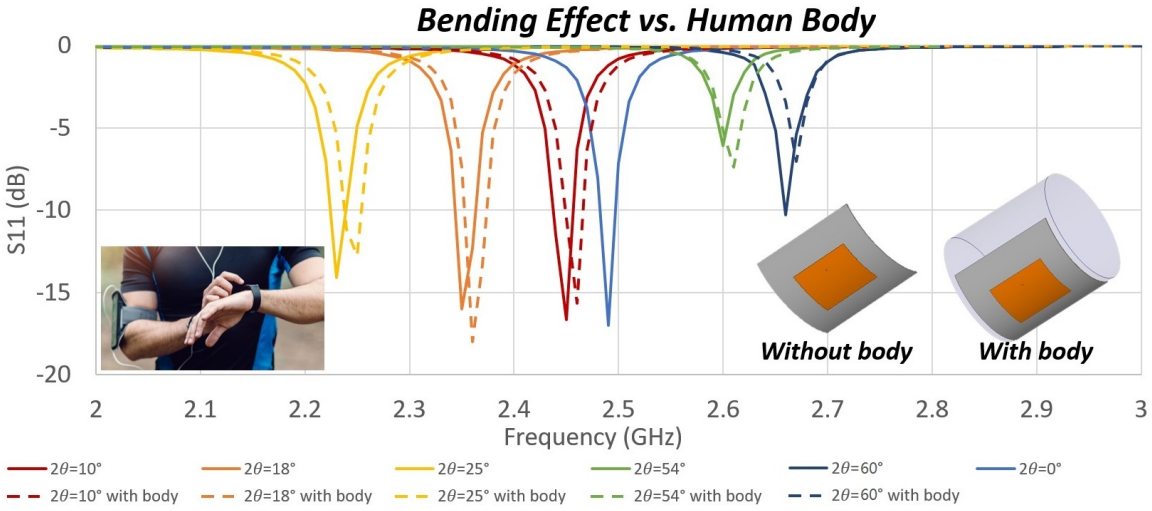

Figure 6.7: The simulated S_{11} for the E plane bent patch antenna with and without the cylindrical phantom lossy tissue.

the difference less than 0.8% compared to the cases without body tissue.

6.2 Analytical Approach for Patch Antenna Bending Effect: Cylindrical-Rectangular Cavity Model

Two major observations can be made from the simulation results as shown in Fig. 6.2: (a) the E plane bending affects the resonant frequency of patch antenna more significantly than H plane bending does; and (b) the frequency shift curve for E plane bending splits into two regions: down shift for bending angles $2\theta < 40°$ and up shift for bending angle $2\theta > 40°$. To have a better interpretation of the simulation results presented in Section 1, an analytical approach has been used in this section to study the effect of a patch antenna bending on a cylindrical surface. Similar to the rectangular cavity model approach for flat rectangular patch antennas, it provides physical insight on the complex mechanism of cylindrical bending from a cavity model point of view, and also offers the advantage of using only small computational resource for calculating the effects of patch antenna bending comparing to full-wave simulations.

The geometry of the bent rectangular patch antenna is modeled by a cylindrical-rectangular

cavity, and the eigenfrequencies corresponding to different bending angles for the transverse electric (TEz) and transverse magnetic (TMz) modes are solved from the vector potentials through Helmholtz equations. The shift of resonant frequency given by the analytical solution explains the intrinsic change of the eigenfrequencies due to deformation of the cavity structure.

The sideview of the cylindrical-rectangular model for the bent patch antenna is plotted in a cylindrical coordinate system, as shown in Fig. 6.8 (a). The cylindrical surface that the patch is bent on is oriented along z axis. The patch and ground are modeled as perfect electric conductor (PEC) surfaces, which gives two electric walls. The four side faces are modeled as magnetic walls, assuming the electric field drops perpendicularly along the edges from the conducting patch to the ground surface. Thus, the region between the patch and the cylindrical ground surface is considered as a cylindrical-rectangular cavity with two electric walls bounded on top and bottom, and four magnetic walls bounded on the sides. This is a similar approach that has been used in [121] and [122]. The electric field and magnetic field can be solved from the electric vector potential $\vec{F}$ and magnetic vector potential $\vec{A}$, which satisfy the Helmholtz equation. The resonant frequency can be found for each of the mode TE_{mli} or TM_{mli} as:

$$f_{r,mli} = \frac{1}{2\pi\sqrt{\epsilon\mu}}\sqrt{k_{mi}^2 + (\frac{l\pi}{2b})^2} \tag{6.1}$$

where the k_{mi} is solved through (6.2) and (6.3) for TEz modes (E plane bending) and TMz modes (H plane bending), respectively:

$$J'_\nu(k_{mi}a)Y'_\nu(k_{mi}(a+h)) - J'_\nu(k_{mi}(a+h))Y'_\nu(k_{mi}a) = 0 \tag{6.2}$$

$$J_\nu(k_{mi}a)Y_\nu(k_{mi}(a+h)) - J_\nu(k_{mi}(a+h))Y_\nu(k_{mi}a) = 0 \tag{6.3}$$

where J_ν and Y_ν are the Bessel functions of the first and second kind, in which $\nu = m\pi/2\theta$ is the order of Bessel function. The prime in (6.2) represents the derivative with respect to the whole argument of the Bessel functions. Dimensions of a and b are illustrated in Fig. 6.8 (b) and (c) for E plane and H plane bending. L and W are the length and width of the patch, and h is the thickness of the substrate. Note that through the study in this section, the dimensions of the patch antenna are fixed as $L = 39.5$ mm, $W = 50$ mm, $h = 1$ mm, while

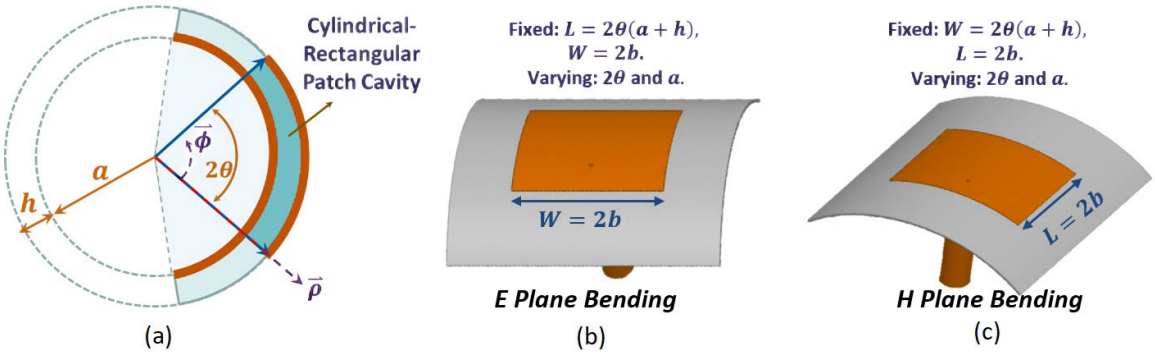

Figure 6.8: The cylindrical-rectangular cavity model for patch antenna bent on cylindrical surface. (a) Side view of the cavity model, fixed and varying parameters for E plane bending (b) and H plane bending, respectively.

the bending angle 2θ and inner bending radius a are varied to represent different bending levels. The detailed steps for (6.2) and (6.3) are provided in the Appendix.

To further verify the results given by the analytical approach, two simplified bent cavity models has been built in HFSS eigenmode solver. Model 1 is assigned with four PMC boundaries on the side walls and two PEC boundaries on the top and bottom surfaces. Model 2 is assigned with PMC on side walls and conductor boundaries on top and bottom (with the loss of copper). The eigenmode simulation results are shown as the green marks (triangular shape) in Fig. 6.9 (a) and (b) for E plane bending and H plane bending, respectively.

For the case of E plane bending shown in Fig. 6.9 (a), the HFSS eigenmode solution agrees well with the analytical calculation. The eigenfrequency cavity model predicts resonant frequency decrease with increase bending, which agrees with the simulation result for small bending ($2\theta < 40°$). For large bending, the full-wave simulation predicts the resonance shifting to higher frequency, which deviates from the trend shown by the TE_{101} eigenfrequencies (green solid line). However, a similar frequency shift is observed in the results for TE_{201} eigenfrequencies (green dashed line). This could be resulted by higher mode excitation due to the variation of input impedance of the rectangular patch as the bending angle increased to $2\theta > 40°$.

For H plane bending shown in Fig. 6.9 (b), the cylindrical-rectangular cavity model

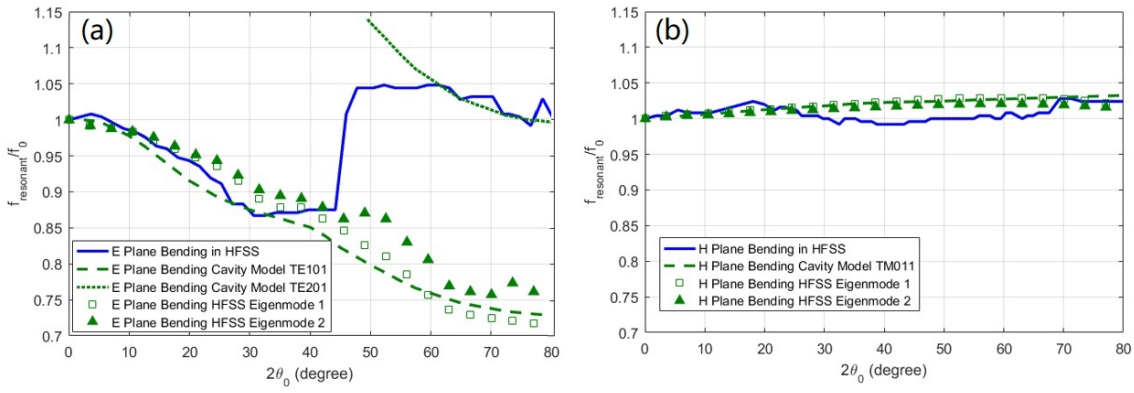

Figure 6.9: The frequency shift plotted respect to bending angle by cylindrical-rectangular cavity calculation (green lines), HFSS eigenmode simulation (green marks), and HFSS full-wave simulation (blue lines) for E plane bending (a) and H plane bending (b), respectively.

and HFSS eigenmode solution have very good agreement, and together with the full-wave simulation, predicts that the resonance frequency for rectangular patch antenna is not very much affected by bending in H plane. This could be due to the fact that H plane bending does not affect the current path for the fundamental resonance. Also inspection of equation (6.3) for the fundamental TM_{011} $(m = 0, l = 1, i = 1)$ mode shows that the order of Bessel function $\nu = m\pi/2\theta = 0$ for any bending angle 2θ, and therefore the solution of eigenfrequency is not as much influenced by the varying bending angle compared to E plane bending.

For the limiting case of flat condition, the bending angle $2\theta = 0°$ and bending radius $a \to \infty$. For E plane bending, the TE_{101} eigenfrequency recovers the flat resonant frequency with:

$$k_{mi} = \frac{m\pi}{2\theta a}, \quad f_{r,mli} = \frac{1}{2\pi\sqrt{\epsilon\mu}}\sqrt{(\frac{m\pi}{2\theta a})^2} \tag{6.4}$$

which satisfies (6.2) as the order of Bessel function ν goes to a very large number. Similarly, it could be easily proved that the TM_{011} eigenfrequency also recovers the flat resonance with:

$$k_{mi} = 0, \quad f_{r,mli} = \frac{1}{2\pi\sqrt{\epsilon\mu}}\sqrt{(\frac{l\pi}{2b})^2} \tag{6.5}$$

which satisfies (6.3) as $\nu = 0$.

6.3 Circuit Model Interpretation

In this section, a generalized lumped element circuit model has been utilized to study the effect of bending for patch antenna. The lumped circuit parameters for different modes of resonance are studied for different bending states, and the shift of resonant frequency is related to the variations of the lumped circuit parameters. Also, with the multi-resonance circuit model linked with particle swarm optimization (PSO), the accurate Z parameter and S parameter over a wide frequency spectrum can be reconstructed with only a limited number of simulated frequency points required. This, comparing with the wideband frequency sweep in full-wave simulation, could significantly reduce the simulation time.

This circuit model topology has been used to study the rectangular and E-shaped patch antennas as reported in [123]. As shown in Fig. 6.10, the orthogonal modes of resonance are modeled as the series connection of parallel resonant sections. The behavior of the feed point impedance of the antenna at the higher and lower edges of the frequency band of interest has been modeled by a high-frequency inductor L_5 and a low-frequency capacitor C_0. Based on the topology in Fig. 6.10, we have the general expression for the input impedance of the equivalent circuit written as:

$$Z_{eq} = j2\pi f L_5 + \frac{1}{j2\pi f C_0} + \sum_{i=1}^{M}(\frac{1}{R_i} + \frac{1}{j2\pi f L_i} + j2\pi f C_i)^{-1} \tag{6.6}$$

where M denotes the number of resonances in the frequency band of interest, R_i, C_i, L_i are the equivalent lumped resistance, capacitance and inductance for the ith number of resonant mode. In this study, we choose $M = 3$ and neglect the influence of higher order modes, since we are more interested in the frequency range where the first resonance is dominated.

The parameters of the equivalent circuit are determined by the particle swarm optimization (PSO), which has been shown to be effective in optimizing multidimensional problems [36]. A normalized error function has been defined as the fitness:

$$\frac{1}{Z_0}(\frac{1}{N}\sum_{k=1}^{N}\{\mathrm{Re}[Z_s(f_k) - Z_{eq}(f_k)]^2 + \mathrm{Im}[Z_s(f_k) - Z_{eq}(f_k)]^2\})^{\frac{1}{2}} \tag{6.7}$$

where Z_0 is the characteristic impedance of 50Ω, N is the number of frequency sampling, f_k is the frequency for the kth sample, Z_s and Z_{eq} are the simulated and equivalent input

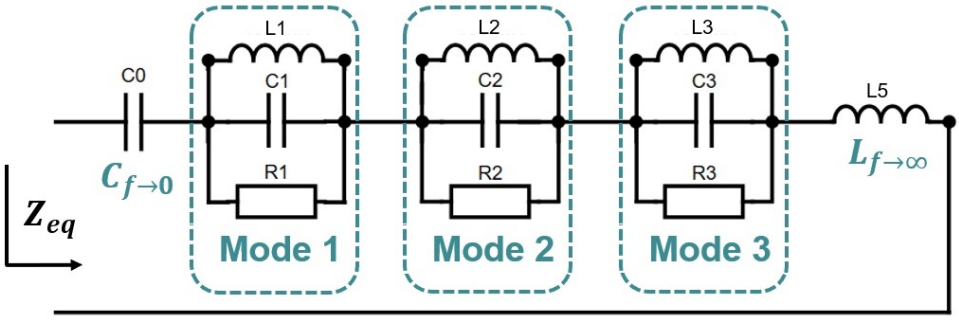

Figure 6.10: The general topology of the equivalent lumped element circuit of rectangular patch antennas. The patch antenna is modeled as the series connection of parallel resonant sections, with one low-frequency capacitor and one high-frequency inductor.

Table 6.1: The optimized circuit model parameters for patch antenna bent in E plane with $\theta = 0°$ (the flat case), $25°, 45°$ and $65°$.

Circuit Parameters	E Plane Bending Angle				Circuit Parameters	E Plane Bending Angle			
	0°	25°	45°	65°		0°	25°	45°	65°
C_0(pF)	16.10	15.79	16.27	17.10	L_5(nH)	0.943	0.901	0.975	0.950
$R_1(\Omega)$	71.35	102.01	72.95	51.79	$R_2(\Omega)$	105.11	98.20	89.78	88.51
C_1(pF)	56.04	39.78	53.55	78.52	C_2(pF)	21.65	20.71	21.81	20.83
L_1(nH)	0.074	0.153	0.076	0.049	L_2(nH)	0.076	0.097	0.080	0.079

impedance of the patch. By minimizing the fitness function, PSO finds the best parameters for the equivalent circuit model which generates the impedance curve closest to the simulation results over the frequency of interest. 45 particles are assigned in the 11-dimensional space to search for the best parameters within 2000 iterations. 4 cases have been studied for bending in E plane with $2\theta = 0°$ (the flat case), $25°, 45°$ and $65°$. Stable fitness values are obtained in the last few iterations, which indicates the convergence behavior of the swarm. The final parameters obtained by PSO give fitness values lower than -14 dB for all the four cases. The input impedance and S_{11} from the optimized circuit parameters demonstrate very good agreement with the simulations for the 4 cases with different bending angles, in a frequency range that starts from 1.5 GHz and includes the first 2 resonant modes, as shown in Fig. 6.11. The number of frequency samplings N used to generate the plots in Fig. 6.11 is 600,

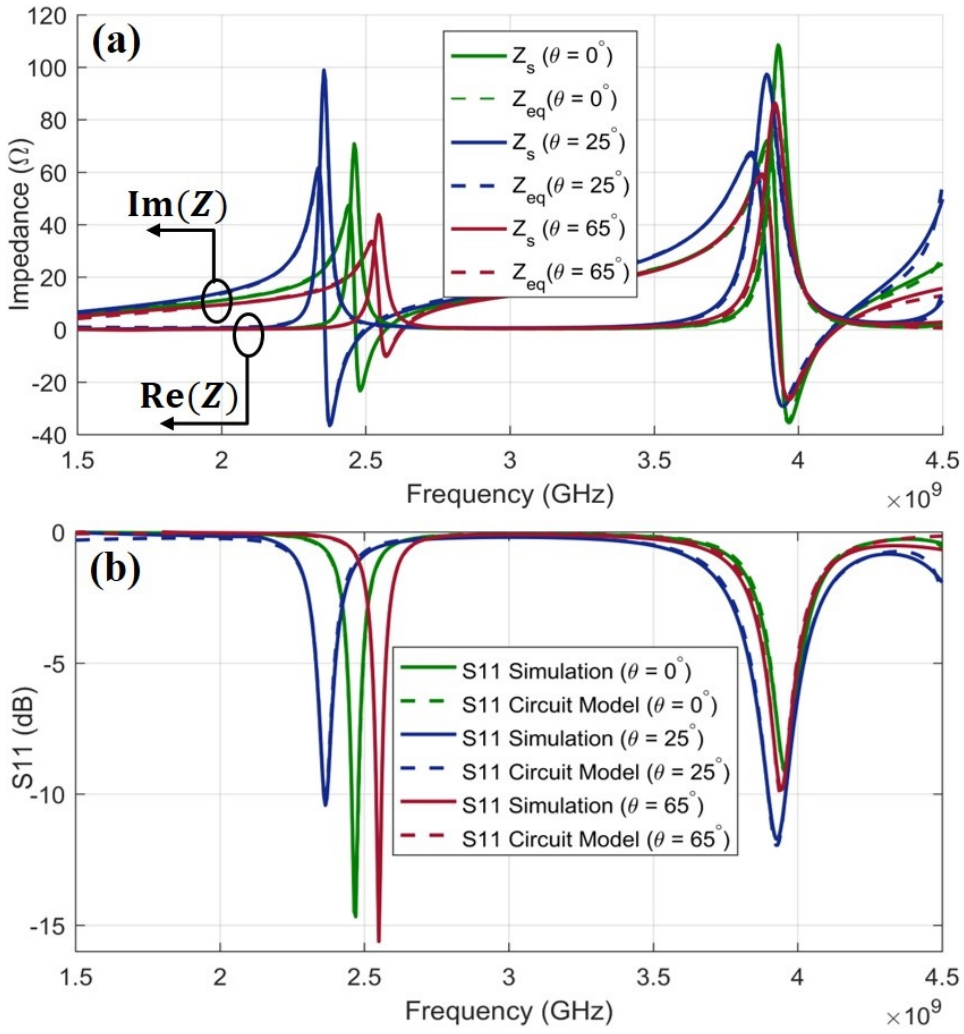

Figure 6.11: The input impedance and S_{11} from the optimized circuit parameters comparing with the simulation results for the 4 cases with $\theta = 0°$ (the flat case), $25°, 45°$ and $65°$.

and can be reduced down to 20 points without significant changes in the results.

Table 6.1 lists the optimized circuit parameters for patch antenna bent in E plane with bending angle $2\theta = 0°$ (the flat case), $25°, 45°$ and $65°$. It reveals that the low-frequency capacitor C_0, the high-frequency inductor L_5 are almost independent to the bending in E plane, and the parameters corresponding to the second resonance (R_2, C_2 and L_2) are not significantly affected as well (since the second resonance at the frequency around 4 GHz is related to the width dimension W, which is not strongly influenced by bending in E plane, as seen in Fig. 6.11). The parameters for M = 3 are not shown here for two reasons: (a) the M

= 3 parameters for the bending cases are not very much different from those for the flat case, and therefore, not too much information can be obtained with respect to bending analysis, and (b) the third mode of resonance is not included in the frequency range of 1.5 GHz to 4.5 GHz, and therefore we can hardly expect the parameters for M = 3 to represent the real situation very accurately. As expected from the simulation and analytical model, the effect of E plane bending on the first resonant mode (which is related to the length dimension L) has been observed by the circuit parameters R_1, C_1 and L_1. Comparing to the flat case with $2\theta = 0°$, at $2\theta = 25°$, the capacitance C_1 decreases and the inductance L_1 increases. The LC product increases, which results in a decreased resonant frequency. While at $2\theta = 65°$, C_1 increases and L_1 decreases. The LC product decreases, and a increased resonant frequency is observed. The lumped element circuit parameters from the circuit model study agree with the observations we have from the simulations (in Fig. 6.2).

6.4 Measurement and Comparison

The patch antenna prototype is built by attaching copper foil (0.03mm in thickness) with cotton substrate (1 mm in thickness) with liquid glue, as shown in Fig. 6.12. The edges and the center of the copper foil are glued to cotton to provide solid connection and bending flexibility. The dimension of the ground copper foil is 100 mm×100 mm. In general the ground plane of patch antenna should be only about 2-3 times the thickness larger than the dimensions of the patch, to maintain a decent front-to-back ratio [118]. S_{11} measurement for the patch antenna is performed for five bending angles, which correspond to the average bending radius for five potential applications, e.g. wrist band, ankle band, headband, waist band and smart cloth (as illustrated in Fig. 6.5), corresponding to bending radius R = 35 mm, 60 mm, 105 mm, 160 mm, 250 mm. To maintain the accurate and stable bending radius, 3D-printed bending brackets with cylindrical surface with the five different radius in polylactide (PLA) material have been built to provide the curved surface in the bending effect measurement, as shown in Fig. 6.13. In the actual applications, different feeding mechanism (aperture-coupling or side-mounting) could be used to avoid the probe and optimize the

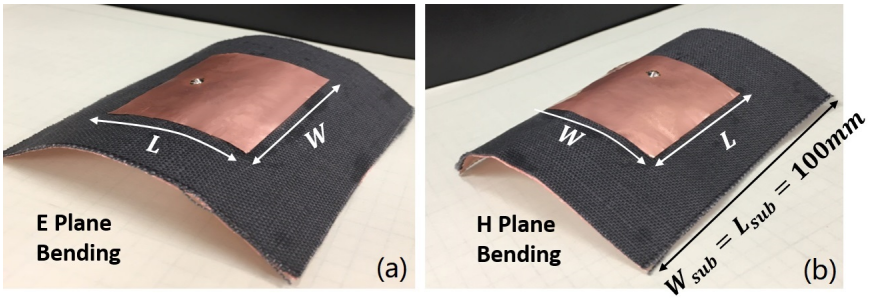

Figure 6.12: Patch antenna prototype bent in E plane (a) and H plane (b). The prototype antenna is made by cotton substrate and copper foil.

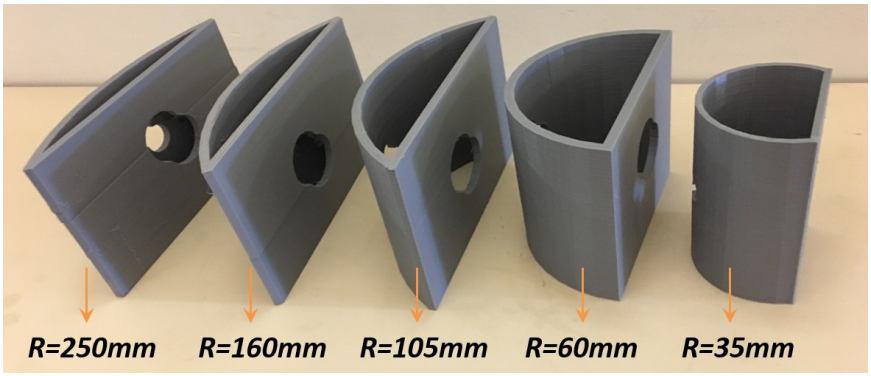

Figure 6.13: 3D-printed bending fixtures in PLA are built to provide the curved surface during the measurement.

comfort of users [124]. It is also shown by simulations that the results and analysis presented in the work based on back-fed patch antennas can be extended to microstrip line-fed patch antennas.

We measured the resonant frequency and radiation performance of the bent patch antenna using network analyzers and the University of California, Los Angeles (UCLA) spherical near-field chamber (Fig. 6.14), respectively. The same S_{11} measurement is repeated three times in order to characterize measurement error. The average of the measured resonant frequencies are taken, with the error bar plotted as well. The measurement results demonstrate very good repeatability among the three rounds of measurements. As expected from the simulations, frequency measurement shows that the E plane bending resulted in a lower frequency shift for $2\theta < 40°$ and a higher frequency shift for $2\theta > 40°$, respectively, while the H plane

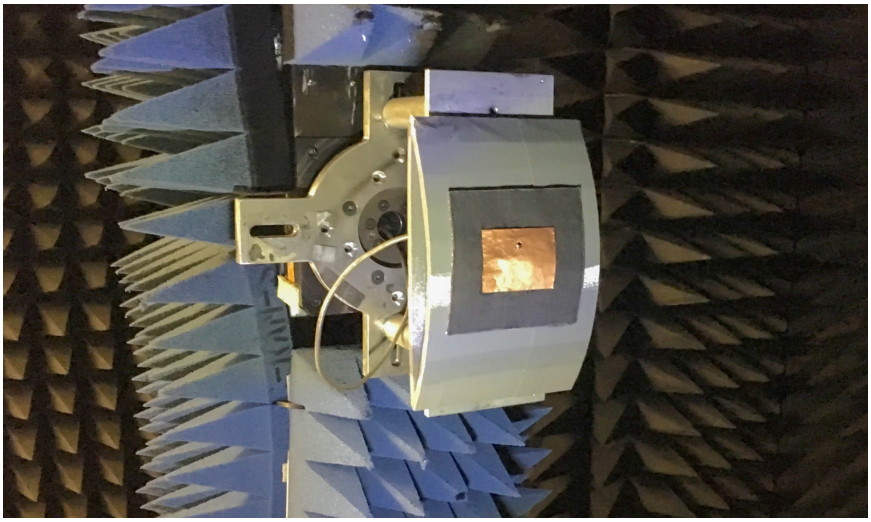

Figure 6.14: The patch antenna mounted with 3D-printed bending bracket (R = 160 mm) in the UCLA spherical near-field chamber. E plane bending is applied to the patch antenna.

bending only slightly affected the resonant frequency. Since the length and width of patch antenna are different (L = 39.5 mm and W = 50 mm), the bending angles corresponding to a fixed bending radius are different for E plane and H plane bending. The angles 2θ for each of the five radii of S_{11} measurement for E and H plane bending are listed in Fig. 6.15. The measured 10 dB S_{11} percentage bandwidth under different bending conditions are also listed in Fig. 6.15. It is observed that small bending angles in E plane slightly increase the impedance matching bandwidth. For large bending angles, the structure is changed remarkably, which results in impedance mistuning and decreased bandwidth. For H plane bending, the input-matching bandwidth stability is very good, with only a slight increase in bandwidth.

The radiation pattern measurement of patch antenna in E plane bending has been shown in Fig. 6.16 and compared with full-wave simulations. Four cases has been measured, in which the flat case and three different bending radii are applied (160 mm, 105 mm and 60 mm). The table in Fig. 6.16 lists the simulated and measured co-pol 3 dB beamwidth and cross-pol level in broadside for each of the bending cases. As expected from simulations, the measurement results proved that severe bending (R = 60 mm for this case) affects the radiation pattern by broadening the beam and increasing the cross-pol component. Based

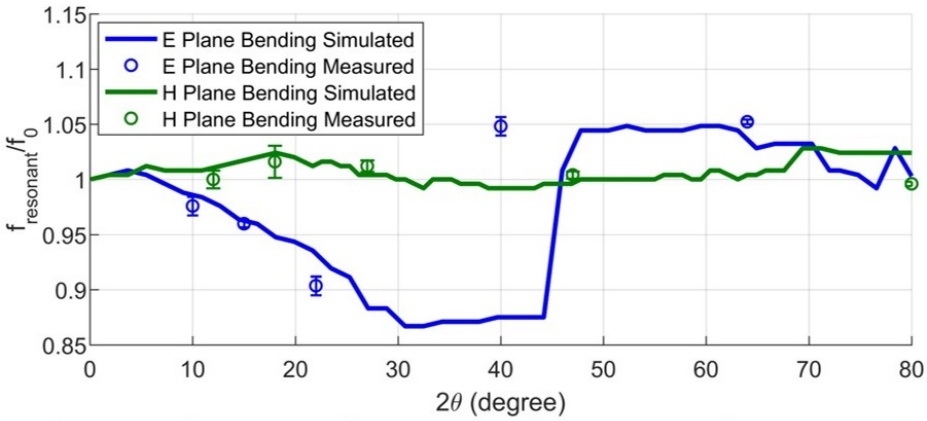

R (mm)	2θ (E Plane)	2θ (H Plane)	Bandwidth(E Plane)	Bandwidth (H Plane)
35	64°	80°	1.03%	1.26%
60	40°	47°	1.01%	1.25%
105	22°	27°	1.21%	1.29%
160	15°	18°	1.31%	1.27%
250	10°	12°	1.28%	1.27%
flat	0°	0°	1.25%	1.25%

Figure 6.15: The measured normalized frequency shift of the patch antenna prototype bent in E plane and H plane. The bending angles and measured 10 dB S_{11} bandwidth for each of the cases are listed in the table.

on the discussion in Section II, we believe that the results obtained in this study can be applied to most of the electro-textile materials with low elasticity and substrate with small thickness.

6.5 Summary

In this work, we investigate the bending effects of wearable rectangular patch antennas. A simple patch has been simulated in a full-wave bending model with varied bending angle 2θ from 0° (flat case) to 90°. We scaled the length and width of the original patch antenna for another two different frequency bands to study the effects of antenna size and the flat resonance frequency. Shifting of the resonant frequency for the fundamental mode and variations

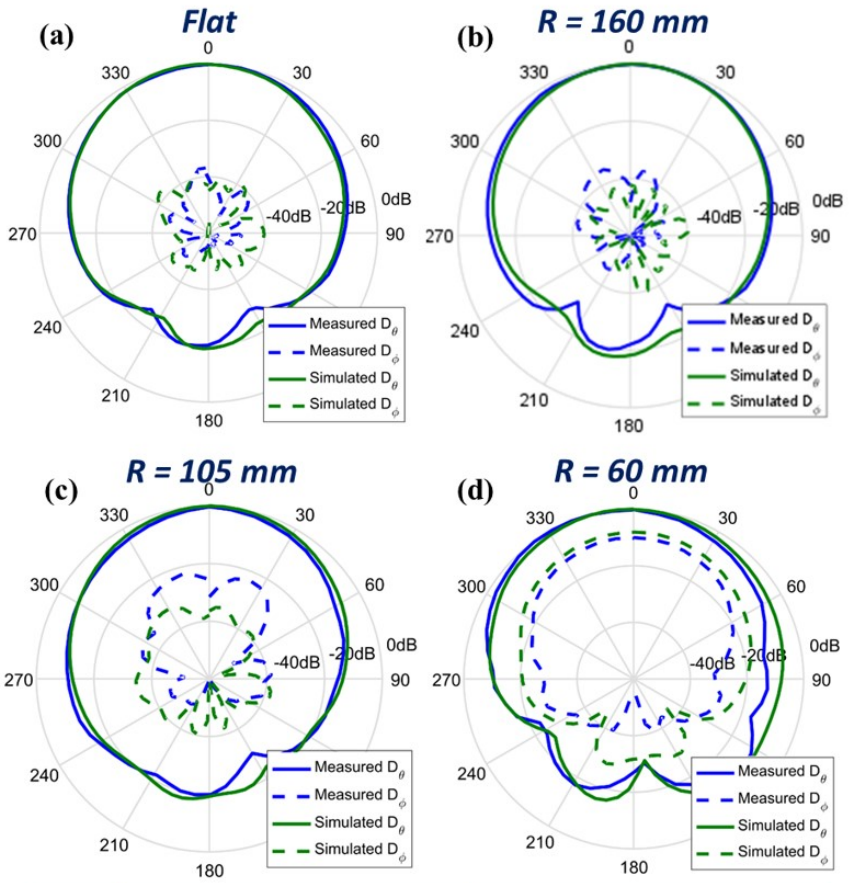

R (mm)	Simulation		Measurement	
	Beamwidth (3 dB)	Cross-pol (broadside)	Beamwidth (3 dB)	Cross-pol (broadside)
60	71	-11.1 dB	72	-9.7 dB
105	59	-31.5 dB	60	-39.6 dB
160	61	-41.7 dB	58	-42.3 dB
flat	56	-39.1 dB	55	-42.1 dB

Figure 6.16: Radiation pattern measurement results for patch antenna bent in E plane. The flat condition (a) and three different bending radius (b) to (d) has been applied by the bending brackets.

in radiation patterns are investigated. We have shown that the bending angle vs. normalized frequency shift is a suitable criterion for comparing the bending robustness among various antenna designs, since it remains consistent over frequency scaling. A normalized frequency shift plot with respect to the bending radius has been generated, which targets antennas for

various wearable applications, representing various parts of the human body. A cylindrical-rectangular cavity model has been used to physically interpret the simulation results for both E plane bending and H plane bending. The analytically calculated resonant frequency vs bending angle agrees well with the simulation and measurement results. A generalized circuit model has been characterized with the circuit parameters optimized by PSO. The circuit model gives very good agreement with simulations for the cases of E plane bending in different angles, which has brought additional insight into the understanding of the bending behaviors for patch antennas. Measurements has been conducted using 3D printed bracket, and measurement results are obtained with good agreement to simulations. Future works include comparison of bending robustness among various types of commonly used antennas candidates, generating simple formulas to estimate the potential bending effects for antenna performance degradations, and wearable antenna optimization incorporating bending analysis. One of the main goals of this study is to generate useful design curves and provide a better understanding of the effects of bending on antenna performance variation for wearable applications.

CHAPTER 7

Hybridizing Particle Swarm and Brain-Storm Optimizations in Electromagnetics

With the growing power of computing hardware and algorithms, the use of optimization has emerged as an essential tool in engineering designs. Utilization of optimization schemes has evolved as a popular strategy in solving complex electromagnetic problems, e.g. genetic algorithms (GA) [52], evolutionary programing [125], particle swarm optimization (PSO) [36], differential evolution [126], etc. In many electromagnetic problems, the fitness functions are non-differentiable, highly dimensional, nonlinear and discontinuous, which make the problem difficult for any optimization technique. Therefore, nature-inspired techniques have become popular in many research applications, especially electromagnetics. PSO is a nature-inspired global optimization algorithm that has been proven advantageous comparing to many other techniques because of its inherent simplicity and robustness in solving multidimensional engineering problems [36]. Brain-storm optimization (BSO) is a relatively new optimization algorithm that was recently introduced into electromagnetics applications [127]. It is a swarm intelligence optimization scheme inspired by the collective behavior of human beings in searching optimal idea for problem solving. The interested readers are encouraged to review [36] and [127] for many other relevant references on these topics.

Hybridizing two or more optimization algorithms to solve the same problem has also been explored in many literature, by either choosing one according to the assigned problem, or switching between them over the course of the optimization. This is generally implemented to combine desired features of each single algorithm, so that the overall hybrid optimization algorithm outperforms each of the individual components. In this chapter, we compare the performance of the two optimization algorithms in a benchmarking function with different

initializing conditions. We observe advantage of BSO in the speed of global exploration from a random initialization, and PSO in the accuracy of local exploitation with a predefined initialization. A hybrid of PSO and BSO is then investigated with an example of patch antenna circuit model determination. It is shown that the hybrid algorithm of PSO initialized with BSO could benefit from the advantages of both single algorithms, and therefore outperforms both PSO and BSO in finding minimum fitness within the same number of iterations.

7.1 Particle Swarm Optimization (PSO) and Brain-Storm Optimization (BSO)

In this section, we start with revisiting the concepts of nature-inspired optimization PSO and BSO. Since these algorithms are discussed throughout the chapter, we first establish the terminologies that describe certain aspects of the optimization problem:

- **Intrinsic Parameters**

  Parameters that are used by the optimization algorithm and characterize the algorithm's performance and convergence. This includes parameters that change throughout the iterations as well as those that remain constant.

- **Design Variables**

  These are the D variables that characterize the problem that is being evaluated and optimized (e.g. the physical dimensions of antenna, the circuit parameters in a circuit equivalence). Each set of values represents a possible solution, and we will be representing this with the design vector $\vec{x}$.

- **Design Boundaries**

  For bounded optimization techniques, one must provide the lower and upper bounds of each variable. These bounds are denoted by the $\vec{x}_{min}$ and $\vec{x}_{max}$ variables.

- **Design Constraints**

  For many optimization problems, constraints are required in order to abstain from

simulating physically unrealizable solutions. Constraints may also be given as part of a specification and therefore must be incorporated into the optimization algorithm.

- **Solution Space**

  The solution space is a D-dimensional hypercubic space defined by the boundary of each design variable. This is only applicable to bounded optimization techniques. For unbounded algorithms, the solution space is infinitely large.

- **Fitness Function**

  The fitness function defines the link between the design variables and the optimizer. This function maps the quality and performance into a single number which allows the optimizer to make decision on whether a given design is better than another.

PSO and BSO are both evolutionary global optimization techniques based on the movement and intelligence of swarms. Both of the two techniques start by assigning a number of agents (also referred as populations in BSO) into the defined solution space. The agents move through the solution space, evaluate their positions using the fitness function, and update their positions (also velocities in PSO) at the end of each iteration.

The major difference between PSO and BSO lies in the position updating schemes. In PSO, the positions are updated based on their movement over a discrete time interval (Δt) with Δt usually set to 1 [36]:

$$\vec{x_n}^{k+1} = \vec{x_n}^{k} + \vec{v_n}^{k+1}\Delta t \tag{7.1}$$

$$\vec{v_n}^{k+1} = w^k \vec{v_n}^{k} + c_1 r^k_{1,n}(\vec{p_n}^{k} - \vec{x_n}^{k}) + c_2 r^k_{2,n}(\vec{g_n}^{k} - \vec{x_n}^{k}) \tag{7.2}$$

where subscript n and superscript k denote the nth agent in the kth iteration. $\vec{v_n}^{k}$ is the velocity, w_k is the inertial weight evolving through the iterations, $\vec{p_n}^{k}$ and $\vec{g_n}^{k}$ are the locations of the personal best and global best fitnesses, c_1 and c_2 the weighting coefficients, and $r^k_{1,n}$ and $r^k_{2,n}$ are random variables within the range of $\{0,1\}$.

For BSO, the populations are grouped into clusters according to their position in the solution space in each iteration. Their new positions (also referred as ideas) are generated based on either one cluster or two clusters controlled by the difference between a random

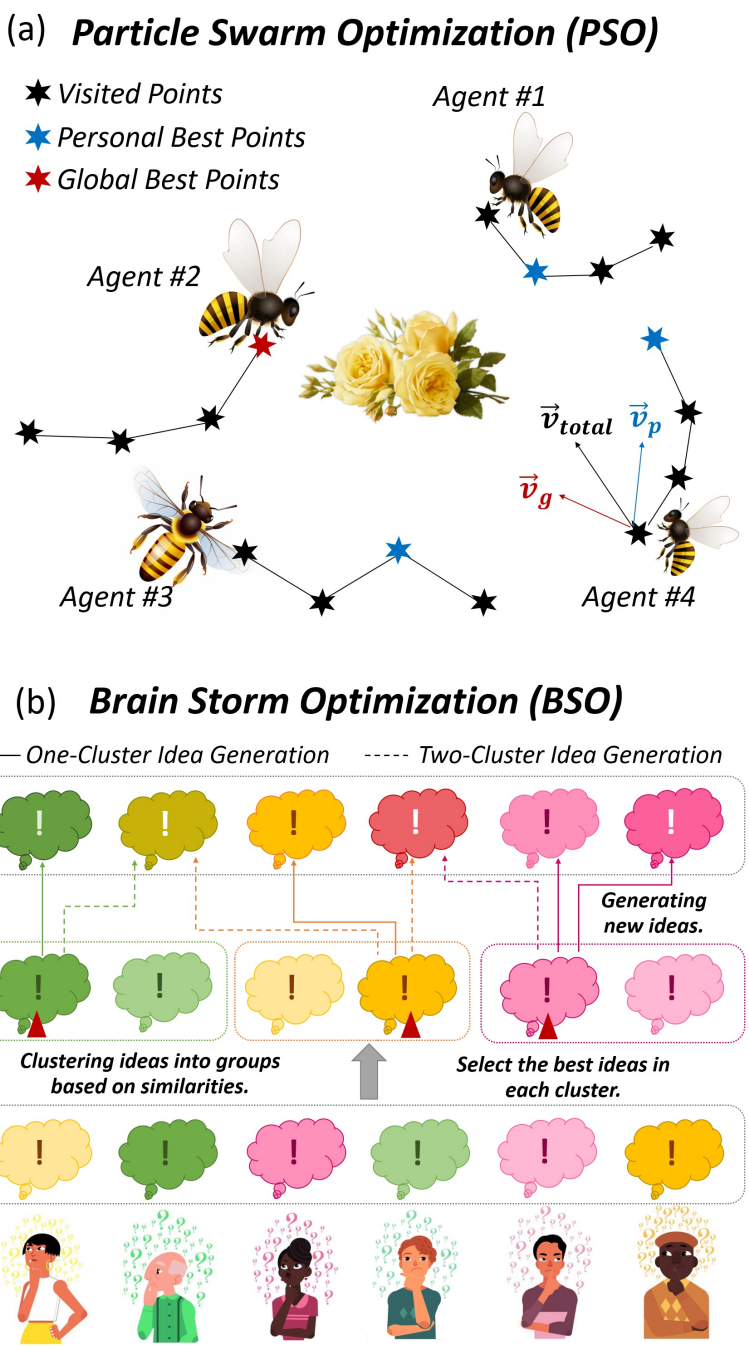

Figure 7.1: Principles of particle swarm optimization (PSO) brain storm optimization (BSO). (a) describes a swarm of bees searching for flowers with the previous visited points marked on the paths for each agent (bee). (b) illustrates the concept of idea generation in BSO by clustering the ideas. Both processes typically continue until reaching the maximum number of iterations.

parameter and a predefined generation parameter. Generating new idea from one cluster enables the algorithm to converge to a solution within a confined region, while generating new idea from two clusters improves the exploration ability and helps avoid deception. For one cluster generation, the ideas are updated as [127]:

$$\vec{x_{new}}^{k+1} = \vec{x_{select}}^{k} + \vec{\xi}^{k} \cdot \vec{N}^{k} \tag{7.3}$$

$$\vec{\xi}^{k} = \alpha r^{k} \exp\left(1 - \frac{K}{K-k+1}\right) \tag{7.4}$$

where $\vec{x_{select}}^{k}$ is the cluster center or a random idea in the selected cluster, $\vec{N}^{k}$ is a Gaussian random vector with mean of 0 and variance of 1, and $\vec{\xi}^{k}$ is a weighting coefficient of $\vec{N}^{k}$ that also contains a random variable r^{k} and evolves with iterations. K is the maximum number of iterations, and k is the number of current iteration. α is a parameter adapting to the size of the solution space to ensure the initial exploration is covering the entire solution space. Similarly, for two cluster idea generation, the $\vec{x_{select}}^{k}$ is generated based on existing ideas from two randomly selected clusters by [127]:

$$\vec{x_{select}}^{k} = R\vec{x_{select1}}^{k} + (1-R)\vec{x_{select2}}^{k} \tag{7.5}$$

where R is a random variables within the range of {0,1}. The new ideas are then generated with equation 7.3.

Inspection of the updating schemes of the two algorithms reveals BSO's inherent capability in diverse searching, because of the involvement of more random variables, which could be advantageous especially during the initial iterations.

7.2 PSO and BSO with Random and Predefined Initializations

In this section, the benchmarking Griewank function is used to compare the performance of PSO and BSO. Griewank function is expressed as:

$$F_{gr}(\vec{x}) = \frac{1}{4000}\sum_{i=1}^{D}[x_i^2] - \prod_{i=1}^{D}[\cos(x_i/\sqrt{i})] + 1 \tag{7.6}$$

which has a global minimum of 0 and is evaluated within the solution space of $x_i \in [-600, 600]$, $\forall\, i = 1, 2, ...D$. 15 dimensions and $4D + 1 = 61$ agents are assigned with a

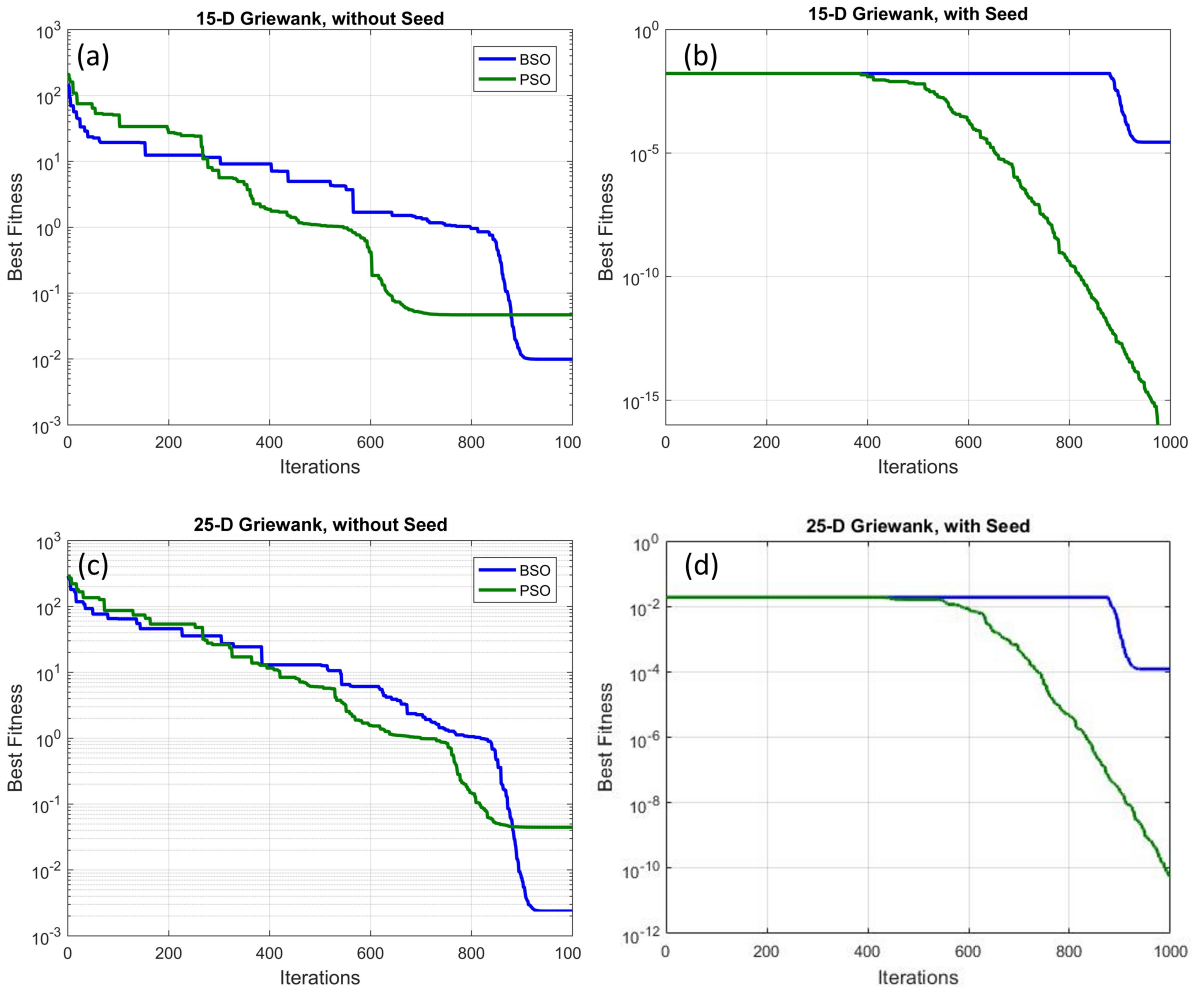

Figure 7.2: Best fitness in optimizing the 15-D and 25-D Griewank function using PSO and BSO, with (a) random initialization and (b) predefined seed assigned to one of the agents at $x_i = 1,\ \forall\, i = 1,\ 2,\ ...D$.

maximum of 1000 iterations, resulting in a total of 61000 function evaluations, while 25 dimensions and $4D+1 = 101$ agents are assigned with a maximum of 1000 iterations, resulting in a total of 101000 function evaluations, for both PSO and BSO. For PSO, social weights c_1 and c_2 are set to 2.0, inertial weight w^k is linearly decreasing from 0.9 to 0.4 through the iterations. For BSO, the number of clusters is set as 12 (about 1/5 of the number of agents), which has been proved to yield optimal performance [127]. Finally, invisible boundaries are used for both two algorithms, which erases the agents outside the boundaries from performing fitness evaluations.

The most commonly adopted swarm initialization in studying optimization techniques is the random initialization, in which the initial position of each agent is generated as:

$$\vec{x_n} = \vec{x_{min}} + \vec{r_n} \cdot (\vec{x_{max}} - \vec{x_{min}}) \tag{7.7}$$

where $\vec{x_{max}}$ and $\vec{x_{min}}$ are the specified maximum and minimum within the solution space, and $\vec{r_n}$ is random vector with value between 0 and 1 in each dimension. In many practical cases, however, the optimization could aim at fine tuning with a reasonable initial guess (referred as seed), which can be achieved by feeding the predefined seed to one of the agents while the rest of them remain random.

Fig. 7.2 plots the global best fitness obtained by PSO and BSO versus the number of iterations, with random initialization in (a), and predefined seed at the position of $x_i = 1.0$, $\forall\, i = 1, 2, ...15$ in (b). With randomly generated initial agents, BSO and PSO are demonstrating comparable performances within 1000 iterations. BSO is showing advantage over PSO in the initial searching speed within the first few hundreds (around 300) of iterations, and also finishes the optimization with a slightly lower fitness (1×10^{-2} for BSO versus 4×10^{-2} for PSO). However, with a initial seed assignment at $x_i = 1$, $\forall\, i = 1, 2, ...D$, which gives an initial best fitness on the order of 10^{-2}, PSO significantly outperforms BSO in the capability of local exploitation based on the knowledge of a "good" initial position. At the end of 1000 iterations, PSO returns a fitness on the order of 10^{-16}, while BSO finishes with a best fitness around 10^{-5}. The advantage of BSO in initial searching speed fails to demonstrate with the knowledge of a "good" seed.

7.3 Hybrid BSO-PSO in Patch Antenna Circuit Model Determination

Hybridizations of PSO with other optimization algorithms (e.g. genetic algorithm) have been studied in literature [128]. In this section, we investigate a hybrid of PSO and BSO, with the hope of benefiting from the advantages of both algorithms by switching from one to the other at certain number of iterations. The switching is done by taking the population of

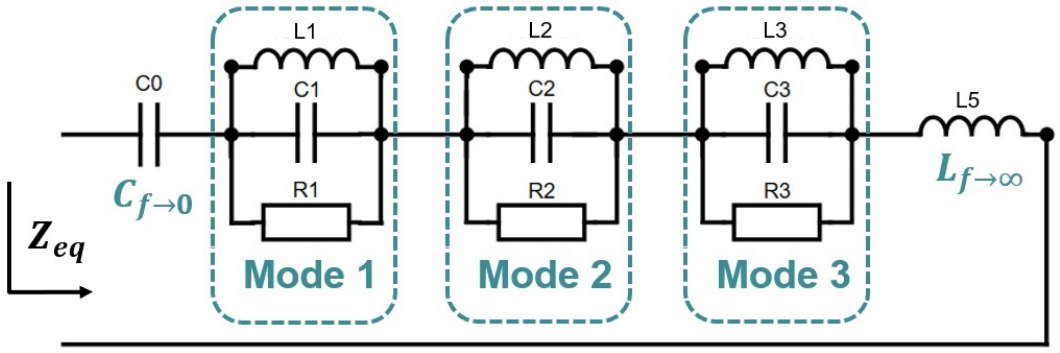

Figure 7.3: General topology of the equivalent lumped element circuit of rectangular patch antennas. The patch antenna input impedance is modeled by the series connection of parallel resonant RLC tanks, a low-frequency capacitor, and a high-frequency inductor.

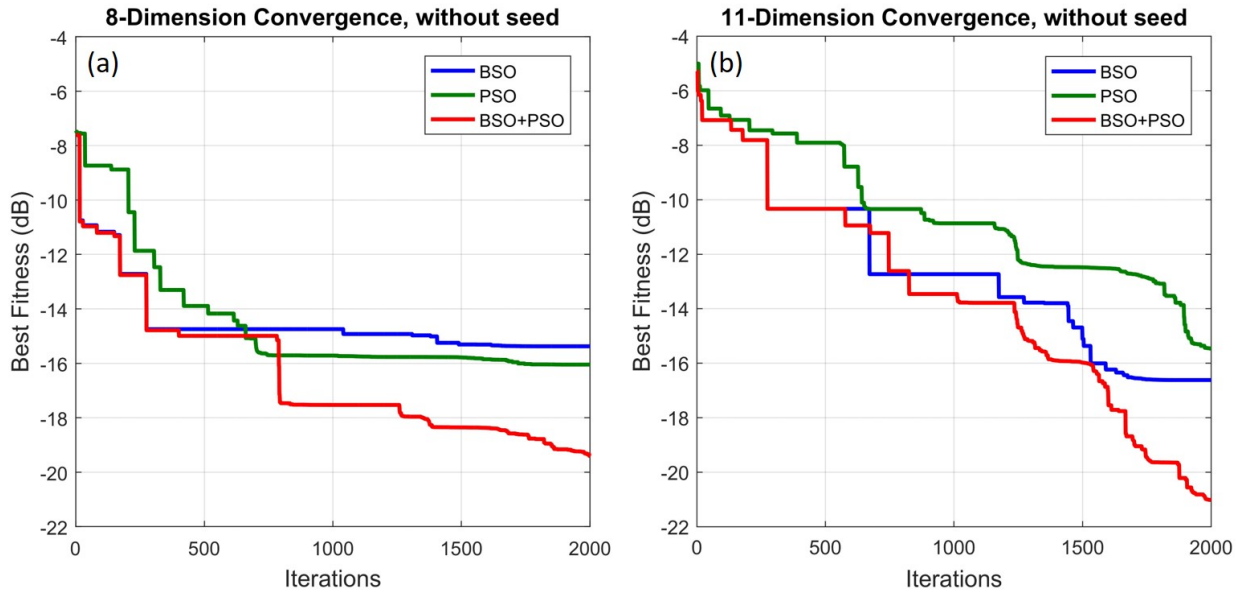

Figure 7.4: Best fitness in optimizing the circuit equivalence of patch antenna using BSO (blue), PSO (green), and the hybrid algorithm of PSO with BSO initialization (red). Two cases are studied, with (a) 8 dimensions and (b) 11 dimensions.

one algorithm and using it as the initial populations of the other algorithm. In this study, we perform PSO with BSO initialization, based on the observed advantages of initial exploration in BSO and local exploitation in PSO.

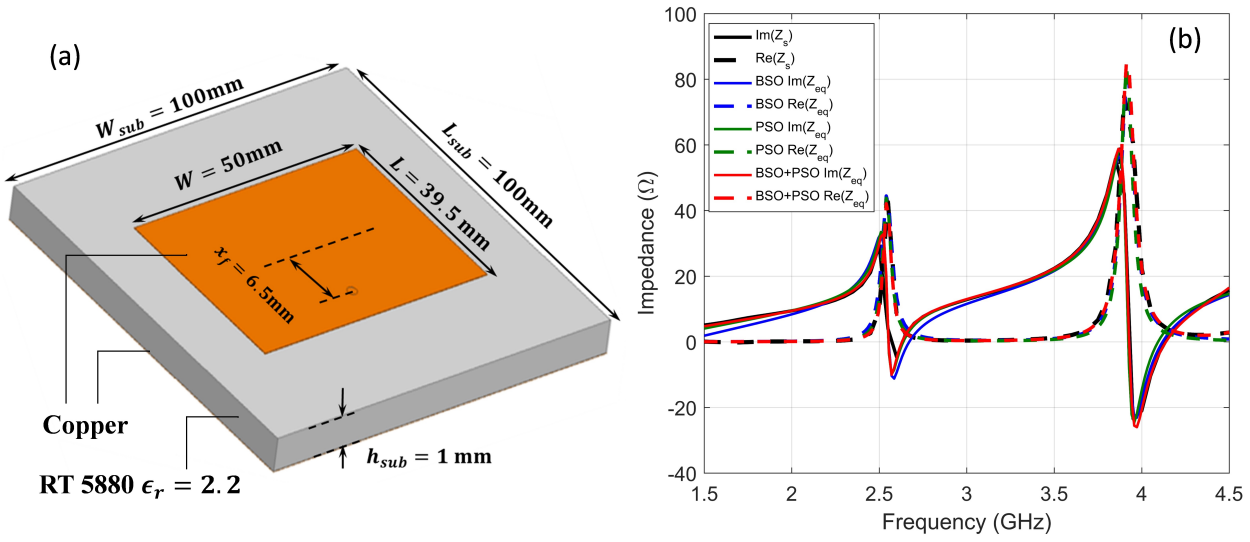

Figure 7.5: (a) Dimensions of the patch antenna used in the example of circuit model determination. (b) The simulated input impedance Z_s (black) and circuit equivalence impedance Z_{eq} of 11 dimensions obtained with BSO (blue), PSO (green), and hybrid of PSO with BSO initialization (red).

The example problem used in this section is the determination of circuit equivalence of a patch antenna, that has been utilized in Chapter 5 and 6. As shown in Fig. 7.3, a generalized circuit equivalence of patch antenna consists of the series connection of a low-frequency capacitor C_0, a high frequency inductor L_5, and parallel RLC tanks representing the orthogonal modes of resonance [123]. The input impedance of the equivalent circuit is written as:

$$Z_{eq} = j2\pi f L_5 + \frac{1}{j2\pi f C_0} + \sum_{i=1}^{M} (\frac{1}{R_i} + \frac{1}{j2\pi f L_i} + j2\pi f C_i)^{-1} \tag{7.8}$$

where M denotes the number of resonances in the frequency band of interest, R_i, C_i, L_i are the equivalent lumped resistance, capacitance and inductance for the ith number of resonant mode. The goal of this optimization is to find the circuit parameters C_0, L_5, R_i, C_i and L_i so that the difference between $Z_{eq}(f)$ computed from (7.8) and the $Z_s(f)$ generated from full-wave simulation is minimized. A normalized error function is therefore defined as the

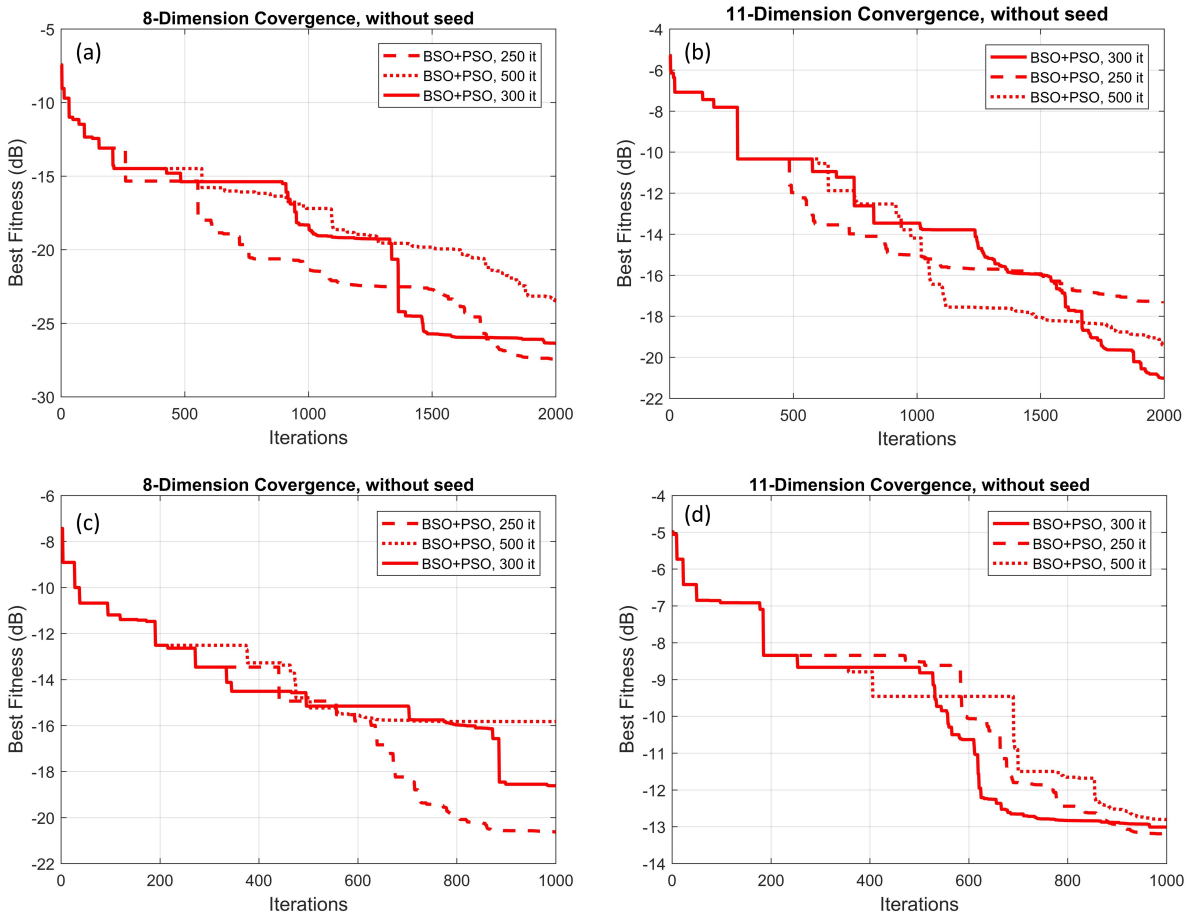

Figure 7.6: Best fitness in optimizing the circuit equivalence of patch antenna using the hybrid algorithm of PSO with BSO initialization. The number of iteration for switching from BSO to PSO is varied for the 8-dimensional and 11-dimensional cases, with the maximum of 1000 and 2000 iterations.

fitness:

$$\frac{1}{Z_0}\left(\frac{1}{N}\sum_{j=1}^{N}\{\mathrm{Re}[Z_s(f_j)-Z_{eq}(f_j)]^2+\mathrm{Im}[Z_s(f_j)-Z_{eq}(f_j)]^2\}\right)^{\frac{1}{2}} \tag{7.9}$$

where Z_0 is the characteristic impedance of 50 Ω, N is the total number of frequency sampling, f_j is the frequency for the jth sample.

In this study, we choose two cases with $M = 2$ and $M = 3$, resulting in 8-dimensional and 11-dimensional optimization problems. The solution space is defined as $C_0, C_i \in [0, 50]$ (pF), $L_5, L_i \in [0, 10]$ (nH), $R_i \in [10, 200]$ (Ω), $\forall i = 1, 2, 3$. The number of agents are

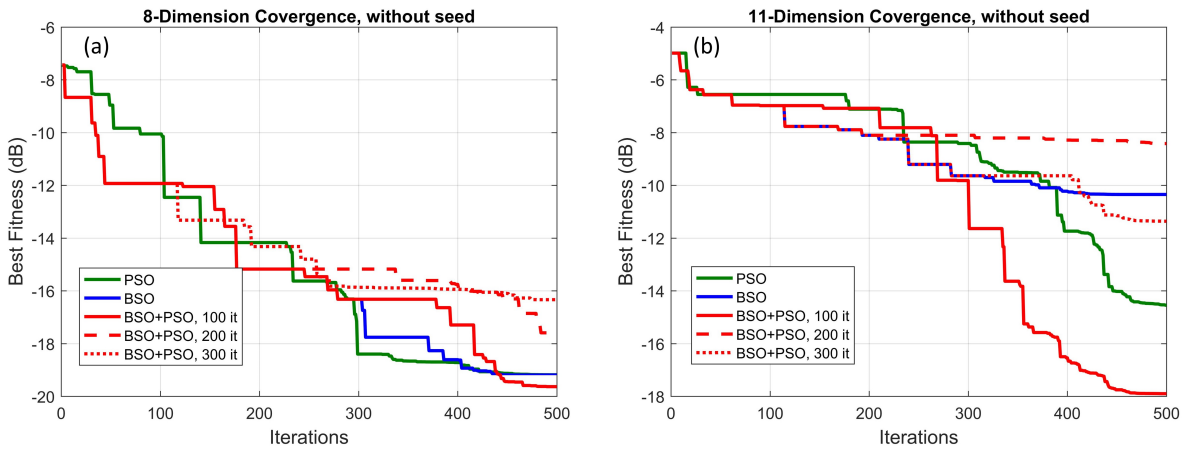

Figure 7.7: Best fitness in optimizing the circuit equivalence of patch antenna using BSO (blue), PSO (green), and the hybrid algorithm of PSO with BSO initialization (red). with the maximum of 500 iterations.

set as 33 and 45, with maximum iteration number of 2000, resulting in 66000 and 90000 fitness evaluations for the 8-dimensional and 11-dimensional cases. The intrinsic parameter setting for BSO and PSO are kept as stated in previous section, except number of clusters of BSO are chosen as 6 and 9 for the two cases (about 1/5 of agents number). BSO, PSO and BSO-PSO hybrid are compared by the two cases, all with random initialization. In the BSO-PSO hybrid, BSO is used in the initial 300 iterations, and then switched into PSO for the rest 1700 iterations with the initial populations taken from BSO in the 300th iteration. Fig. 7.4 plots the best fitness versus number of iterations using BSO (blue), PSO (green), and BSO-PSO hybrid (red). The BSO-PSO hybrid outperforms both BSO and PSO alone within 2000 iterations, for both 8-dimensional and 11-dimensional problems.

Dimensions of the rectangular patch antenna used in the example of circuit model determination are illustrated in Fig. 7.5 (a). The simulated input impedance Z_s and circuit equivalence impedance Z_{eq} of 11 dimensions obtained with BSO, PSO, and hybrid of PSO with BSO initialization are shown in Fig. 7.5 (b). All three methods generate reasonably good results, with the closest agreement to simulation obtained using the hybrid BSO-PSO.

A critical parameter in the BSO-PSO hybrid is the number of iteration that the optimiza-

tion algorithm switched from BSO to PSO. The number of iteration for switching from BSO to PSO is varied in Fig. 7.6. It is observed that fitness obtained by switching at 300th iteration is better than those at 250th and 500th iterations for the 11-dimensional problem, while the case switching at 250th iteration outperforms the other two cases for the 8-dimensional problem. This indicates that a larger solution space could result in a relatively large number of switching iteration in order to take fully advantage of BSO's exploration capability. Comparing Fig. 7.6 (a) and (c), or (b) and (d), it is observed that changing the maximum number of iterations from 2000 to 1000 does not significantly affect the observation for the optimal switching iteration, although the advantage of hybridization could be less significant with a reduced maximum iteration number. It is also interesting to notice that, comparing to the results in Fig. 7.4 (b) with PSO or BSO alone, the hybrid method outperforms in all three cases with different switching points, returning lower fitnesses at the end of 2000 iterations.

In many electromagnetic optimization problems the maximum number of iterations is limited within a few hundreds, due to the limitation in time and computational resources. The advantage of the hybrid algorithm over single algorithms with relatively small maximum iterations is therefore investigated. As shown in Fig. 7.7, the maximum number of iteration is set as 500 and the best fitness with single and hybrid algorithms with varying switching conditions is compared for 8-dimensional and 11-dimensional cases. For the hybrid BSO-PSO, the switching is implemented at 100th, 200th, and 300th iterations. Comparing Fig. 7.7 (a) and (b), hybrid BSO-PSO is demonstrating more improvement in the returned fitness for 11-D problem than its 8-D counterpart with a total of 500 iterations. The advantage of hybrid over single algorithms appears to be more significant for a relatively large dimension and solution space. Comparing the results with varying switching conditions, it is also observed that although hybrid BSO-PSO could potentially achieve better performance than single algorithms, the improvement becomes more sensitive to the switching condition with a reduced total iteration number. For both 8-D and 11-D cases, only switching at 100th iteration results in improvements over single algorithms. The selection of the switching iteration therefore becomes more important and difficult as the total number of is limited to

a few hundreds, especially for high-dimensional problems.

7.4 Summary

We perform comparison study regarding the performance of PSO and BSO. The advantages of the two algorithms are identified using a benchmarking function. Based on this observation, a hybrid of PSO and BSO is proposed and investigated with the example of patch antenna circuit model determination. We demonstrate that the BSO-PSO hybrid algorithm could benefit from the advantages of both PSO and BSO, and therefore outperforms single technique in some optimization problems. We use high-dimensional optimization problems to investigate the improvements of BSO-PSO hybrid over single algorithms under varying switching conditions. It is observed that BSO-PSO holds more benefits with relatively large total number of iterations (a few thousands) and a larger solution space. The advantage could be maintained for relatively small total iteration number, with the switching condition carefully chosen.

Part III

Conclusions and Future Works

CHAPTER 8

Conclusions

Next-generation antenna designs involve new materials and fabrication processes for emerging wireless applications. The exploitation of new material also relies on novel integration and synthesis processes to enhance the capabilities of electronic devices, circuits and systems. In this work, we have presented several novel antenna innovations and analysis that exploit the use of new materials and fabrication technologies, providing performance improvement to the current state-of-the-art.

The work presented in this dissertation is divided into two parts, seven Chapters. In the first part of this work, the use of liquid metal EGaIn in designing reconfigurable antennas is extensively explored. Liquid metal-based RF reconfiguration is proposed as an alternative solution to semiconductor-based reconfiguration, with the major advantage of more flexibility and better power handling. The major contributions in this part are summarized as follows:

- **Design:** Two novel patch antenna designs are proposed towards ultra-wide tuning range in frequency and polarization characteristics based on liquid metal reconfiguration. Chapter 2 has demonstrates a wide-band and continuous frequency reconfigurable patch antenna with switchable slots (PASS) that achieves a 70% tuning bandwidth with a 2% instantaneous bandwidth. Chapter 3 demonstrates a polarization reconfigurable patch antenna capable of multi-polarization reconfiguration among dual circular polarizations (RHCP and LHCP) and linear polarization with arbitrarily tunable orientation in the x-y plane, achieved with a single element and a single feed. The achieved flexibilities and integration simplicity of the two antenna designs are extraordinary comparing to the current state-of-the-art based on semiconductor devices, which typically requires multiple feeds, increased number of devices, and complex biasing design to achieve a

comparable tuning flexibility. The two designs are both based on slot-loaded patch antennas, which have been widely used in wireless communication, due to their low-profile, low-cost feature and capability of realizing various functionalities. The work presented in this dissertation utilizes the flexible nature of liquid conductor and the slot-loading technique in patch antenna design to achieve reconfiguration capabilities in various aspects of antenna characteristics, i.e. frequency and polarization agilities.

- **Analysis:** The related theoretical analysis are presented in each chapter to assist the understanding and design of the proposed antennas. In Chapter 2, the effects of slot-loading in PASS is introduced by explaining the dual-band operation characteristics two frequencies of resonance. Simple empirical formulas to predict the two resonant frequencies are established based on full-wave simulation parameterized using particle swarm optimization. In Chapter 3, the circuit model aspects of designing asymmetric E-shaped patch antenna is discussed based on the theory of orthogonal modes degeneration. We for the first time develop a circuit equivalence for the E-shaped patch antenna that is asymmetrically loaded. In Chapter 4, we first describe the analytical solutions for insulating monopole immersed in lossy dielectric media, and based on that, propose a coaxial antenna that can be adaptively tuned with liquid metal to maintain the optimal impedance matching in a varying lossy dielectric environment. These related analysis brought underlying physical insights to the proposed antenna designs and can be potentially implemented in accelerating the design procedures to achieve the targeted performances.

- **Implementation:** The fabrication processes for the liquid metal and microfluidic based reconfigurable patch antennas are practiced extensively and discussed in detail. Building reliable microfluidics on printed circuit boards (PCB) presents a great challenge of upscaling in the microfluidics society. One of the major difficulties is the incompatibility between PCB and the popular microfluidic material PDMS. In this work we for the first time explore the option of integrating 3D printed microfluidics onto PCB for the application of reconfigurable patch antennas. Section 2.3 provides

important hands-on details including material selection, surface treatment, liquid loading procedures etc. These discussions could be beneficial to researchers in the related fields of antennas, electronics or microfluidics. In Section 3.5, we carefully characterize the liquid metal tuning technique regarding the properties of switching speed, power handling, insertion and isolation, etc. These performances are compared to other popular options based on literatures and experiments, with the advantages and drawbacks clearly identified. These discussions are critical in the potential application of the liquid metal tuning technique.

- **Application:** Chapter 4 is dedicated to the exploration of liquid-metal tuning in a specific medical application for cancer treatment. We propose an interstitial coaxial antenna that can be adaptively tuned in real time with liquid metal. The purpose of tuning is to maintain the optimal impedance matching in a varying lossy dielectric environment, as the ablation antenna is applied to different organs or different states of tissue (dehydrated, desiccated, charred). The liquid metal reconfiguration is preferred over semiconductor-based tuning, mainly due to the intense power requirement. In order to effectively elevate the local area to cytotoxic temperature, the applied incident power level is typically in the range of 50 to 150 W, significantly higher than what is utilized in conventional electronic systems.

Another important aspect of the current antenna design highlights lies in the applications involving wireless body-area networks (WBANs), which enables the vision of ubiquitous healthcare. The recent advances in wireless communication and in electronics offer small and intelligent sensors able to be used on, around, or implanted in the human body. In the second part of this work, we focus on wearable antenna design based on electro-textile material, for the emerging applications in WBANs. The major contributions in this part are summarized as follows:

- **Design:** The embroidery-based electro-textile patch antennas are different to the ones fabricated with bulk conductive materials since the characterization of the detailed

embroidery structures need to be carefully incorporated into the antenna design procedures. In Chapter 5 we present the methodology of material characterization and modeling strategies for embroidered textile rectangular patch antennas. The methodologies of dielectric and conductive textile material characterizations are provided, and the full-wave modeling strategies to incorporate some unique aspects of embroidery are proposed for the first time. These design and modeling strategies are validated to be effective in predicting the resonance and radiation properties of the prototyped embroidery patch antenna.

- **Analysis:** The major work of analysis in second part of the dissertation is embodied in Chapter 6, in which a systematic and comprehensive investigation of the bending effects of wearable rectangular patch antennas is presented. We focus on the resonant frequency and radiation pattern variations due to bending in two principle planes by simulating patch antennas in a full-wave simulations. A frequency shift plot with respect to bending radius has been generated to target antennas for various wearable applications. An analytical approach using cylindrical-rectangular cavity model has been implemented to study the effect of resonant frequency shifting due to cylindrical bending in two principle planes. An equivalent lumped element circuit model is developed to study the bending effect, which provide more physical insights on the complex mechanism of antenna bending. Measurement results using 3D printed bending fixture is discussed and compared with simulations. The work presented in this section could assist antenna engineers to incorporate the effects of bending more efficiently for various wearable applications.

- **Optimization:** Utilization of optimization schemes has evolved as a popular strategy in solving complex electromagnetic problems. While the use of optimization has been extensively practiced in the previous chapters, Chapter 7 has been specifically dedicated to the discussion about a hybrid of particle swarm optimization (PSO) and brain-storm optimization (BSO), which aims at taking advantages of the two single algorithms. The hybrid algorithum is investigated with the example of patch antenna circuit model

determination. The advantages and limitations of the hybrid algorithm comparing with PSO and BSO are discussed in this chapter.

CHAPTER 9

Future Work

9.1 Fully-Integrated Liquid Metal Pneumatic Control System

Figure 9.1: A two-channel syringe pump [129](a) and a stainless steel piezoelectric micropump [130] (b).

The development of automatic and fully-integrated liquid metal control system is critical in the practical application of liquid metal reconfiguration technique. The most straightforward approach to accurately and automatically handle liquid metal in a fluidic system is to integrate pumps. There are many different types of pumps available in the market. Syringe pumps offers good tuning accuracy but are generally expensive and create bulky device. A more favorable option is to integrate miniature micropumps for liquid control [130]. Representative pictures of syringe pump and micropump are shown in Fig. 9.1. Besides the use of micropumps, liquid metal can also be actuated using electro-wetting. With the presence of electrolyte, the electrochemical reactions on the surface of the metal deposit or remove the surface oxide, which results in large changes in the interfacial tension of the metal. Applying a small DC voltage causes the metal to flow into or out of a capillary. The authors of [131]

has successfully demonstrated the use of electro-wetting in a reconfigurable liquid metal monopole antenna. However, the use of electrolyte as carrier liquid introduce additional loss to the reconfiguration element and could degrade the overall antenna efficiency.

To the end, the potential future effort aims at developing a cheap, robust and integrated liquid metal pneumatic control system. The use of different carrier liquid can be explored to improve system reliability and reusability (e.g. high viscosity oil Hydrocal 2400). Multi-layer microfluidic will be designed and implemented to move the liquid system to the back side of radiation element to avoid the influence to radiation. Micro-pumps will be incorporated to achieve automation with high accuracy. Finally, evaluation of the tuning resolution, power consumption, transition behaviors etc. will be carried out based on the new system setup.

9.2 Adaptively Tunable Ablation Antennas for Lung Cancer Treatments

Lung cancer has been reported as the most common cancer, with approximately 2.09 million new diagnoses each year, and is claiming more lives yearly than breast, colon, and prostate cancers combined. With the clinical practice of microwave ablation widely adopted for liver cancer, studies reporting lung cancer treatments with interstitial microwave ablation are relatively limited. As shown by the preliminary experiment results in Chapter 4, while the lung-tuned antenna led to significantly less reflected power compared to the liver-tuned antenna in the lung, the amount of reflected power remained high (22-32%) throughout the ablation period. In clinical practice the variation of tissue dielectric properties is expected to be more significant with ventilation. This suggests that the lung environment is much more heterogeneous and time-varying compared to the liver, which necessitates the integration of a more intense cooling system, with any fixed applicator antenna design. Successful adaptive tuning could potentially decrease the need for cooling mechanisms. The studies in antenna optimization, particular in the utility of using tunable antennas via dynamic tuning, will likely play a role in the development of next generation microwave ablation systems.

The study presented in Chapter 4 could be continued is several aspects towards a more

realistic in-vivo application of lung ablation antennas, through both multi-physics simulation and experimental validation. A more complete modeling incorporating both electromagnetic radiation and heat transfer could be developed for a time-varying estimation of ablation performance. Thermal equations and electromagnetic equations can be coupled through two major mechanisms. First, the microwave power density absorbed by the tissue is the thermal source during heat transfer. Second, the effects of heat absorption and heat transfer elevates local temperature, generating the time-varying dielectric properties of the lung tissue. Regarding experimental validation, the effects of blood flow in the in-vivo lung tissue could potentially reduce the ablation size comparing to what is obtained in ex-vivo experiments as we presented in Chapter 4. The cycling between inflating and deflating states should be implemented in future experiments to approximate the clinical scenario.

9.3 Electro-Textile Antennas in Potential Wearable Applications

Figure 9.2: Photograph of hospital environment [132].

Wireless body-area networks (WBANs) have attracted much attention in recent times due to the emerging wearables market, and medical WBANs have been highlighted as a solution to deliver better healthcare, synchronous automated data collection, and intelligent

diagnostics in busy clinical environment such as patient rooms in hospital. It is also important to consider how patient posture may effect on-body data links in a hospital environment, as illustrated in Fig. 9.2. The work in [133] reported how body geometry changes will change the channel impulse response. Investigations by the authors of [134–136] each presented path loss measurements in various environments between the master node (waist) and a range of distributed transceivers on several body areas (wrist, head, chest, ankle, thigh, hand etc.).

This portion of potential future work aims at demonstrating a practical wearable sensing system enabled by electro-textile antennas. This part of work involves integrating electro-textile antennas with RF modules, microcontroller and wearable sensors to build a wireless wearable platform, as well as performance testing of E-textile antennas in realized Bluetooth/WIFI communication link for on-body health monitoring application. The effects of posture on textile antenna performance could also be investigated to improve system reliability.

APPENDIX A

Solving the Eigenfrequencies for the Cylindrical-Rectangular Cavity

This appendix provides the detailed steps for (6.2) and (6.3) to calculate the eigenfrequencies for the cylindrical-rectangular cavity, with the geometry shown in Fig. 6.8. The cavity model is a common choice for analyzing microstrip patch antennas due to their narrow-band resonant characteristics. The rationale for using cylindrical-rectangular cavity model on analyzing patch antenna bending stems from the analogy with flat rectangular patch antenna, for which the boundary conditions are defined based on the following observations:

1. Referring to the top and bottom walls, the electric field has only normal components and the magnetic field has only transverse component in the rectangular cavity region bounded by the patch and ground plane. This observation provides for the electric wall at the top and bottom surfaces.

2. Referring to the side walls, the electric current has no normal components to the edge of the walls, which implies that the tangential components of the magnetic field along the edge is negligible. This observation provides for the magnetic wall at the side surfaces.

For the cylindrical-rectangular cavity model for patch antenna bent on cylindrical surface, although the characteristic modes are perturbed by the bending situation, the similar boundary conditions still hold for the cylindrical-rectangular cavity. Therefore, the electric wall on top and bottom and magnetic wall on side walls are applied in this analysis.

The electric vector potential $\vec{F}$ and magnetic vector potential $\vec{A}$ satisfy the Helmholtz equation:

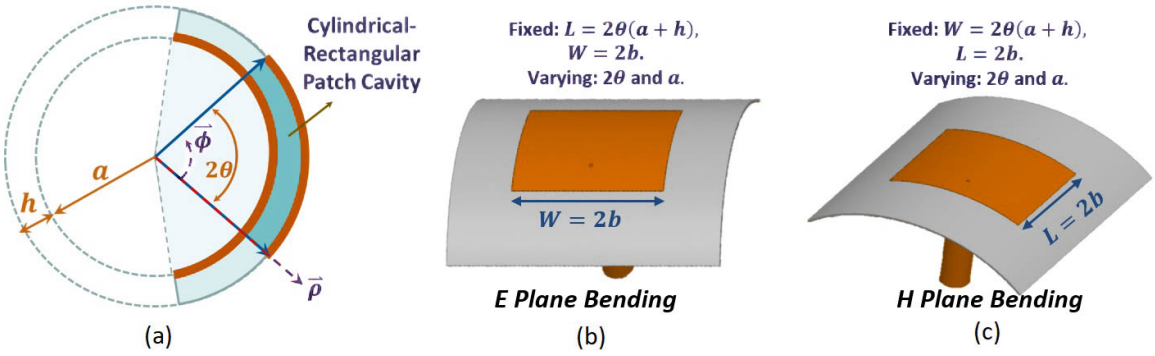

Figure A.1: The cylindrical-rectangular cavity model for patch antenna bent on cylindrical surface. (a) Side view of the cavity model, fixed and varying parameters for E plane bending (b) and H plane bending, respectively.

$$\nabla^2 \vec{F} + k^2 \vec{F} = 0 \tag{A.1}$$

$$\nabla^2 \vec{A} + k^2 \vec{A} = 0, \tag{A.2}$$

where $k^2 = (2\pi f)^2 \mu\epsilon$. Here the dielectric constant of cotton is used $\epsilon = 2.1$. In general the material loss could also be considered. However, for dry cotton the material loss at S band (2 to 4 GHz) is relatively small ($\tan\delta < 0.03$ [119]) and is thus neglected in this study. Consider the case of bending in E plane with bending angle 2θ, in which the boundary conditions are specified as:

$$\text{Electric Walls: } \rho = a, \rho = a + h, 2\theta(a + h) = L \tag{A.3}$$

$$\text{Magnetic Walls: } \phi = 0°, \phi = 2\theta, z = 0, z = 2b, 2b = W \tag{A.4}$$

The related dimensions are illustrated in Fig. A.1. For the transverse electric mode TEz, the solution is constructed by:

$$\vec{A} = 0, \vec{F} = \hat{z}\psi \tag{A.5}$$

$$\psi_{mli} = A_{mli} R_\nu(k_{mi}\rho) \sin(\frac{m\pi}{2\theta}\phi) \cos(\frac{l\pi}{2b}z) \tag{A.6}$$

where ψ_{mli} is the corresponding scalar function for the mode TE_{mli}, A_{mli} is a constant associated with the mode. The solution for ψ_{mli} above satisfies the magnetic wall boundary

conditions for ϕ and z. Function R_ν with $\nu = m\pi/2\theta$ satisfies the Bessel equation:

$$p\frac{d}{dp}[p\frac{dR_\nu(p)}{dp}] + [p^2 - \nu^2]R_\nu(p) = 0, p = k_{mi}\rho \tag{A.7}$$

$$R_\nu(p) = c_1 J_\nu(p) + c_2 Y_\nu(p) \tag{A.8}$$

where the solution of function R_ν is written as a summation of Bessel functions of the first kind J_ν and Bessel functions of the second kind Y_ν. The electric wall boundary condition for ρ requires the derivative of function R_ν to satisfy:

$$R'_\nu(p)|_{\rho=a,\rho=a+h} = 0 \tag{A.9}$$

$$c_1 J'_\nu(k_{mi}a) + c_2 Y'_\nu(k_{mi}a) = 0 \tag{A.10}$$

$$c_1 J'_\nu(k_{mi}(a+h)) + c_2 Y'_\nu(k_{mi}(a+h)) = 0 \tag{A.11}$$

Note that the prime here represents the derivative with respect to the whole argument of the Bessel function. Considering the matrix equation formed by the two linear equations with c_1 and c_2 as unknowns, the non-trivial solution exists only when the determinant goes to zero:

$$J'_\nu(k_{mi}a)Y'_\nu(k_{mi}(a+h)) - J'_\nu(k_{mi}(a+h))Y'_\nu(k_{mi}a) = 0 \tag{A.12}$$

Once the argument k_{mi} is solved from the equation, the resonant frequency can be found for each of the mode TE_{mli} as:

$$f_{r,mli} = \frac{1}{2\pi\sqrt{\epsilon\mu}}\sqrt{k_{mi}^2 + (\frac{l\pi}{2b})^2} \tag{A.13}$$

Likewise the E plane bending, for the case with bending in H plane, the boundary conditions are specified as:

$$\text{Electric Walls: } \rho = a, \rho = a+h, 2\theta(a+h) = W \tag{A.14}$$

$$\text{Magnetic Walls: } \phi = 0^\circ, \phi = 2\theta, z = 0, z = 2b, 2b = L \tag{A.15}$$

The transverse magnetic mode TMz satisfying the magnetic boundary conditions is constructed as:

$$\vec{F} = 0, \vec{A} = \hat{z}\psi \tag{A.16}$$

$$\psi_{mli} = A_{mli} R_\nu(k_{mi}\rho)\cos(\frac{m\pi}{2\theta}\phi)\sin(\frac{l\pi}{2b}z), \nu = m\pi/2\theta \tag{A.17}$$

$$R_\nu(p) = c_1 J_\nu(p) + c_2 Y_\nu(p), p = k_{mi}\rho \tag{A.18}$$

In the case of TMz, the electric wall boundary condition requires the function R_ν to satisfy:

$$R_\nu(p)|_{\rho=a,\rho=a+h} = 0 \tag{A.19}$$

$$c_1 J_\nu(k_{mi}a) + c_2 Y_\nu(k_{mi}a) = 0 \tag{A.20}$$

$$c_1 J_\nu(k_{mi}(a+h)) + c_2 Y_\nu(k_{mi}(a+h)) = 0 \tag{A.21}$$

The non-trivial solution of $c_1$and c_2 gives the equation of k_{mi}, through which the resonant frequency can be solved accordingly:

$$J_\nu(k_{mi}a)Y_\nu(k_{mi}(a+h)) - J_\nu(k_{mi}(a+h))Y_\nu(k_{mi}a) = 0 \tag{A.22}$$

$$f_{r,mli} = \frac{1}{2\pi\sqrt{\epsilon\mu}}\sqrt{k_{mi}^2 + (\frac{l\pi}{2b})^2} \tag{A.23}$$

APPENDIX B

Circuit Parameters in the Circuit Equivalence for E-Shaped Patch Antenna

In this section we elaborate the details of the formulas used to find the circuit parameters in the circuit equivalence developed in Section III, with some representative cases calculated for the vertical and horizontal modes.

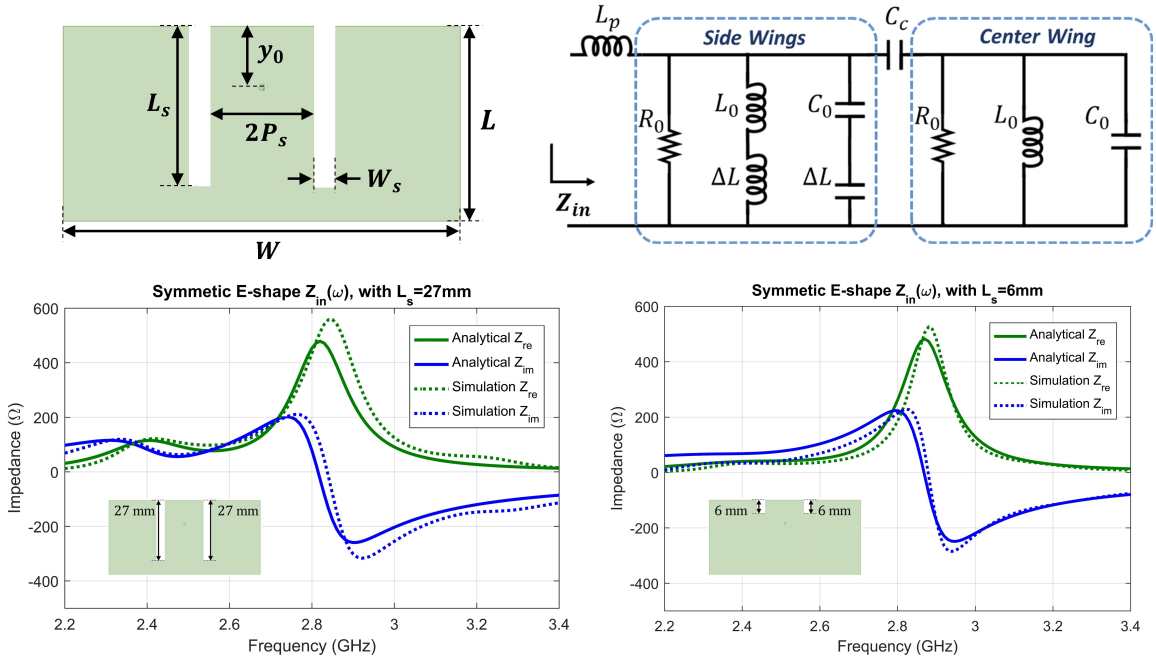

Figure B.1: Equivalent circuit for the vertical mode of resonance, with two representative cases of symmetric E-shaped patches calculated based on (3.2) and compared with full-wave simulation.

The vertical mode input impedance is formulated in (3.2) with the circuit equivalence illustrated in Fig. B.1, corresponding to a LP E-shaped patch with symmetric slot length.

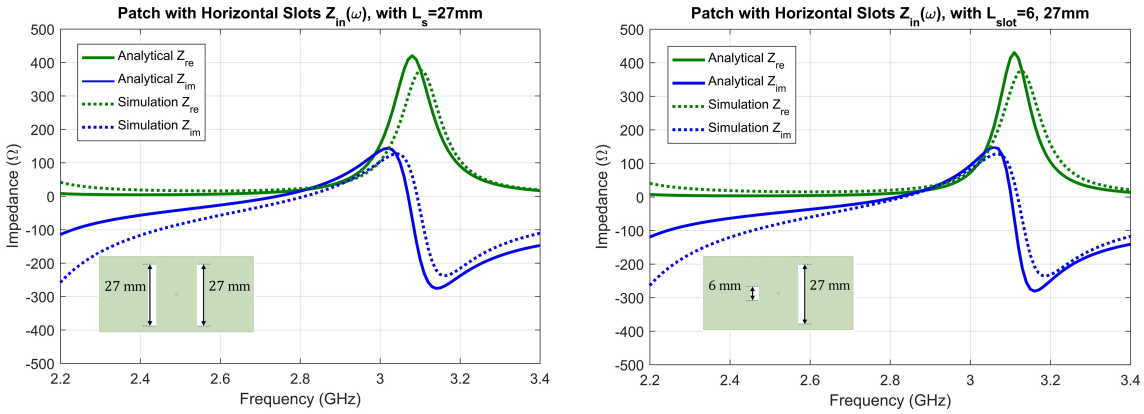

Figure B.2: Two representative cases of symmetric and asymmetric patch antenna with slots calculated based on (3.6) and compared with full-wave simulation.

The circuit parameters R_0, L_0, C_0 are found from the well-established formulas for rectangular microtrip antennas based on transmission-line model [137]. The effective dielectric constant ϵ_{eff}, fringing field length ΔL_f and resonant frequency f_r are given by:

$$\epsilon_{eff} = \frac{\epsilon_r + 1}{2} + \frac{\epsilon_r - 1}{2}[1 + \frac{10}{W/h}]^{-1/2} \tag{B.1}$$

$$\Delta L_f = 0.824h\frac{(\epsilon_r + 0.3)(W/h + 0.263)}{(\epsilon_r - 0.26)(W/h + 0.8)} \tag{B.2}$$

$$f_r = \frac{c}{2(L + \Delta L_f)\sqrt{\epsilon_{eff}}} \tag{B.3}$$

The input resistance at resonance R_0 and capacitance C_0 is obtained by transferring the self and mutual admittances for the two radiating edges to the input terminal:

$$R_0 = \frac{1}{2(G_0 + G_{m0})}(\cos\frac{\pi y_0}{L})^2 \tag{B.4}$$

$$G_0 = \frac{1}{120\pi^2}\int_0^\pi [\sin(\frac{k_r W\cos\theta}{2})]^2 \tan^2\theta \sin\theta d\theta \tag{B.5}$$

$$G_{m0} = \frac{1}{120\pi^2}\int_0^\pi [\sin(\frac{k_r W\cos\theta}{2})]^2 \tan^2\theta \sin\theta J_0(k_r L\sin\theta) d\theta \tag{B.6}$$

$$C_0 = \frac{\epsilon_{eff}\epsilon_0(L + \Delta_f)W}{2h}(\cos\frac{\pi y_0}{L})^{-2} \tag{B.7}$$

And the inductance L_0 is related to C_0 and f_r as:

$$L_0 = \frac{1}{(2\pi f_r)^2 C_0} \tag{B.8}$$

For the side wings, additional series inductance ΔL and ΔC incorporated to account for the effect of current flowing around the slots and the presence of notch capacitance. The notch inductance ΔL is accounted based on the transmission line theory and according to the current flows around the slot [138]:

$$\Delta L = \frac{Z_{01} + Z_{02}}{4\pi f_r}(\cos\frac{\pi y_0}{L})^2 \tan\frac{\pi f_r L_s}{c} \tag{B.9}$$

$$Z_{01,2} = 120\pi(\frac{W_{1,2}}{h} + 1.393 + 0.667\ln(\frac{W_{1,2}}{h} + 1.444))^{-1} \tag{B.10}$$

where $W_1 = 2P_s$ and $W_2 = (W - 2P_s - 2W_s)/2$ denotes the width of center and side wings, respectively. The notch capacitance ΔC is considered as the gap capacitance of coupled transmission lines between center and side wings [139]:

$$\begin{aligned}\Delta C &= 2L_s[\frac{\epsilon_0}{\pi}\ln(2\frac{1+\sqrt{k'}}{1-\sqrt{k'}}) + \frac{\epsilon_0\epsilon_r}{\pi}\ln\coth(\frac{\pi W_s}{4h}) \\ &+ 0.013\frac{C_f h}{W_s}](\cos\frac{\pi y_0}{L})^{-2}\end{aligned} \tag{B.11}$$

$$k' = \sqrt{1-k^2},\ \ k^2 = \frac{1 + (W_1 + W_2)/W_s}{(1 + W_1/W_s)(1 + W_2/W_s)} \tag{B.12}$$

$$C_f = \frac{\sqrt{\epsilon_{eff}}}{c(Z_{01} + Z_{02})} - \epsilon_0\epsilon_r\frac{W_1 W_2}{2h(W_1 + W_2)} \tag{B.13}$$

The mutual coupling capacitance between center and side wings C_c is found by considering the capacitive coupling of two parallel resonant circuits [50] with L_0, C_0 and $L' = L_0 + \Delta L$, $C' = C_0 + \Delta C$, resonant at $f_r = 1/(2\pi\sqrt{L_0 C_0})$ and $f_r' = 1/(2\pi\sqrt{L'C'})$, respectively:

$$C_c = \frac{1}{2}[-(C_0 + C') + \sqrt{(C_0 + C')^2 - 4C_0 C'(1 - 1/C_p^2)}] \tag{B.14}$$

$$C_p = \frac{1}{\sqrt{Q_0 Q'}},\ \ Q_0 = 2\pi f_r R_0 C_0,\ \ Q' = 2\pi f_r' R_0 C' \tag{B.15}$$

Notice that for the special case of $L_s = 0$, the notch induction ΔL, notch capacitance ΔC and coupling capacitance C_c all become 0, and the circuit equivalence of LP E-shaped patch reduces to that of a simple rectangular patch. Fig. B.1 gives two representative cases of symmetric E-shaped patches with L_s = 27mm and 6 mm, calculated based on (3.2) and compared with full-wave simulation with good agreement.

For the horizontal mode, the asymmetric E-shaped patch is modeled using transmission line theory and the input impedance Z_h is formulated in (3.6) to (3.8). The slot inductance due to the current going around the horizontal slot is given by [51]:

$$Z_{s1,2} = j\omega L_{s1,2} = j\omega \frac{h\pi\mu_0}{4}(1 - \frac{Z_{h0}}{Z_{h1,2}})^2 \tag{B.16}$$

$$Z_{h0} = 120\pi(\frac{L}{h} + 1.393 + 0.667\ln(\frac{L}{h} + 1.444))^{-1} \tag{B.17}$$

$$Z_{h1,2} = 120\pi(\frac{L - L_{s1,2}}{h} + 1.393 + 0.667\ln(\frac{L - L_{s1,2}}{h} + 1.444))^{-1} \tag{B.18}$$

To validate the transmission line model for horizontal mode, we simulated patch antenna with two slots cut and also horizontally excited from the center of x axis. Fig. B.2 plots the input impedance from circuit equivalence and full-wave simulation for two representative cases, with symmetric $L_s = 27$ mm, and asymmetric $L_s = 6, 27$ mm, proving the effectiveness of the circuit equivalence.

REFERENCES

[1] D. R. Smith, J. B. Pendry, and M. C. Wiltshire, "Metamaterials and negative refractive index," *Science*, vol. 305, no. 5685, pp. 788–792, 2004.

[2] S. M. Anlage, "The physics and applications of superconducting metamaterials," *Journal of Optics*, vol. 13, no. 2, p. 024001, 2010.

[3] R. F. Gibson, "A review of recent research on mechanics of multifunctional composite materials and structures," *Composite structures*, vol. 92, no. 12, pp. 2793–2810, 2010.

[4] P. Wright, B. Chambers, A. Barnes, K. Lees, and A. Despotakis, "Progress in smart microwave materials and structures," *Smart Materials and Structures*, vol. 9, no. 3, p. 273, 2000.

[5] M. Vaezi, H. Seitz, and S. Yang, "A review on 3d micro-additive manufacturing technologies," *The International Journal of Advanced Manufacturing Technology*, vol. 67, no. 5-8, pp. 1721–1754, 2013.

[6] T. Engineering and P. S. C. (EPSRC), "New materials for rf and microwave technologies," *IEEE Antennas and Wireless Propagation Letters*, 2014.

[7] L. Hinsz and B. D. Braaten, "A frequency reconfigurable transmitter antenna with autonomous switching capabilities," *IEEE Transactions on antennas and propagation*, vol. 62, no. 7, pp. 3809–3813, 2014.

[8] Y. Sung, T. Jang, and Y.-S. Kim, "A reconfigurable microstrip antenna for switchable polarization," *IEEE microwave and wireless components letters*, vol. 14, no. 11, pp. 534–536, 2004.

[9] N. Behdad and K. Sarabandi, "Dual-band reconfigurable antenna with a very wide tunability range," *IEEE Transactions on Antennas and Propagation*, vol. 54, no. 2, pp. 409–416, 2006.

[10] N. Behdad and K. Sarabandi, "A varactor-tuned dual-band slot antenna," *IEEE Transactions on Antennas and Propagation*, vol. 54, no. 2, pp. 401–408, 2006.

[11] C. Koo, B. E. LeBlanc, M. Kelley, H. E. Fitzgerald, G. H. Huff, and A. Han, "Manipulating liquid metal droplets in microfluidic channels with minimized skin residues toward tunable RF applications," *Journal of Microelectromechanical Systems*, vol. 24, no. 4, pp. 1069–1076, 2015.

[12] M. D. Dickey, R. C. Chiechi, R. J. Larsen, E. A. Weiss, D. A. Weitz, and G. M. Whitesides, "Eutectic gallium-indium (egain): a liquid metal alloy for the formation of stable structures in microchannels at room temperature," *Advanced Functional Materials*, vol. 18, no. 7, pp. 1097–1104, 2008.

[13] M. Wang, M. R. Khan, M. D. Dickey, and J. J. Adams, "A compound frequency-and polarization-reconfigurable crossed dipole using multidirectional spreading of liquid metal," *IEEE Antennas and Wireless Propagation Letters*, vol. 16, pp. 79–82, 2017.

[14] G. H. Huff, H. Pan, D. J. Hartl, G. J. Frank, R. L. Bradford, and J. W. Baur, "A physically reconfigurable structurally embedded vascular antenna," *IEEE Transactions on antennas and propagation*, vol. 65, no. 5, pp. 2282–2288, 2017.

[15] A. M. Morishita, C. K. Kitamura, A. T. Ohta, and W. A. Shiroma, "A liquid-metal monopole array with tunable frequency, gain, and beam steering," *IEEE antennas and wireless propagation letters*, vol. 12, pp. 1388–1391, 2013.

[16] A. P. Saghati, J. S. Batra, J. Kameoka, and K. Entesari, "Miniature and reconfigurable cpw folded slot antennas employing liquid-metal capacitive loading," *IEEE Transactions on antennas and propagation*, vol. 63, no. 9, pp. 3798–3807, 2015.

[17] W. Su, R. Bahr, S. A. Nauroze, and M. M. Tentzeris, "3d printed reconfigurable helical antenna based on microfluidics and liquid metal alloy," in *Antennas and Propagation (APSURSI), 2016 IEEE International Symposium on*, pp. 469–470, IEEE, 2016.

[18] M. R. Khan, C. Trlica, and M. D. Dickey, "Recapillarity: Electrochemically controlled capillary withdrawal of a liquid metal alloy from microchannels," *Advanced Functional Materials*, vol. 25, no. 5, pp. 671–678, 2015.

[19] D.-H. Kim, N. Lu, R. Ma, Y.-S. Kim, R.-H. Kim, S. Wang, J. Wu, S. M. Won, H. Tao, A. Islam, *et al.*, "Epidermal electronics," *science*, vol. 333, no. 6044, pp. 838–843, 2011.

[20] K. Chen, W. Gao, S. Emaminejad, D. Kiriya, H. Ota, H. Y. Y. Nyein, K. Takei, and A. Javey, "Printed carbon nanotube electronics and sensor systems," *Advanced Materials*, vol. 28, no. 22, pp. 4397–4414, 2016.

[21] S. Zhang, H. Ling, Y. Chen, Q. Cui, J. Ni, X. Wang, M. C. Hartel, X. Meng, K. Lee, J. Lee, *et al.*, "Hydrogel-enabled transfer printing: Hydrogel-enabled transfer-printing of conducting polymer films for soft organic bioelectronics (adv. funct. mater. 6/2020)," *Advanced Functional Materials*, vol. 30, no. 6, 2020.

[22] M. Stoppa and A. Chiolerio, "Wearable electronics and smart textiles: a critical review," *sensors*, vol. 14, no. 7, pp. 11957–11992, 2014.

[23] Z. Wang, *Electronic textile antennas and radio frequency circuits for body-worn applications*. The Ohio State University, 2014.

[24] D. Zhang, *Novel Electro-textile Antenna Designs Supporting Magnetic Resonance Imaging and Communication Systems*. University of California, Los Angeles, 2019.

[25] D. Moschou and A. Tserepi, "The lab-on-pcb approach: tackling the μtas commercial upscaling bottleneck," *Lab on a Chip*, vol. 17, no. 8, pp. 1388–1405, 2017.

[26] C. G. Christodoulou, Y. Tawk, S. A. Lane, and S. R. Erwin, "Reconfigurable antennas for wireless and space applications," *Proceedings of the IEEE*, vol. 100, no. 7, pp. 2250–2261, 2012.

[27] D. Zhang and Y. Rahmat-Samii, "Top-cross-loop improving the performance of the uwb planar monopole antennas," *Microwave and Optical Technology Letters*, vol. 59, no. 10, pp. 2432–2440, 2017.

[28] P. S. Hall, P. Gardner, and A. Faraone, "Antenna requirements for software defined and cognitive radios," *Proceedings of the IEEE*, vol. 100, no. 7, pp. 2262–2270, 2012.

[29] J. M. Kovitz, H. Rajagopalan, and Y. Rahmat-Samii, "Design and implementation of broadband MEMS RHCP/LHCP reconfigurable arrays using rotated E-shaped patch elements," *IEEE Transactions on Antennas and Propagation*, vol. 63, no. 6, pp. 2497–2507, 2015.

[30] A. Mansoul, F. Ghanem, M. R. Hamid, and M. Trabelsi, "A selective frequency-reconfigurable antenna for cognitive radio applications," *IEEE Antennas and Wireless Propagation Letters*, vol. 13, pp. 515–518, 2014.

[31] H. Li, J. Xiong, Y. Yu, and S. He, "A simple compact reconfigurable slot antenna with a very wide tuning range," *IEEE Transactions on Antennas and Propagation*, vol. 58, no. 11, pp. 3725–3728, 2010.

[32] F. Yang and Y. Rahmat-Samii, "Patch antennas with switchable slots (PASS) in wireless communications: Concepts, designs, and applications," *IEEE Antennas and Propagation Magazine*, vol. 47, no. 2, pp. 13–29, 2005.

[33] S. Waheed, J. M. Cabot, N. P. Macdonald, T. Lewis, R. M. Guijt, B. Paull, and M. C. Breadmore, "3d printed microfluidic devices: enablers and barriers," *Lab on a Chip*, vol. 16, no. 11, pp. 1993–2013, 2016.

[34] S. Maci, G. B. Gentili, P. Piazzesi, and C. Salvador, "Dual-band slot-loaded patch antenna," *IEE Proceedings-Microwaves, Antennas and Propagation*, vol. 142, no. 3, pp. 225–232, 1995.

[35] C. A. Ballanis, "Antenna theory analysis and design," *John Willey and Son's Inc., New York*, 1997.

[36] J. Robinson and Y. Rahmat-Samii, "Particle swarm optimization in electromagnetics," *IEEE transactions on antennas and propagation*, vol. 52, no. 2, pp. 397–407, 2004.

[37] Stratasys Inc, *Polyjet Material Datasheet*, 3 2016.

[38] L. Badicu, P. Notingher, L. Dumitran, G. Tanasescu, and D. Popa, "Measuring of the dielectric properties of mineral oil," in *Proceedings of the 5th International Conference Metrology & Measurement Systems*, pp. 284–289, 2009.

[39] H. Wong, W. Lin, L. Huitema, and E. Arnaud, "Multi-polarization reconfigurable antenna for wireless biomedical system," *IEEE Transactions on Biomedical Circuits and Systems*, vol. 11, no. 3, pp. 652–660, 2017.

[40] W. Lin and H. Wong, "Multipolarization-reconfigurable circular patch antenna with L-shaped probes," *IEEE Antennas and Wireless Propagation Letters*, vol. 16, pp. 1549–1552, 2017.

[41] H. H. Tran, N. Nguyen-Trong, T. T. Le, and H. C. Park, "Wideband and multipolarization reconfigurable crossed bowtie dipole antenna," *IEEE Transactions on Antennas and Propagation*, vol. 65, no. 12, pp. 6968–6975, 2017.

[42] C. Wang, J. C. Yeo, H. Chu, C. T. Lim, and Y.-X. Guo, "Design of a reconfigurable patch antenna using the movement of liquid metal," *IEEE Antennas and Wireless Propagation Letters*, vol. 17, no. 6, pp. 974–977, 2018.

[43] M. Wang, M. R. Khan, M. D. Dickey, and J. J. Adams, "A compound frequency-and polarization-reconfigurable crossed dipole using multidirectional spreading of liquid metal," *IEEE Antennas and Wireless Propagation Letters*, vol. 16, pp. 79–82, 2016.

[44] G. B. Zhang, R. C. Gough, M. R. Moorefield, K. J. Cho, A. T. Ohta, and W. A. Shiroma, "A liquid-metal polarization-pattern-reconfigurable dipole antenna," *IEEE Antennas and Wireless Propagation Letters*, vol. 17, no. 1, pp. 50–53, 2017.

[45] V. T. Bharambe, J. Ma, M. D. Dickey, and J. J. Adams, "Planar, multifunctional 3D printed antennas using liquid metal parasitics," *IEEE Access*, vol. 7, pp. 134245–134255, 2019.

[46] L. Song, W. Gao, C. O. Chui, and Y. Rahmat-Samii, "Liquid metal 3D printed microfluidic channel reconfigurable patch antenna with switchable slots," in *2018 United States National Committee of URSI National Radio Science Meeting (USNC-URSI NRSM)*, pp. 1–2, IEEE, 2018.

[47] L. Song, W. Gao, C. O. Chui, and Y. Rahmat-Samii, "Wideband frequency reconfigurable patch antenna with switchable slots based on liquid metal and 3-D printed microfluidics," *IEEE Transactions on Antennas and Propagation*, vol. 67, no. 5, pp. 2886–2895, 2019.

[48] A. Khidre, K. F. Lee, F. Yang, and A. Elsherbeni, "Wideband circularly polarized E-shaped patch antenna for wireless applications," *IEEE Antennas and Propagation Magazine*, vol. 52, no. 5, pp. 219–229, 2010.

[49] S. Maddio, A. Cidronali, and G. Manes, "A new design method for single-feed circular polarization microstrip antenna with an arbitrary impedance matching condition," *IEEE Transactions on Antennas and Propagation*, vol. 59, no. 2, pp. 379–389, 2010.

[50] V. K. Pandey and B. R. Vishvakarma, "Analysis of an E-shaped patch antenna," *Microwave and Optical Technology Letters*, vol. 49, no. 1, pp. 4–7, 2007.

[51] A. Khidre, F. Yang, and A. Z. Elsherbeni, "A patch antenna with a varactor-loaded slot for reconfigurable dual-band operation," *IEEE Transactions on Antennas and Propagation*, vol. 63, no. 2, pp. 755–760, 2014.

[52] Y. Rahmat-Samii and E. Michielssen, "Electromagnetic optimization by genetic algorithms," *Microwave Journal*, vol. 42, no. 11, pp. 232–232, 1999.

[53] E. Chang, S. Long, and W. Richards, "An experimental investigation of electrically thick rectangular microstrip antennas," *IEEE Transactions on Antennas and Propagation*, vol. 34, no. 6, pp. 767–772, 1986.

[54] 3M Scotch-Weld, *Epoxy Potting Compound/Adhesive*, 3 2015.

[55] A. Dey, R. Guldiken, and G. Mumcu, "Microfluidically reconfigured wideband frequency-tunable liquid-metal monopole antenna," *IEEE Transactions on Antennas and Propagation*, vol. 64, no. 6, pp. 2572–2576, 2016.

[56] V. Rathi, G. Kumar, and K. Ray, "Improved coupling for aperture coupled microstrip antennas," *IEEE Transactions on antennas and propagation*, vol. 44, no. 8, pp. 1196–1198, 1996.

[57] C. Wood, "Improved bandwidth of microstrip antennas using parasitic elements," in *IEE Proceedings H (Microwaves, Optics and Antennas)*, vol. 127, pp. 231–234, IET, 1980.

[58] F. Yang and Y. Rahmat-Samii, "Microstrip antennas integrated with electromagnetic band-gap (ebg) structures: A low mutual coupling design for array applications," *IEEE transactions on antennas and propagation*, vol. 51, no. 10, pp. 2936–2946, 2003.

[59] D. Nashaat, H. A. Elsadek, E. A. Abdallah, M. F. Iskander, and H. M. Elhenawy, "Ultrawide bandwidth microstrip patch array antenna using electromagnetic band-gap structure (ebg)," *IEEE transactions on antennas and propagation*, vol. 59, no. 5, pp. 1528–1534, 2011.

[60] S. Targonski, R. Waterhouse, and D. Pozar, "Design of wide-band aperture-stacked patch microstrip antennas," *IEEE Transactions on Antennas and Propagation*, vol. 46, no. 9, pp. 1245–1251, 1998.

[61] R. Waterhouse, *Microstrip patch antennas: a designer's guide*. Springer Science & Business Media, 2013.

[62] J. Costantine, Y. Tawk, S. E. Barbin, and C. G. Christodoulou, "Reconfigurable antennas: Design and applications," *Proceedings of the IEEE*, vol. 103, no. 3, pp. 424–437, 2015.

[63] M. Wang, I. M. Kilgore, M. B. Steer, and J. J. Adams, "Characterization of intermodulation distortion in reconfigurable liquid metal antennas," *IEEE Antennas and Wireless Propagation Letters*, vol. 17, no. 2, pp. 279–282, 2017.

[64] C. L. Brace, "Microwave tissue ablation: biophysics, technology, and applications," *Critical Reviews^{TM} in Biomedical Engineering*, vol. 38, no. 1, 2010.

[65] P. Laeseke, L. Sampson, T. Frey, D. van der Weide, F. Lee, and C. Brace, "Thermal ablation in kidneys: microwave ablation with a triaxial antenna results in larger zones of coagulation than rf," in *Radiological Society of North America Annual Meeting*, 2006.

[66] M. Ahmed, "Image-guided tumor ablation: standardization of terminology and reporting criteria—a 10-year update: supplement to the consensus document," *Journal of Vascular and Interventional Radiology*, vol. 11, no. 25, pp. 1706–1708, 2014.

[67] D. Galandi and G. Antes, "Radiofrequency thermal ablation versus other interventions for hepatocellular carcinoma," *Cochrane Database of Systematic Reviews*, no. 2, 2004.

[68] M. F. Meloni, J. Chiang, P. F. Laeseke, C. F. Dietrich, A. Sannino, M. Solbiati, E. Nocerino, C. L. Brace, and F. T. Lee Jr, "Microwave ablation in primary and secondary liver tumours: technical and clinical approaches," *International Journal of Hyperthermia*, vol. 33, no. 1, pp. 15–24, 2017.

[69] C. L. Brace, J. L. Hinshaw, P. F. Laeseke, L. A. Sampson, and F. T. Lee Jr, "Pulmonary thermal ablation: comparison of radiofrequency and microwave devices by using gross pathologic and ct findings in a swine model," *Radiology*, vol. 251, no. 3, pp. 705–711, 2009.

[70] M. Venturini, M. Cariati, P. Marra, S. Masala, P. L. Pereira, and G. Carrafiello, "Cirse standards of practice on thermal ablation of primary and secondary lung tumours," *CardioVascular and Interventional Radiology*, pp. 1–17, 2020.

[71] Y. Mohtashami, H. Luyen, J. F. Sawicki, J. D. Shea, N. Behdad, and S. C. Hagness, "Tools for attacking tumors: Performance comparison of triaxial, choke dipole, and balun-free base-fed monopole antennas for microwave ablation," *IEEE Antennas and Propagation Magazine*, vol. 60, no. 6, pp. 52–57, 2018.

[72] J. M. Bertram, D. Yang, M. C. Converse, J. G. Webster, and D. M. Mahvi, "A review of coaxial-based interstitial antennas for hepatic microwave ablation," *Critical Reviews^{TM} in Biomedical Engineering*, vol. 34, no. 3, 2006.

[73] J. Chiang, P. Wang, and C. L. Brace, "Computational modelling of microwave tumour ablations," *International Journal of Hyperthermia*, vol. 29, no. 4, pp. 308–317, 2013.

[74] S. Labonte, A. Blais, S. R. Legault, H. O. Ali, and L. Roy, "Monopole antennas for microwave catheter ablation," *IEEE transactions on microwave theory and techniques*, vol. 44, no. 10, pp. 1832–1840, 1996.

[75] R. D. Nevels, G. D. Arndt, G. W. Raffoul, J. R. Carl, and A. Pacifico, "Microwave catheter design," *IEEE Transactions on Biomedical Engineering*, vol. 45, no. 7, pp. 885–890, 1998.

[76] S. Etoz and C. L. Brace, "Analysis of microwave ablation antenna optimization techniques," *International Journal of RF and Microwave Computer-Aided Engineering*, vol. 28, no. 3, p. e21224, 2018.

[77] R. W. King, B. Trembly, and J. Strohbehn, "The electromagnetic field of an insulated antenna in a conducting or dielectric medium," *IEEE Transactions on Microwave Theory and Techniques*, vol. 31, no. 7, pp. 574–583, 1983.

[78] N. A. Durick, P. F. Laeseke, L. S. Broderick, F. T. Lee Jr, L. A. Sampson, T. M. Frey, T. F. Warner, J. P. Fine, D. W. Van der Weide, and C. L. Brace, "Microwave ablation with triaxial antennas tuned for lung: results in an in vivo porcine model," *Radiology*, vol. 247, no. 1, pp. 80–87, 2008.

[79] C. L. Brace, D. W. van der Weide, F. T. Lee, P. F. Laeseke, and L. Sampson, "Analysis and experimental validation of a triaxial antenna for microwave tumor ablation," in *2004 IEEE MTT-S International Microwave Symposium Digest (IEEE Cat. No. 04CH37535)*, vol. 3, pp. 1437–1440, IEEE, 2004.

[80] R. W. King, "Theory of the terminated insulated antenna in a conducting medium," *IEEE Transactions on Antennas and Propagation*, vol. 12, no. 3, pp. 305–318, 1964.

[81] S. Rao, N. Llombart, E. Moradi, K. Koski, T. Bjorninen, L. Sydanheimo, J. M. Rabaey, J. M. Carmena, Y. Rahmat-Samii, and L. Ukkonen, "Miniature implantable and wearable on-body antennas: towards the new era of wireless body-centric systems [antenna applications corner]," *IEEE Antennas and Propagation Magazine*, vol. 56, no. 1, pp. 271–291, 2014.

[82] G. Ginestet, N. Brechet, J. Torres, E. Moradi, L. Ukkonen, T. Björninen, and J. Virkki, "Embroidered antenna-microchip interconnections and contour antennas in passive uhf rfid textile tags," *IEEE Antennas and Wireless Propagation Letters*, vol. 16, pp. 1205–1208, 2017.

[83] A. Paraskevopoulos, D. de Sousa Fonseca, R. D. Seager, W. G. Whittow, J. C. Vardaxoglou, and A. A. Alexandridis, "Higher-mode textile patch antenna with embroidered vias for on-body communication," *IET Microwaves, Antennas & Propagation*, vol. 10, no. 7, pp. 802–807, 2016.

[84] A. Kiourti, C. Lee, and J. L. Volakis, "Fabrication of textile antennas and circuits with 0.1 mm precision," *IEEE Antennas and Wireless Propagation Letters*, vol. 15, pp. 151–153, 2016.

[85] Z. Wang, L. Zhang, Y. Bay Ram, J. L. Volakis, *et al.*, "Embroidered conductive fibers on polymer composite for conformal antennas," *IEEE Transactions on Antennas and Propagation*, vol. 60, no. 9, p. 4141, 2012.

[86] Y. Senbokuya and H. Tsunoda, "A study on the circular patch antennas using conductive non-woven fiber fabrics," in *Antennas and Propagation Society International Symposium, 2002. IEEE*, vol. 1, pp. 782–784, IEEE, 2002.

[87] X. Lin, B.-C. Seet, and F. Joseph, "Fabric antenna with body temperature sensing for ban applications over 5g wireless systems," in *Sensing Technology (ICST), 2015 9th International Conference on*, pp. 591–595, IEEE, 2015.

[88] R. Yahya, M. Kamarudin, N. Seman, and H. U. Iddi, "Eye shaped fabric antenna for uwb application," in *Antennas and Propagation Society International Symposium (APSURSI), 2013 IEEE*, pp. 228–229, IEEE, 2013.

[89] W. G. Whittow, A. Chauraya, J. Vardaxoglou, Y. Li, R. Torah, K. Yang, S. Beeby, and J. Tudor, "Inkjet-printed microstrip patch antennas realized on textile for wearable applications," *IEEE Antennas Wirel. Propag. Lett*, vol. 13, pp. 71–74, 2014.

[90] A. Chauraya, W. G. Whittow, J. Y. C. Vardaxoglou, Y. Li, R. Torah, K. Yang, S. Beeby, and J. Tudor, "Inkjet printed dipole antennas on textiles for wearable communications," *IET Microwaves, Antennas & Propagation*, vol. 7, no. 9, pp. 760–767, 2013.

[91] M. Akbari, L. Sydänheimo, Y. Rahmat-Sami, J. Virkki, and L. Ukkonen, "Implementation and performance evaluation of graphene-based passive uhf rfid textile tags," in *Electromagnetic Theory (EMTS), 2016 URSI International Symposium on*, pp. 447–449, IEEE, 2016.

[92] X-Static:, "http://www.noblebiomaterials.com/category2.asp?itemid=212,"

[93] Shieldex:, "http://www.statex.biz/?lang=en,"

[94] Amberstrand:, "http://www.metalcladfibers.com/amberstrand-fiber/,"

[95] R. K. Shawl, B. R. Longj, D. H. Werner, and A. Gavrin, "The characterization of conductive textile materials intended for radio frequency applications," *IEEE Antennas and Propagation Magazine*, vol. 49, no. 3, pp. 28–40, 2007.

[96] D. Zhang, *Novel Electro-textile Antenna Designs Supporting Magnetic Resonance Imaging and Communication Systems*. PhD thesis, UCLA, 2018.

[97] R. Seager, S. Zhang, A. Chauraya, W. Whittow, Y. Vardaxoglou, T. Acti, and T. Dias, "Effect of the fabrication parameters on the performance of embroidered antennas," *IET Microwaves, Antennas & Propagation*, vol. 7, no. 14, pp. 1174–1181, 2013.

[98] L. Song and Y. Rahmat-Samii, "A systematic investigation of rectangular patch antenna bending effects for wearable applications," *IEEE Transactions on Antennas and Propagation*, vol. 66, no. 5, pp. 2219–2228, 2018.

[99] R. Cavallari, F. Martelli, R. Rosini, C. Buratti, and R. Verdone, "A survey on wireless body area networks: Technologies and design challenges," *IEEE Communications Surveys & Tutorials*, vol. 16, no. 3, pp. 1635–1657, 2014.

[100] N. Rais, P. J. Soh, F. Malek, S. Ahmad, N. Hashim, and P. Hall, "A review of wearable antenna," in *Antennas & Propagation Conference, 2009. LAPC 2009. Loughborough*, pp. 225–228, IEEE, 2009.

[101] M. I. Jais, M. F. B. Jamlos, M. Jusoh, T. Sabapathy, M. R. Kamarudin, R. B. Ahmad, A. A. A.-H. Azremi, E. I. Bin Azmi, P. J. Soh, G. A. Vandenbosch, *et al.*, "A novel 2.45 GHz switchable beam textile antenna (sbta) for outdoor wireless body area network (wban) applications," *Progress In Electromagnetics Research*, vol. 138, pp. 613–627, 2013.

[102] T. Haagenson, S. Noghanian, P. de Leon, and Y.-h. Chang, "Textile antennas for spacesuit applications: Design, simulation, manufacturing, and testing of textile patch antennas for spacesuit applications.," *IEEE Antennas and Propagation Magazine*, vol. 57, no. 4, pp. 64–73, 2015.

[103] J. DicCbshfsE, M. K. Abd Rahim, N. A. Samsuri, H. A. M. Salim, and M. F. Ali, "Embroidered fully textile wearable antenna for medical monitoring applications," *Progress In Electromagnetics Research*, vol. 117, pp. 321–337, 2011.

[104] P. Salonen and Y. Rahmat-Samii, "Wearable antennas: Advances in design, characterization, and application," in *Antennas and Propagation for Body-Centric Wireless Communications* (P. S. Hall and Y. Hao, eds.), ch. 6, pp. 151–186, Norwood, MA, USA: Artech House, Inc., 2006.

[105] P. Salonen and Y. Rahmat-Samii, "Textile antennas: Effects of antenna bending on input matching and impedance bandwidth," *IEEE Aerospace and Electronic Systems Magazine*, vol. 22, no. 12, pp. 18–22, 2007.

[106] Q. Bai and R. Langley, "Textile PIFA antenna bending," in *Antennas and Propagation Conference (LAPC), 2011 Loughborough*, pp. 1–4, IEEE, 2011.

[107] Q. Bai and R. Langley, "Crumpling of PIFA textile antenna," *IEEE Transactions on Antennas and Propagation*, vol. 60, no. 1, pp. 63–70, 2012.

[108] A. Kiourti and J. L. Volakis, "Stretchable and flexible E-fiber wire antennas embedded in polymer," *IEEE Antennas and Wireless Propagation Letters*, vol. 13, pp. 1381–1384, 2014.

[109] H.-L. Kao, C.-L. Cho, X. Y. Zhang, L.-C. Chang, B.-H. Wei, X. Dai, and H.-C. Chiu, "Bending effect of an inkjet-printed series-fed two-dipole antenna on a liquid crystal polymer substrate," *IEEE Antennas and Wireless Propagation Letters*, vol. 13, pp. 1172–1175, 2014.

[110] B. Mandal, B. Mukherjee, A. Chatterjee, and S. K. Parui, "Design of printed body wearable textile antenna for broadband application," in *Applied Electromagnetics Conference (AEMC), 2013 IEEE*, pp. 1–2, IEEE, 2013.

[111] E. Rajo-Iglesias, I. Gallego-Gallego, L. Inclan-Sanchez, and O. Quevedo-Teruel, "Textile soft surface for back radiation reduction in bent wearable antennas," *IEEE Transactions on Antennas and Propagation*, vol. 62, no. 7, pp. 3873–3878, 2014.

[112] F. Boeykens, H. Rogier, and L. Vallozzi, "An efficient technique based on polynomial chaos to model the uncertainty in the resonance frequency of textile antennas due to bending," *IEEE Transactions on Antennas and Propagation*, vol. 62, no. 3, pp. 1253–1260, 2014.

[113] L. Vallozzi, F. Boeykens, and H. Rogier, "Cylindrically-bent rectangular patch antennas: novel modeling techniques for resonance frequency variation and uncertainty," in *Antennas and Propagation (EuCAP), 2015 9th European Conference on*, pp. 1–5, IEEE, 2015.

[114] C. Krowne, "Cylindrical-rectangular microstrip antenna," *IEEE Transactions on Antennas and Propagation*, vol. 31, no. 1, pp. 194–199, 1983.

[115] K.-M. Luk, K.-F. Lee, and J. S. Dahele, "Analysis of the cylindrical-rectangular patch antenna," *IEEE Transactions on antennas and propagation*, vol. 37, no. 2, pp. 143–147, 1989.

[116] V. Šafářová and J. Militkỳ, "Electromagnetic shielding properties of woven fabrics made from high-performance fibers," *Textile Research Journal*, vol. 84, no. 12, pp. 1255–1267, 2014.

[117] I. Locher, M. Klemm, T. Kirstein, and G. Trster, "Design and characterization of purely textile patch antennas," *IEEE Transactions on advanced packaging*, vol. 29, no. 4, pp. 777–788, 2006.

[118] W. L. Stutzman and G. A. Thiele, *Antenna Theory and Design*. John Wiley & Sons, 2012.

[119] S. Sankaralingam and B. Gupta, "Determination of dielectric constant of fabric materials and their use as substrates for design and development of antennas for wearable applications," *IEEE Transactions on Instrumentation and Measurement*, vol. 59, no. 12, pp. 3122–3130, 2010.

[120] Y. Rahmat-Samii, K. Kim, M. Jensen, K. Fujimoto, and O. Edvardsson, "Antennas and humans in personal communications," *Mobile Antenna Systems Handbook*, pp. 361–460, 2001.

[121] F. Boeykens, L. Vallozzi, and H. Rogier, "Cylindrical bending of deformable textile rectangular patch antennas," *International Journal of Antennas and Propagation*, vol. 2012, 2012.

[122] H. R. Sanjari, A. A. Merati, S. M. Hosseini Varkiyani, and A. Tavakoli, "Evaluation of the effect of bending on the resonance frequency of inset-fed rectangular textile patch antenna," *Journal of Industrial Textiles*, vol. 46, no. 1, pp. 19–44, 2016.

[123] M. Ansarizadeh, A. Ghorbani, and R. A. Abd-Alhameed, "An approach to equivalent circuit modeling of rectangular microstrip antennas," *Progress In Electromagnetics Research B*, vol. 8, pp. 77–86, 2008.

[124] C. Hertleer, A. Tronquo, H. Rogier, L. Vallozzi, and L. Van Langenhove, "Aperture-coupled patch antenna for integration into wearable textile systems," *IEEE antennas and wireless propagation letters*, vol. 6, pp. 392–395, 2007.

[125] A. Hoorfar, "Evolutionary programming in electromagnetic optimization: a review," *IEEE Transactions on Antennas and Propagation*, vol. 55, no. 3, pp. 523–537, 2007.

[126] P. Rocca, G. Oliveri, and A. Massa, "Differential evolution as applied to electromagnetics," *IEEE Antennas and Propagation Magazine*, vol. 53, no. 1, pp. 38–49, 2011.

[127] A. Aldhafeeri and Y. Rahmat-Samii, "Brain storm optimization for electromagnetic applications: continuous and discrete," *IEEE Transactions on Antennas and Propagation*, vol. 67, no. 4, pp. 2710–2722, 2019.

[128] J. Robinson, S. Sinton, and Y. Rahmat-Samii, "Particle swarm, genetic algorithm, and their hybrids: optimization of a profiled corrugated horn antenna," in *IEEE Antennas and Propagation Society International Symposium (IEEE Cat. No. 02CH37313)*, vol. 1, pp. 314–317, IEEE, 2002.

[129] K. S. Inc, "Kds200 series legacy syringe pump," *5600-002-REV-H*.

[130] D. Microfluidics, "Stainless steel piezoelectric pumps," *PN3200311, MAR-000085 V.A.5*.

[131] M. Wang, C. Trlica, M. Khan, M. Dickey, and J. Adams, "A reconfigurable liquid metal antenna driven by electrochemically controlled capillarity," *Journal of Applied Physics*, vol. 117, no. 19, p. 194901, 2015.

[132] K. D. A. Hospital, "https://www.kokilabenhospital.com," *PN3200311, MAR-000085 V.A.5*.

[133] M. Hämäläinen, T. Kumpuniemi, and J. Iinatti, "Observations from ultra wideband on-body radio channel measurements," in *General Assembly and Scientific Symposium (URSI GASS), 2014 XXXIth URSI*, pp. 1–4, IEEE, 2014.

[134] J.-W. Kim, Y. Kim, and S.-C. Kim, "Ultra wideband channel characteristics for body area network," in *Vehicular Technology Conference (VTC Spring), 2014 IEEE 79th*, pp. 1–5, IEEE, 2014.

[135] M. M. Khan, "Comparison of narrowband and ultra wideband subject-specific on-body radio channel studies for healthcare applications," in *Green Energy and Technology (ICGET), 2014 2nd International Conference on*, pp. 139–144, IEEE, 2014.

[136] Z. H. Hu, Y. I. Nechayev, P. S. Hall, C. C. Constantinou, and Y. Hao, "Measurements and statistical analysis of on-body channel fading at 2.45 ghz," *IEEE Antennas and Wireless Propagation Letters*, vol. 6, pp. 612–615, 2007.

[137] R. Garg, P. Bhartia, I. J. Bahl, and A. Ittipiboon, *Microstrip Antenna Design Handbook*. Artech house, 2001.

[138] X.-X. Zhang and F. Yang, "Study of a slit cut on a microstrip antenna and its applications," *Microwave and Optical Technology Letters*, vol. 18, no. 4, pp. 297–300, 1998.

[139] I. J. Bahl, *Lumped Elements for RF and Microwave Circuits*. Artech house, 2003.